Classical and quantum dynamics of twisted light

by

Frédéric Bouchard

Thesis submitted to the
Faculty of Graduate and Postdoctoral Studies
In partial fulfillment of the requirements
For the degree of
Master of Science in Physics

Ottawa-Carleton Institute of Physics
Department of Physics
University of Ottawa

© Frédéric Bouchard, Ottawa, Canada, 2016

Abstract

This thesis encompasses a body of experimental work on the dynamics of twisted light. We first deal with the generation and reconstruction of twisted light for applications in classical and quantum physics, respectively. In the first case, we present a novel device that has the ability to generate twisted light in a manner that is completely wavelength-independent. Such a device may find applications in various fields of classical physics, ranging from nano to astronomical imaging. In the second work, we study the dynamics of twisted light in the case of laser-induced radial birefringence. This is done by studying the optical features resulting from elastic properties of silver-doped glass. In the last work on generation of twisted light, we present a nano-scale twisted light generator having the capacity to generate an optical mode with a controllable number of twists. In the context of quantum communication and quantum computations, this device has a great potential due to its small size and integrability. In the second part of the thesis, we study the propagation of twisted light both at the classical and quantum regime. In the first case, we observe exotic group velocities of light pulses in vacuum due to the twisting of its wavefront. In the second case, we study the effect of quantum decoherence of twisted light due to the coupling of photonic internal degrees of freedom. We present a technique to recover the lost coherence, which we name *recoherence*, by a practical unitary transformation.

Résumé

Cette thèse comprend un ensemble de travaux expérimentaux portant sur la dynamique de la lumière tordue. Dans un premier temps, nous traitons de la génération et de la reconstruction de la lumière tordue pour des applications en physique classique et quantique. Dans le premier cas, nous présentons un appareil original pouvant générer de la lumière tordue indépendamment de la longueur d'onde de la lumière. Un tel appareil aurait plusieurs applications dans une variété de domaines en physique classique, allant de l'imagerie nanoscopique à l'imagerie astronomique. Dans le deuxième projet, nous étudions la dynamique de telles lumières dans le cas de biréfringence radiale induit par l'illumination d'un laser. Cela se fait en étudiant les propriétés optiques résultant des propriétés élastiques d'un échantillon de verre dopé d'argent. Dans le dernier projet portant sur la génération de lumière tordue, nous présentons un générateur de lumière tordue à une échelle nanoscopique ayant la capacité de générer un mode optique contenant un nombre désiré d'entortillements. Dans le contexte de communication et de calcul quantique, cet appareil possède un grand potentiel grâce à sa taille et son intégrabilité. Dans la deuxième partie de cette thèse, nous étudions la propagation de la lumière tordue sur le plan classique et quantique. Dans le premier cas, nous observons les vitesses de groupes exotiques d'impulsions optiques dans le vide dû à l'entortillement de son front d'onde. Dans le deuxième cas, nous étudions l'effet de décohérence quantique de la lumière tordue dû au couplage de différents degrés de liberté des photons. De plus, nous présentons une technique, que nous nommons *recohérence*, qui a pour but de récupérer la cohérence perdue en utilisant une transformation unitaire pratique.

Acknowledgements

I wish to thank my supervisors Prof. Ebrahim Karimi and Prof. Robert Boyd for their support, valuable advices and for giving me numerous opportunities throughout the course of my Master's degree. It is a privilege for me to work in such a unique scientific environment. I am particularly grateful to Prof. Karimi for countless hours of scientific discussions and for making himself available to us night and day, literally.

I acknowledge the financial support of the Canada Excellence Research Chairs (CERC) program, of the Natural Sciences and Engineering Research Council of Canada (NSERC) and of the Fonds de recherche du Québec en Nature et technologies (FRQNT).

I would like to thank Jérémie Harris for many interesting discussions and Harjaspreet Mand, my partner in crime, for making the lab such a fun place to work. Both were indispensable in the experiments presented in this thesis. I am also thankful to one great post-doc, Robert Fickler, and two great students, Alicia Sit and Hugo Larocque, for reading my thesis. Moreover, I would like to acknowledge all of my other co-authors Israel De Leon, Sebastian A Schulz, Jeremy Upham, Nicolas Bent, Mohammad Mirhosseini, Ali Akbar Ahangary, Enrico Santamato and Hamid Reza Khalesifard for making all of this possible. Finally, I would like to thank Alicia Sit, Hugo Larocque, Peter Morris and Jérémie Gagnon-Bischoff for making the lab such a lively place to work.

Certainly, none of this would have been possible without the support and patience of my family. I warmly appreciate their generosity and understanding.

Most importantly, I would like to thank my wonderful life partner, Véronique Bélanger, for always supporting me in my studies since the beginning.

Table of Contents

CV

Publications

1. **F. Bouchard**, I. De Leon, S. A. Schulz, J. Upham, E. Karimi, and R. W. Boyd, "Optical spin-to-orbital angular momentum conversion in ultra-thin metasurfaces with arbitrary topological charges," *Applied Physics Letters* **105**, 101905 (2014).

2. **F. Bouchard**, H. Mand, M. Mirhosseini, E. Karimi, and R. W. Boyd, "Achromatic orbital angular momentum generator," *New Journal of Physics* **16**, 123006 (2014).

3. A. Ahangary, **F. Bouchard**, E. Santamato, E. Karimi, and H. R. Khalesifard, "Dynamics of laser-induced radial birefringence in silver-doped glasses," *Optics Letters* **40**, 4062 (2015).

4. **F. Bouchard**, J. Harris, H. Mand, N. Bent, E. Santamato, R. W. Boyd, and E. Karimi, "Observation of quantum recoherence of photons by spatial propagation," *Scientific Reports* **5**, 15330 (2015).

5. S. A. Schulz, J. Upham, **F. Bouchard**, I. De Leon, E. Karimi, and R. W. Boyd, "Quantifying the impact of proximity error correction on plasmonic metasurfaces," *Optical Materials Express* **5**, 2798 (2015).

6. **F. Bouchard**, J. Harris, H. Mand, R. W. Boyd, and E. Karimi, "Observation of sub-luminal twisted light in vacuum," *Optica* **3**, 351 (2016).

7. J. Harris, **F. Bouchard**, E. Santamato, W. H. Zurek, R. W. Boyd and E. Karimi, "Quantum probabilities from quantum entanglement: experimentally unpacking the Born rule," *New Journal of Physics* **18**, 053013 (2016).

8. P. Wozniak, P. Banzer, **F. Bouchard**, E. Karimi, G. Leuchs and R. W. Boyd, "Tighter spots of light with superposed orbital angular momentum beams," *Physical Review A* **94**, 021803 (2016).

9. **F. Bouchard**, H. Larocque, A. M. Yao, C. Travis, I. De Leon, A. Rubano, E. Karimi, G. Oppo, R. W. Boyd, "Polarization shaping for control of nonlinear propagation," arXiv:1606.05010 (2016).

10. H. Larocque, J. Gagnon-Bischoff, **F. Bouchard**, R. Fickler, J. Upham, R. W. Boyd, E. Karimi, "Arbitrary optical wavefront shaping via spin-to-orbit coupling," arXiv:1608.06603 (2016).

Statement of originality and collaborative contributions

To the best of his knowledge, the author states that the work described in this Master's thesis constitute original research in the field of physics. Below, we provide the collaborative contributions of each participant for every chapters.

Ebrahim Karimi initiated the work of chapter 2. Mohammad Mirhosseini performed the structure's design. F. Bouchard and E. Karimi designed the experiment. F. Bouchard and Harjaspreet Mand performed the experiment. F. Bouchard analyzed the data. Robert W. Boyd and E. Karimi supervised all aspects of the project. All authors contributed to the text of the manuscript.

Ebrahim Karimi initiated the work of chapter 3. F. Bouchard and E. Karimi developed the theoretical model. Ali Akbar Ahangary performed the experiment. Enrico Santamato, E. Karimi and Hamid Reza Khalesifard supervised all aspects of the project. All authors contributed to the text of the manuscript.

Ebrahim Karimi initiated the work of chapter 4. Israel De Leon performed the structure's design and numerical analysis. Sebastian A. Schulz and Jeremy Upham fabricated the samples. F. Bouchard performed the experiment and analyzed the data. Robert W. Boyd and E. Karimi supervised all aspects of the project. All authors contributed to the text of the manuscript.

Ebrahim Karimi initiated the work of chapter 5. F. Bouchard and E. Karimi designed the experiment. F. Bouchard performed the numerical analysis. F. Bouchard performed the experiment and analyzed the data. Jérémie Harris and Harjaspreet Mand helped with the experiment. Robert W. Boyd and E. Karimi supervised all aspects of the project. All authors contributed to the text of the manuscript.

Ebrahim Karimi and Enrico Santamato initiated the work of chapter 6. F. Bouchard and E. Karimi designed the experiment. Jérémie Harris performed the

numerical analysis. F. Bouchard performed the experiment and analyzed the data. Jérémie Harris, Harjaspreet Mand and Nicolas Bent helped with the experiment. E. Santamato, Robert W. Boyd and E. Karimi supervised all aspects of the project. All authors contributed to the text of the manuscript.

List of Figures

Chapter 1

Introduction

Light has long been a fascinating subject among those scientists trying to understand the world in which they live in. Historically, the way we described light has repeatedly oscillated between a wave and particle description. Interference and diffraction of light beams are direct consequences of the wave nature of light. However, one can also associate particle-like characteristics, such as energy and linear momentum, to light. In this description, the aforementioned properties are associated individually to single particles of light, namely photons, where the energy and the linear momentum of a single photon are respectively given by its frequency and its wavevector, in units of the reduced Planck constant, $\hbar$.

Interestingly, photons may possess further particle-like properties, such as angular momentum. Traditionally, in the paraxial regime it is convenient to separate angular momentum into two components, i.e. a spin angular momentum component and an orbital angular momentum component. In analogy with planets orbiting the sun in our solar system, spin angular momentum would be given by the rotation of planets on themselves. On the other hand, the planets rotating around the sun would carry an orbital angular momentum. Intuitively, one may see how these two types of rotations are intrinsically different and how a single particle, e.g. a planet in the case of the solar system, may carry both types of angular momentum independently. Surprisingly, light particles also behave in the same manner when it comes to angular momentum. For one thing, spin and orbital angular momentum result from completely different features of light. Optical spin angular momentum is associated to the vectorial nature of light, whereas optical orbital angular momentum is related to the wavefront and transverse spatial modes of light. More precisely, left- and right-handed circularly polarized light will carry a spin angular momentum of $\hbar$ and $-\hbar$ per photon along

their propagation direction, respectively. In analogy to spin angular momentum, light beams with $|\ell|$ intertwined helical wavefronts will carry an orbital angular momentum value of $\ell\hbar$ per photon along their propagation direction, where the sign of ℓ is determined by the handedness of the twisted wavefronts. In this thesis we are mainly interested in the properties of light carrying orbital angular momentum, also referred to as "twisted light", both at the classical and quantum regime.

Twisted light may be generated using different techniques. The main characteristic of twisted light is its helical wavefront corresponding to an azimuthal phase profile. Hence, using a phase-plate with an appropriate azimuthal dependent optical-path-length yields an output beam with a helical wavefront. This type of device is called a *spiral phase plate* and is conceptually similar to a lens. In the case of a lens, the thickness is radially dependent rather than azimuthal. For a specific type of twisted light ($\ell = 1$), such devices would have an optical thickness variation of λ between the azimuthal position of 0 and 2π, where λ is the wavelength of the input field, thus making this technique wavelength-dependent. Another useful and versatile method of generating beams with a given phase profile is called holography. Typically, pitch-fork gratings can be used to generate twisted light, where the period of the grating will depend on the wavelength of the input beam and the desired diffraction angle. Lastly, liquid-crystal devices that imprint a phase distribution on an optical field may also be used to generate twisted light, where the phase retardation of the liquid-crystals may be tuned according to the wavelength of the beam. Hence, monochromatic twisted light beams may be efficiently generated using the aforementioned techniques, but there is a lack of devices achieving broadband generation of orbital angular momentum. In chapter 2, we proposed a novel device capable of generating achromatic twisted light. The device, working under the principle of a geometric phase given by total internal reflection, was further fabricated and characterized with three different light sources of different wavelength, namely red, green and blue. Applications in astronomy are further discussed in this chapter.

Wavefront shaping using the concept of geometric phases, as it is the case in the chapter on broadband generation of twisted light, may be realized with a wide range of techniques. In principle, any birefringent media in addition with the ability of organizing its transverse structure may lead to the generation of twisted light. Moreover, this technique using geometric phases is of particular interest as it couples spin angular momentum (polarisation) to orbital angular momentum. Such photonic spin-to-orbit coupling can be realized in a variety of anisotropic and isotropic media.

One interesting case in which we will draw our attention in chapter 3 is the case of laser-induced birefringence. By illuminating a specific type of material, it is possible to induce birefringence due to thermally-induced stress, leading to generation of twisted light. In this chapter, we will discuss the dynamics of such processes for different regimes of illumination.

We conclude the section on the generation of twisted light of this thesis by noting that the devices mentioned previously for generation of light carrying orbital angular momentum are in general fairly bulky and not appropriate for integrated optics. In chapter 4, we propose a novel method of generating twisted light at the microscopic level using a meta-surface consisting of structurally arranged nano-antennas. This method also supports spin-to-orbit coupling allowing for generation of structured light beams at a much smaller scale. Moreover, our fabricated metasurfaces would support the generation of orbital angular momentum with values ranging from -25 to 25. Such a wide range of orbital angular momentum values would allow for super-dense coding, nano-scale sensing, high-dimensional quantum key distribution and quantum information into integrated devices.

The second part of this thesis deals with the dynamics of twisted light as it evolves in time and space, both at the classical and quantum level. In the language of optics, this is typically referred to as propagation. Hence, we study several interesting properties of twisted light beams as they undergo free-space propagation. In chapter 5, we manipulate classical pulses of light to reveal the distinct velocity of twisted light with various orbital angular momentum values. We propose and experimentally verify that such pulses would exhibit subluminal group velocities, i.e. slower than the physical constant c representing the speed of light in vacuum. This decrease in group velocity results from the degree of twisting of the wavefront of the optical pulses. At the quantum level, twisted light with different orbital angular momentum values can be used as proper quantum states of photons, which has many applications in quantum communication and cryptography. Most schemes in quantum information rely on the preservation of the quantum information stored in the orbital angular momentum degree of freedom of single photons. In chapter 6, we show that the orbital angular momentum degree of freedom may couple to additional internal degrees of freedom, e.g. radial, leading to losses in quantum information of the systems. We further propose a method to retrieve the lost quantum information which we name *quantum recoherence*.

Chapter 2

Broadband generation of twisted light

This chapter is based on the following paper:

1. **F. Bouchard**, H. Mand, M. Mirhosseini, E. Karimi, and R. W. Boyd, "Achromatic orbital angular momentum generator," *New Journal of Physics* **16**, 123006 (2014).

2.1 Introduction to orbital angular momentum of light

A scalar paraxial optical field, $\Psi(\mathbf{r},t)$, may be described by an amplitude $A(\mathbf{r},t)$ and a phase $\Phi(\mathbf{r},t)$, where $\Psi(\mathbf{r},t) = A(\mathbf{r},t)\, e^{i\Phi(\mathbf{r},t)}$. It was recognize by *Allen et al.* [1] that optical fields with phase terms $\exp(i\ell\varphi)$ carry an orbital angular momentum of $\ell\hbar$ per photon along their propagation direction, where ℓ is an integer and φ is the azimuthal coordinate in the transverse plane of the field. This can be intuitively recognized from the fact that, in quantum mechanics, $\exp(im\varphi)$ represents eigenfunctions of the z-component of the orbital angular momentum momentum operator $\hat{L}_z = -i\hbar\frac{\partial}{\partial\varphi}$, with eigenvalues $m\hbar$, where m is traditionally referred to as the magnetic quantum number [2]. Hence, in analogy to the quantum theory of angular momentum, one may interpret ℓ as being the orbital angular momentum value carried by a single photon along its propagation direction, in units of $\hbar$. Such beams possess a wavefront forming intertwined helices (See Fig 2.1). These eigenfunctions represent a complete

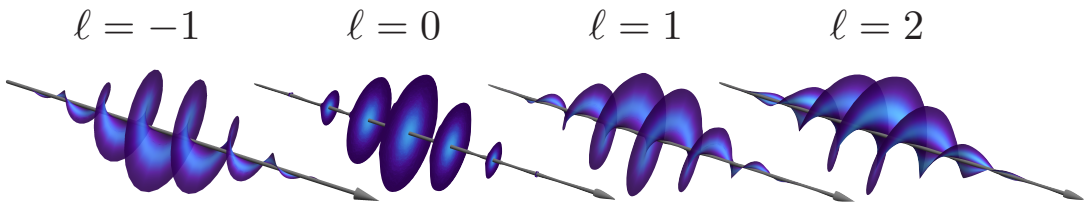

Figure 2.1: **Wavefront of twisted beams**. The wavefront of a twisted beam is given by $|\ell|$ intertwined helices, where the handedness of the helices is given by the sign of the OAM value ℓ.

and orthogonal set of modes from which any arbitrary angle-dependent functions can be expanded [3]. Thus, these orbital angular momentum eigenfunctions represent a useful basis in which one may express quantum states of single photons.

Such phase terms can be found in several solutions of the paraxial wave equation. The paraxial wave equation is obtained from the scalar wave equation in the approximation of propagating beams with beam sizes much larger than their wavelengths, and dictates the propagation of such beams. In the presence of a cylindrical symmetry, the natural set of solutions for the paraxial wave equation is given by the Laguerre-Gauss (LG) modes, in cylindrical coordinates [4]. These modes are labelled by an azimuthal and a radial index respectively given by p and ℓ, where p is a positive integer and ℓ is an integer. Here, $\mathrm{LG}_{p,\ell}$ modes are of particular interest due to their azimuthal phase dependence, i.e. $\mathrm{LG}_{p,\ell}(r,\varphi) \propto \exp(i\ell\varphi)$. Thus, due to the completeness of LG modes, any beam may, in general, be expressed as a superposition of different p and ℓ indices, i.e. $\sum_{p,\ell} c_{p,\ell}\mathrm{LG}_{p,\ell}(r,\varphi)$, where $c_{p,\ell}$ are complex coefficients.

2.2 Generation of twisted light

In order to generate twisted light, one needs the ability to imprint a specific phase pattern onto a light beam. In this section, we will outline some of the main methods currently used to do so and provide some of their limitations.

2.2.1 Optical path length

The conceptually most straightforward way of imprinting a specific phase profile onto an optical field is by varying the relative optical path length (OPL) of the beam at

different positions in its transverse plane, where the OPL is obtained by multiplying the distance of the path light follows d, and the refractive index of the medium in which light propagate n, i.e. OPL $= nd$. More precisely, the resulting phase shift $\Delta\Phi$ is given by the OPL with the following relation, i.e. $\Delta\Phi = 2\pi nd/\lambda$, where λ is the wavelength of the light beam. In the context of this chapter, it is noteworthy to mention that the phase shift induced by the difference in OPL depends directly on the wavelength of the input beam.

Hence, the OPL may be adjusted by either varying the thickness or the refractive index of a medium. The former can in general be done in any homogeneous and isotropic media such as glass. The specific device that achieves generation of twisted light using this principle is referred to as a *spiral phase plate* [5]. An example of materials which have a variable refractive index is given by liquid crystals. The refractive index of liquid crystals may be electrically or thermally tuned by either applying a voltage or varying their temperature, respectively. One particularly useful device that can be used to dynamically control the refractive index of liquid crystals is a *spatial light modulator* (SLM). An SLM consists of a pixelated array of liquid crystal materials that can be controlled by applying an independent voltage to each pixel.

2.2.2 Holography

Holography is an optical method that allows one to imprint an arbitrary phase profile to an optical beam. For the sake of simplicity, we will limit our treatment to the generation of light carrying orbital angular momentum, although beams with arbitrary phase profiles may be generated by this technique. In order to understand the underlying physics of holography in this context, let us consider the interference between two coherent sources of light. In the first place, we consider a reference plane wave propagating in the z-direction, $\Psi^{(0)}(\mathbf{r}) = A_0 \exp(ikz)$, where A_0 is a constant and $k = 2\pi/\lambda$ is the magnitude of its wavevector. The second interfering beam is given by a twisted beam of orbital angular momentum value ℓ propagating with an incident angle β, i.e. $\Psi^{(\ell)}(\mathbf{r}) = A_0 \exp(i\ell\varphi) \exp(i(k_x x + k_z z))$, where $k_z = k\cos\beta$ and $k_x = k\sin\beta$. At the plane of $z = 0$ the interference between the beams is given by the following intensity,

$$\frac{1}{2}\left|\Psi^{(0)}(\mathbf{r}) + \Psi^{(\ell)}(\mathbf{r})\right|^2 = A_0^2\left[1 + \cos\left(\ell\varphi + \frac{2\pi}{\lambda}\sin(\beta)x\right)\right]. \tag{2.1}$$

From this interference pattern, one may then fabricate either an amplitude or a phase hologram, where the phase hologram usually yields much higher efficiencies [6]. Illuminating the hologram with a plane wave then result in the generation of an optical field with the characteristics of the interfering twisted beam mentioned above. This technique is extremely useful as phase holograms may be straightforwardly realized with spatial light modulators and can further be manipulated dynamically. Once more, we notice that the hologram pattern will depend on the wavelength of the input beam, making this technique limited to rather monochromatic beams.

2.2.3 Geometric phase

Geometric phases are interesting in the study of quantum systems evolving adiabatically along closed trajectories. This fundamental concept in quantum mechanics may be extended and used to our benefit in optical systems when considering the evolution of polarisation states of light. It is convenient at this point to introduce the Poincaré sphere as a physical representation of polarisation states of light. This representation can further be extended to any arbitrary bidimensional quantum systems as we will see in later chapters. A polarisation state of light is then represented as a point on a unit sphere. The poles represent the circular polarisation states with left and right handedness lying at the north and south poles, respectively. On the equator lie the linear polarisation states such as horizontal, vertical, diagonal, anti-diagonal, etc. The azimuthal position of these states on the equator corresponds to the relative phase between the left- and right-circular polarisation components. All other points on the Poincaré sphere would then represent elliptical states of light with various orientations and ellipticities. In the case of polarisation, the acquired geometric phase of a polarisation state undergoing a closed-loop trajectory on the Poincaré sphere will be equal to half the solid angle surrounded by the outlined trajectory. This is an ingenious mean by which one may imprint a polarisation dependent phase on an optical beam, leading to interesting effects such as spin-to-orbit coupling.

One extremely useful device that allows one to generate orbital angular momentum using the principle of geometric phases is the *q-plate* [7]. A q-plate consists of a liquid-crystal device where the optical axis of the liquid-crystals are arranged in the transverse plane of an input beam. The liquid-crystals may be tuned in order to achieve any arbitrary optical retardation, δ, ranging from zero to a half-wavelength. In order to generate a beam carrying an orbital angular momentum value of ℓ, the q-plate is first tuned to act as a half-wave plate with $\delta = \pi$. The plate is then illuminated

with a circularly polarized beam, say left-circular. The action of the half-wave plate is to convert left-circular polarisation into right-circular polarisation, thus displacing the polarisation state from the north pole to the south pole of the Poincaré sphere. The path taken by the polarisation state will be dictated by the orientation of the liquid-crystal's optical axis, α. Thus the phase difference of two beams undertaking different trajectories on the Poincaré sphere will be given by half the solid angle enclosed by their trajectories. This argument still holds for a single beam illuminating a q-plate that has different optical axis of the birefringent medium at different points in the transverse plane of the beam. Any arbitrary phase profile $\Phi(r, \varphi)$ can be obtained by adjusting the optical axis $\alpha(r, \varphi)$, where $\Phi(r, \varphi) = 2\alpha(r, \varphi)$. Finally, one may note that this method is independent of the wavelength of the input beam, as it is only dependent on the orientation of the optical axis of the birefringent medium. However, this method requires the birefringent medium to possess an optical retardation of $\delta = \pi$. This is typically done by using an isotropic birefringent medium with a wavelength dependent optical retardation, $\delta = 2\pi\Delta n d/\lambda$, where Δn is the birefringence and d is the thickness of the medium. This motivates the work presented in this chapter proposing a novel device for twisted light generation using a geometric phase element with a wavelength independent optical retardation.

2.3 Detection of twisted light

In general, there are different methods that allow one to detect twisted light. This can be done by revealing the phase profile of the optical beam through an interferometric method, as can be seen in the following chapters [6]. The interference pattern of a twisted light beam with a reference plane wave is given by a characteristic pitch-fork pattern. This allows for a qualitative detection of twisted light. A more quantitative technique to measure the orbital angular momentum content of an optical beam can essentially be done using any of the devices used to generate twisted light. For an optical field with a phase profile of $\exp(i\ell\varphi)$, one needs to imprint the opposite phase of $\exp(-i\ell\varphi)$, leaving the output beam as a plane wavefront with $\ell = 0$. One may then project on the $\ell = 0$ mode using a single mode optical fibre (SMOF). This process is referred to as *phase-flattening* and can be performed using any of the technique listed above [8, 9]. Moreover, this technique can be done coherently to achieve detection of any arbitrary orbital angular momentum superposition states of light. This technique of phase-flattening is widely used both in the classical and quantum regime.

New Journal of Physics
The open access journal at the forefront of physics
Deutsche Physikalische Gesellschaft DPG | IOP Institute of Physics

Achromatic orbital angular momentum generator

Frédéric Bouchard[1], Harjaspreet Mand[1], Mohammad Mirhosseini[2], Ebrahim Karimi[1] and Robert W Boyd[1,2]

[1] Department of Physics, University of Ottawa, 25 Templeton, Ottawa, Ontario, K1N 6N5 Canada
[2] Institute of Optics, University of Rochester, Rochester, New York, 14627, USA
E-mail: ekarimi@uottawa.com

Received 7 September 2014, revised 14 October 2014
Accepted for publication 24 October 2014
Published 2 December 2014

New Journal of Physics **16** (2014) 123006

doi:10.1088/1367-2630/16/12/123006

Abstract

We describe a novel approach for generating light beams that carry orbital angular momentum (OAM) by means of total internal reflection in an isotropic medium. A continuous space-varying cylindrically symmetric reflector, in the form of *two glued hollow axicons*, is used to introduce a nonuniform rotation of polarization into a linearly polarized input beam. This device acts as a full spin-to-orbital angular momentum convertor. It functions by switching the helicity of the incoming beam's polarization, and by conservation of total angular momentum thereby generates a well-defined value of OAM. Our device is broadband, since the phase shift due to total internal reflection is nearly independent of wavelength. We verify the broad-band behaviour by measuring the conversion efficiency of the device for three different wavelengths corresponding to the RGB colours, red, green and blue. An average conversion efficiency of 95% for these three different wavelengths is observed. This device may find applications in imaging from micro- to astronomical systems where a white vortex beam is needed.

Keywords: light orbital angular momentum, spin angular momentum, total internal reflection

Content from this work may be used under the terms of the Creative Commons Attribution 3.0 licence. Any further distribution of this work must maintain attribution to the author(s) and the title of the work, journal citation and DOI.

© 2014 IOP Publishing Ltd and Deutsche Physikalische Gesellschaft

1. Introduction

Optical orbital angular momentum (OAM), corresponding to a helical phase-front of a light beam, finds numerous applications in many research areas such as imaging systems, lithography techniques, optical tweezers, and quantum information [1–5]. Marvelously, it provides multidimensional encoding onto a single photon for classical and quantum communications, which is being used for increasing the communication channel capacity [6–10]. However, the methods used to generate and manipulate the OAM have been substantially restricted to a few techniques that can be listed as (i) spiral phase plates (inhomogeneous dielectric media), (ii) holographic techniques, (iii) astigmatic mode converters and (iv) spin-to-orbit coupling in an inhomogeneous birefringent medium [11–15]. Several fundamentally different concepts have also been proposed and exploited to generate OAM, such as internal conical reflection in biaxial crystals and reflection from a metallic cone reflector [16, 17]. Almost all methods are wavelength dependent, and do not yield a broadband OAM generator. However, the existence of an achromatic OAM generator would open up new possibilities for imaging techniques such as the optical vortex coronagraph. In the optical vortex coronagraph, the background light is suppressed by means of a spiral phase plate which generates an OAM value of 2. However, spiral phase plates are wavelength dependent and thus analyzing a polychromatic astronomical object is not feasible. An achromatic OAM generator with an OAM value of 2 would lead to analysis of *white* astronomical objects [18]. Recently, Zhang and Qui proposed a technique based on total internal reflection to generate achromatic radial and azimuthal polarized light beams [19].

It has been well-established that a light beam under conditions of total internal reflection acquires an incident-angle-dependent phase change, which does not exist for light going from a lower to a denser medium [20]. Such behaviour triggered *Augustin-Jean Fresnel* to propose and design an achromatic wave retarder in 1817 that can be used to modify the polarization state of light; specifically he invented a broadband quarter-wave plate, now referred to as the *Fresnel rhomb* [20]. The refractive index for most isotropic transparent media varies very slowly in wavelength. For instance, the refractive index of commercial N-BK7 decreases with optical wavelength at a rate of $dn/d\lambda = -0.0124\ \mu m^{-1}$. The retardation of commercial half-wave Fresnel rhombs made of N-BK7 is 0.5089λ, 0.4963λ and 0.4923λ at wavelengths of 400 nm, 1000 nm and 1550 nm, respectively[3]. This indeed leads to an achromatic wave-retarder that does not depend on the input beam's wavelength. There are two ways to adjust the phase retardation under conditions of total internal reflection: (1) adjusting the beam's incident angle and (2) implementing a sequence of reflections that overall leads to a global phase equal to the sum of each phase retardation introduced by each reflection. Therefore, one can achieve any specific phase delay between transverse electric (TE, sagittal plane polarization) and transverse magnetic (TM, tangential plane polarization) polarizations via a sequence of total internal reflections.

In this article, we propose a novel design to generate an OAM value of ± 2 from a circularly polarized light beam via total internal reflection in a cylindrically symmetric Fresnel rhomb-like system. A well-designed two-Fresnel-rhomb system works as a half-wave plate,

[3] These data were taken from manufactured Fresnel rhombs (Product number of FR600HM) with N-BK7 martial form Thorlabs company.

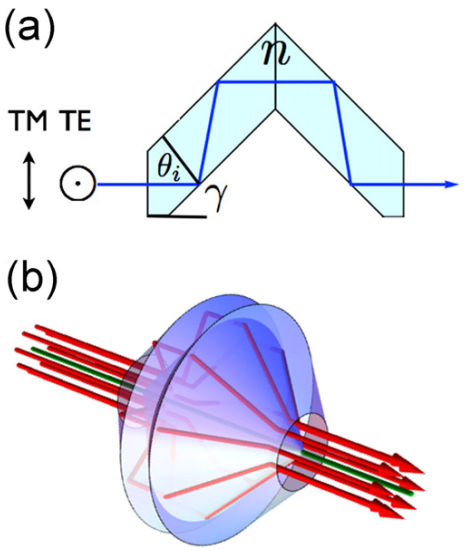

Figure 1. (a) Schematic sketch of two attached Fresnel rhombs. The relative phase change between TE and TM polarization after four appropriately designed reflections is π radians. (b) The three-dimensional graphical design of our device, which is a surface of revolution formed by rotating the design of part (a) about its optical axis. It is made of two glued truncated hollow axicons.

which flips the helicity of input circularly polarized beam fairly independently of the beam's wavelength. Since the system is cylindrically symmetric, we would not expect any changes in the total value of angular momenta, i.e. spin+OAM. Therefore, the output light beam gains additional OAM of $\pm 2\hbar$ per photon, where the sign depends on the helicity of the input beam; $\hbar$ is the reduced Planck constant. However it is worth noticing that higher OAM values can be generated via cascading these devices with appropriate wave plates, e.g. cascading two such devices with an intermediate half-wave plate generates OAM values of ± 4.

2. Theory

2.1. Total internal reflection

Let us assume that a light beam undergoes total internal reflection at the surface of a medium having a relative refractive index of n (see figure 1(a)). The relative phase change between the two polarization components TE and TM is given by

$$\delta = 2 \arctan\left(\frac{\cos\left(\theta_i\right)\sqrt{\sin\left(\theta_i\right)^2 - n^2}}{\sin\left(\theta_i\right)^2} \right), \tag{1}$$

where θ_i is the angle of incidence [20]. The beam acquires a total relative phase change between these orthogonal polarizations for a sequence of total internal reflections inside the dielectric given by the following Jones matrix:

$$\mathcal{J}_0 = \begin{pmatrix} 1 & 0 \\ 0 & e^{i\delta} \end{pmatrix}. \tag{2}$$

In this expression, δ is the *relative* phase change between two polarization states after all reflections, which is a function of initial incidence angle, i.e. $\delta := \delta(\theta_i, n)$.

The relative angle between the reflective surface and the incoming polarization defines the *birefringence angle* α, which is analogous to the orientation angle of the fast axis in a wave plate. Therefore, the polarization of the incoming beam after passing through the medium is modified by the orientation of the surface. The polarization dependent phase shift corresponding to a rotated surface can be calculated by means of the Jones calculus: $\mathcal{J}_\alpha = R(-\alpha) \cdot \mathcal{J}_0 \cdot R(\alpha)$, where $R(\alpha)$ is a 2×2 rotation matrix[4]. Reflection from a flat surface implies a uniform phase variation for a set of parallel rays; instead a curved surface introduces a nonuniform phase change. This nonuniform phase alteration comes from the nonuniformity of the *birefringence angle*, α, introduced by the curved surface. Thus, it gives rise to a nonuniform rotation of polarization, e.g. a linearly polarized beam is transformed into a specific polarization topology. The Jones operator of an infinitesimal reflective surface at angle α with respect to a fixed reference, say for example the horizontal axis, in the circular polarization basis, is given by:

$$\mathcal{J}_\alpha = \begin{pmatrix} \cos\left(\frac{\delta(\theta_i, n)}{2}\right) & i \sin\left(\frac{\delta(\theta_i, n)}{2}\right) e^{-2i\alpha} \\ i \sin\left(\frac{\delta(\theta_i, n)}{2}\right) e^{2i\alpha} & \cos\left(\frac{\delta(\theta_i, n)}{2}\right) \end{pmatrix}. \tag{3}$$

In general, α depends on the transverse coordinates, e.g. $\alpha := \alpha(r, \phi)$ in polar coordinates. However, in our case we assume that the angle of the reflective surface is only a function of the azimuthal angle, i.e. $\alpha(\phi) = q\,\phi$, where q is an integer or half-integer constant defined as the topological charge. A completely cylindrically symmetric reflective surface, such as that in figure 1(b), possesses a unit topological charge, i.e. $\alpha(\phi) = \phi$. This optic, consisting of two glued hollow axicons, generates light OAM of $\ell = \pm 2$, where the sign depends on the input polarization state. Let us assume a left-handed circularly polarized input beam, i.e. $|L\rangle = (1, 0)^T$, where T stands for transpose operator. Then, the emerging beam can be split into two parts using equation (3), $\cos\left(\frac{1}{2}\,\delta(\theta_i, n)\right)|L\rangle + i \sin\left(\frac{1}{2}\,\delta(\theta_i, n)\right) e^{2i\phi}\,|R\rangle$, and in a similar manner it transforms a right-handed circularly polarized beam, i.e. $|R\rangle = (0, 1)^T$, into $\cos\left(\frac{1}{2}\,\delta(\theta_i, n)\right)|R\rangle + i \sin\left(\frac{1}{2}\,\delta(\theta_i, n)\right) e^{-2i\phi}\,|L\rangle$. Thus the output polarization, as one would expect, depends on the relative optical retardation between the TE and TM polarizations. Importantly, when it is designed to behave as a half-wave plate, i.e. $\delta = \pi$, the device does transform a left-circularly polarized beam into a right-circularly polarized beam with an OAM value of $\ell = +2$. Inversely, it transforms the right-circularly polarized beam into a left-circularly polarized beam, and gains an OAM value of $\ell = -2$. A circularly polarized light beam carries angular momentum of $\pm\hbar$ per photon. Since the device is cylindrically symmetric there should be no exchange of angular momenta with the device. In the first case, assuming a left-circularly polarized TEM_{00} input beam, the total value of angular momentum is $+\hbar$ since SAM $= +\hbar$ and

[4] Active 2×2 rotation matrix about z-axes is $R(\alpha) = \begin{bmatrix} \cos\alpha & \sin\alpha \\ -\sin\alpha & \cos\alpha \end{bmatrix}$.

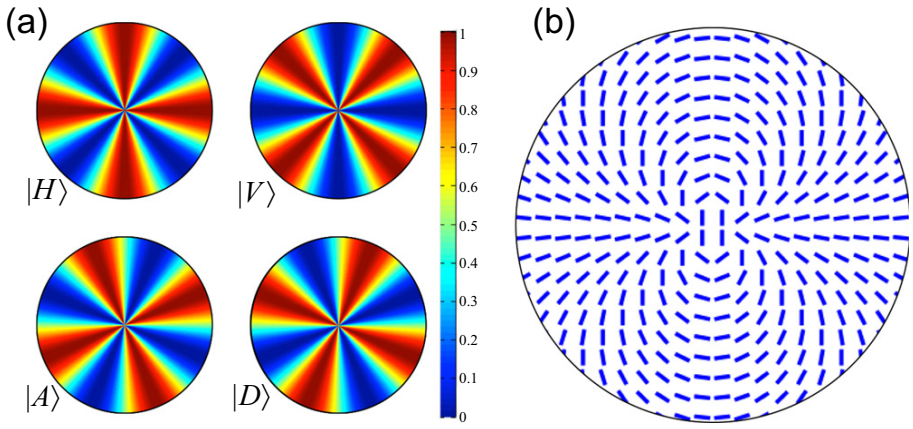

Figure 2. (a) Intensity profile of the generated vector beam described in section 2.2 after passing through a linear polarizer oriented in horizontal, vertical, diagonal and anti-diagonal directions, respectively. (b) Transverse polarization pattern of the generated vector beam when the device is illuminated with a horizontally polarized input beam.

OAM = 0. The device inverts the polarization helicity into $-\hbar$, and therefore gains an OAM of $+\hbar - (-\hbar) = +2\hbar$, since total angular momentum must be conserved. Instead, for the case of a right-circularly polarized input beam, the sign changes to a negative. Indeed, the device works as a full spin-to-orbital angular momentum converter. The physics of this effect lies at the heart of a well-known quantum phenomena known as the geometric phase, where the polarization state of photons evolves adiabatically in the Hilbert space, and it acquires an additional phase that is given by geometrical features of the Hilbert space. For our case, this geometrical phase is proportional to half of the solid angle of the evolution path in the polarization Poincaré sphere [21]. This feature has already been well-investigated in a patterned dielectric, a patterned liquid crystal cell device, and very recently in a patterned plasmonic metasurface [22–24].

2.2. Vector vortex beam

The achromatic spin-to-orbital angular momentum coupler with a specific optical retardation value of π can also be used to generate a vector vortex beam. These types of beams have specific nonuniform transverse polarization patterns. A subclass of these beams, cylindrical vector beams, corresponds to a superposition of two circularly polarized light beams with opposite OAM values, i.e. $|L\rangle \exp(-i\ell\phi) + e^{i\gamma}|R\rangle \exp(+i\ell\phi)$, where γ is a relative phase between these two beams. In the case of $|\ell| = 2$, these beams can be generated by feeding our device with a linearly polarized input beam. In the circular polarization basis, linear polarization states can be expressed as the following superposition states: $|\theta\rangle = (e^{-i\theta}|L\rangle + e^{i\theta}|R\rangle)/\sqrt{2}$, where θ is the angle of linear polarization with respect to the horizontal axis. If we apply the Jones operator $\mathcal{J}_\alpha$ to a specific linear polarization state, e.g. horizontal polarization $|H\rangle := |\theta = 0\rangle$, we obtain the following output polarization state:

$$\mathcal{J}_\alpha \cdot |H\rangle = \cos(2\phi)|H\rangle + \sin(2\phi)|V\rangle, \tag{4}$$

where a $\pi/2$ global phase is omitted. In this case we obtain a specific transverse polarization pattern as described in figure 2(b). It is possible to reconstruct this polarization pattern by

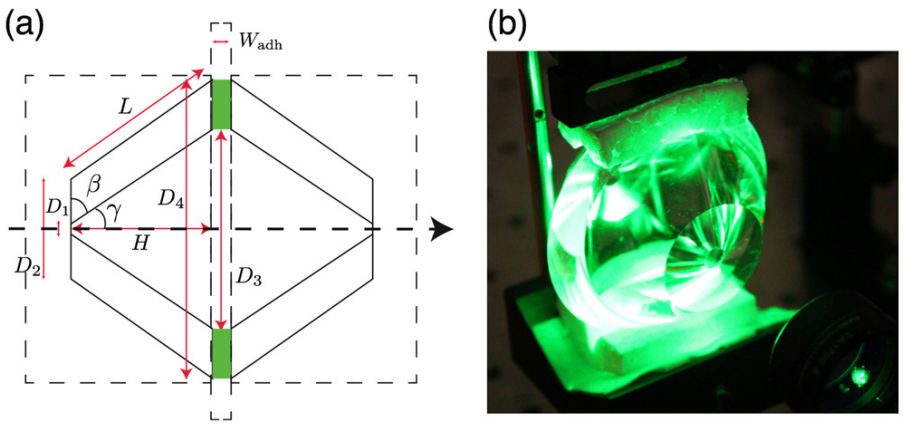

Figure 3. (a) Two-dimensional schematic of the angular cone. Legend: γ is the half-angle of the cone; β is the complementary angle with respect to γ; W_{adh} is the adhesive layer thickness; H and L are the height and lateral height of the truncated cone; D_1 and D_2 are the inner and outer diameters of the annulus at the small end of the cone, and D_3 and D_4 are the inner and outer diameters of the annulus at the large end of the cone, respectively. (b) Photo of the manufactured device when illuminated by a green diode laser.

performing polarization state tomography, where we measure the intensity of different polarization states using a sequence of a quarter-wave plate and a half-wave plate followed by a polarizing beam splitter. Furthermore, one can determine the OAM value from these types of measurements, as it can be shown that the number *intensity petals* (number of maxima) in the transverse profile is equal to twice the OAM value.

The retardation introduced by the reflections, i.e. $\delta(\theta_i, n)$, can be intentionally adjusted to not impose a full spin-to-orbital angular momentum conversion. Therefore, a fraction of the (circularly polarized) beam given by $\eta = \left|\sin\left(\frac{1}{2}\delta(\theta_i, n)\right)\right|^2$ undergoes the full spin-to-orbital angular momentum conversion, where its polarization flips to opposite handedness and gains an OAM value of $|\ell| = 2$. The remaining part, $1 - \eta$, does not go through the spin-to-orbital angular momentum conversion process, and thus possesses the same polarization and OAM value as the input beam. Implementing specific retardations, in particular having a power balance between spin-to-orbital and non–spin-to-orbital angular momentum converted photons (i.e. $\eta = 1/2$), leads to complex transverse polarization patterns called '*polarization-singular beams*' or '*Poincaré beams*' [25, 26]. This condition requires a static design of the device, for instance by changing the dielectric material or the cone angle, and cannot be adjusted dynamically.

Due to the presence of the *surface singularity* on the axis of the device (D_1 in figure 3(a)), a small portion of the beam near this region is scattered out. Thus, the transmitted beam possesses a doughnut shape at the exit face of the device. Nevertheless, since the emerging beam carries an OAM value of ± 2, this doughnut shape remains unchanged by free-space propagation. The acceptance aperture of the truncated outer cone, D_2 in figure 3(a), introduces further diffraction on the beam, which affects the beam's radial shape similar to that presented in most OAM generators [27]. It is worth noticing that both effects are present in all OAM

Table 1. Specifications of the device parameters. Δn is the maximum tolerable refractive-index mismatch between the PMMA and the adhesive layer.

Description	Value	Tolerance
n @ 633 nm	1.497	±0.001
β	51.78°	±0.1°
γ	38.22°	±0.1°
D_1	6 mm	±0.1 mm
D_2	30 mm	±0.1 mm
D_3	43.7 mm	±0.1 mm
D_4	67.7 mm	±0.1 mm
H	23.94 mm	±0.1 mm
L	30.47 mm	±0.1 mm
W_{adh}	$\leqslant 25\,\mu$m	5 μm
Δn	$\leqslant 0.1$	

generator devices, except for the cylindrical mode convertor that transfers the cartesian laser cavity modes, i.e. Hermite–Gaussian, into the cylindrical solution of Laguerre–Gaussian modes [14]. Furthermore, the emerging beam undergoes a type of radial astigmatism, since the rays close to the center traverse faster than the rays at the periphery for an imperfectly collimated beam. However, this radial astigmatism can be compensated by adding a radially shaped pattern to the input and output ports of the device.

3. Design

The device is made of polymethyl methacrylate (PMMA) and takes the form of two hollow cones, where the inner surface is removed by diamond turning. This approach allows us to reach a 'singularity diameter' as small as $D_1 = 6$ mm, without introducing any deleterious effects. In order to reduce any thermal birefringence, the cast acrylic was held at a constant temperature during the diamond turning process. Specifications of the fabrication of the device are given in table 1, whereas the various quantities are defined in figure 3. These parameters provide a clear aperture about 24 mm. The two cones were attached to one another by a UV-curable adhesive with a thickness of (0.025 ± 0.005) mm, and a refractive index close to that of cast acrylic. However, some inhomogeneities were observed due to nonuniformity of the applied adhesive at the cone's interface.

4. Results and discussion

As described in more detail below, we have experimentally demonstrated that the fabricated achromatic spin-to-orbital angular momentum coupler generates a light beam carrying an OAM value of $\ell = \pm 2$. We examine the beam emerging from the device by performing polarization projective measurements, where the nature of spin-to-orbital angular momentum coupling is used to analyze the output beam. In our analysis, the device is illuminated with different polarization states, which are a superposition of states in the circular polarization basis. In

addition to this, we have also measured the OAM spectrum of the emerging beam for different input polarization states. This is performed by means of OAM state tomography in which the output beam was projected onto different OAM basis and then the corresponding OAM density matrix was measured. Furthermore, we show generation of a vector vortex beam where the polarization undergoes a full rotation as we go through a full cycle around the beam's axis. The transverse polarization pattern of the vector beam is determined by measuring the reduced Stokes parameters [28].

4.1. Examining the device with a laser source

Fabrication limitations encountered in this experiment consist of a central circular orifice and of an annular region where light is not transmitted, called the *dead zone*. The part of the beam that is transmitted through the central opening does not undergo the sequence of total internal reflections that lead to spin-to-orbital angular momentum coupling. This central non-converted region of the output beam can be filtered out with a sequence of a quarter-wave plate and a polarizing beam splitter, since the converted and non-converted beams have orthogonal polarizations. Only the outer annular region leads to spin-to-orbital angular momentum coupling, thus generating a beam carrying orbital angular momentum or a vector vortex beam.

Because we do not have access to the entire transverse profile of the output beam, the characteristic doughnut-shaped intensity profile is not visible. Thus, we determine the OAM value by using projective measurements on a generated vector beam with a horizontally polarized input beam. In the case of a spin-to-orbital angular momentum coupling device with a unit topological charge, we would expect to see a *cross pattern* after projecting the outgoing beam onto a linear polarizer. In general, the number of bright regions in the transverse intensity profile of the projective measurement, i.e. petals, is twice that of the OAM value of the beam. Rotating the polarizer causes a rotation onto the four-fold petal pattern. This set of polarization projective measurements constitutes an accurate means of determining the OAM value of an output beam in the case of a circularly polarized input beam. Furthermore, the reduced Stokes parameters, which are necessary to reconstruct the polarization pattern of the vector vortex beam, can be calculated from this set of measurements.

To show the broadband performance of the device, we perform polarization projective measurements for three different laser sources; namely red, green and blue (RGB). The red, green and blue laser sources correspond to a He–Ne laser at a wavelength of 633 nm and diode lasers operating at wavelengths of 532 nm and 405 nm, respectively. A polarizing beam splitter is used to obtain a horizontally polarized input beam. Then, horizontal, vertical, diagonal and anti-diagonal components of the intensity profile are measured using a sequence of a half-wave plate and a polarizing beam splitter. Figure 4 shows the desired 'cross' patterns previously described. The intensity profiles for left and right circularly polarized input beams are also shown in figure 4, where the intensity forms a *uniform* doughnut shape. As a measure of the quality of coupling between SAM and OAM in our device, polarization conversion efficiency (the amount of light converting from one polarization handedness to the opposite one in circular polarization basis) is measured. Conversion efficiencies of 96%, 95% and 94% for red, green and blue light are obtained, respectively. These conversion efficiencies are quite high and indicative of the high quality of the OAM generator.

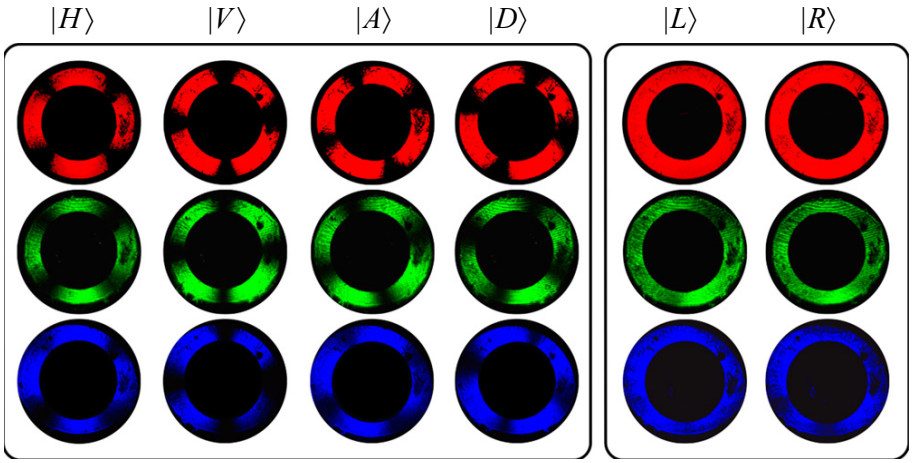

Figure 4. (left) Recorded intensity profiles of the outgoing beam from the device after projecting its polarization state onto horizontal (H), vertical (V), diagonal (D), and anti-diagonal (A) directions. The device is illuminated with a linearly horizontal polarized beam. (right) Beam intensity profiles when the cone is fed with a left (L) and right (R) circularly polarized light beam. The rows correspond to different laser sources with wavelengths of 633 nm, 532 nm and 405 nm, respectively. In all cases, the dark disk in the center of the pattern is the *dead zone* described in the text. In the above figure, the residual light from the central region has been artificially masked for reasons of clarity.

4.2. OAM state tomography

Polarization projective measurements shown in the previous section give a nice illustration of the spin-to-orbital angular momentum coupling nature of the device. In this section, we show quantitative measurements confirming the generation of OAM values of $2\hbar$ per photon for a left-handed circularly polarized beam, and $-2\hbar$ per photon for a right-handed circularly polarized beam. In order to reconstruct the OAM state of the output beam we performed OAM state tomography. We measured the OAM spectrum of the output beam by performing a phase-flattening projective measurement technique [29]. The measured OAM power spectrum is negligible for $|\ell| \neq 2$. The results confirm that the emerging beam from the device carries OAM values of $\ell = \pm 2$. Thus, we limit our analysis to a bi-dimensional OAM Hilbert space spanned by the following basis: $\{|\ell = +2\rangle_o, |\ell = -2\rangle_o\}$, where $|\ell\rangle_o$ represents an OAM state in this Hilbert space. Hence the OAM state of the output beam can be represented by $|\psi\rangle_o = \alpha|+2\rangle_o + \beta|-2\rangle_o$, where α and β are complex numbers. This specific OAM sub-space is isomorphous to the polarization Hilbert space spanned by two orthogonal polarization states, which can be represented by the SU(2) group [30]. Pauli Matrices $\hat{\sigma}_x$, $\hat{\sigma}_y$, $\hat{\sigma}_z$, and the identity matrix $\hat{I}$ are corresponding generators of the SU(2) group. Therefore, one can reconstruct the OAM density matrix of the output light beam, i.e. $\rho_{|\psi\rangle_o} := |\psi\rangle_o\langle\psi|_o$, by projecting the unknown OAM state $|\psi\rangle_o$ over the eigenstates of the generators. This is identical to measuring the polarization Stokes parameters, i.e. projecting the state on the H, V, A, D, L and R basis. The correspondence with the case of polarization is straightforwardly done by associating $|+2\rangle_o$ and $|-2\rangle_o$ to the left and right-handed circular polarized states of light, respectively. A full characterization of the unknown OAM state can be done by measuring four

independent *Stokes-like* parameters Λ_i ($i = 0, 1, 2, 3$) defined as:

$$\begin{cases} \Lambda_0 = P_{|+2\rangle_o} + P_{|-2\rangle_o} \\ \Lambda_1 = P_{|h\rangle_o} - P_{|v\rangle_o} \\ \Lambda_2 = P_{|a\rangle_o} - P_{|d\rangle_o} \\ \Lambda_3 = P_{|+2\rangle_o} - P_{|-2\rangle_o}. \end{cases} \tag{5}$$

Where $P_{|i\rangle_o}$ are the power of the projective measurement over the state of $|i\rangle_o$, and $|h\rangle_o = \left(|+2\rangle_o + |-2\rangle_o\right)/\sqrt{2}$, $|v\rangle_o = -i\left(|+2\rangle_o - |-2\rangle_o\right)/\sqrt{2}$, $|a\rangle_o = \left(|+2\rangle_o + i|-2\rangle_o\right)/\sqrt{2}$, and $|d\rangle_o = \left(|+2\rangle_o - i|-2\rangle_o\right)/\sqrt{2}$ are the eigenstates of the $\hat{\sigma}_x$ and $\hat{\sigma}_y$, respectively [31]. In order to achieve these sets of measurements, we implement a well-known phase-flattening projective measurement. In this technique, the emerging beam from the device is imaged onto a spatial light modulator (SLM) where different computer-generated holograms corresponding to the above six measurements were displayed. These holograms 'flatten' the corresponding *complementary phase-front* of the beam at the first order of diffraction. Thus, only the 'flattened' component of the optical field can be coupled into a single mode optical fibre, which results in measuring $P_{|i\rangle_o}$ [32, 33]. The SLM and the single mode optical fibre act as the polarizer in the case of polarization state tomography. We implement this approach using a Pluto HOLOEYE SLM suitable for visible, excluding ultra-violet, wavelengths. The power of the projective measurements $P_{|i\rangle_o}$ are recovered by a Newport power meter. From these measurements the Stokes-like parameters of equation (5) are calculated. The reconstructed OAM density matrix of the output beam is then calculated by the following expression:

$$\hat{\rho} = \frac{1}{2}\sum_{i=0}^{3}\frac{\Lambda_i}{\Lambda_0}\hat{\sigma}_i. \tag{6}$$

Figure 5 shows the reconstructed OAM density matrix for different input polarization states, and a red and green laser source. Fidelity of 94% and 91% are observed for generating the OAM value of +2 and −2 with a red laser source, and 93% and 98% are observed for generating OAM value of +2 and −2 with a green laser source. It is worth mentioning that we do not have access to a UV-SLM since all commercial liquid-crystal devices will not work as desired for the case of blue/UV light. This is based on the fact that they are originally made using UV light, and consequently, illuminating them with a UV light source would change the orientation of the polymer substrate. However, the analysis reported in the previous section confirmed the existence of spin-to-orbital angular momentum coupling for the blue laser as well. Thus, our device can be used to generate OAM values of ± 2 at the UV wavelength regime, which is a missing fact in the community.

4.3. White vector vortex beam

We examine the broadband performance of the device by performing a polarization projective measurement for the case of a linearly polarized white-light input beam. A liquid crystal display (laptop screen) is used as the polarized white light source and a high definition camera was used to detect the transverse intensity profile of the output beam after projecting the light polarization state by means of a broadband half-wave plate and a polarizing beam splitter. The 'cross'

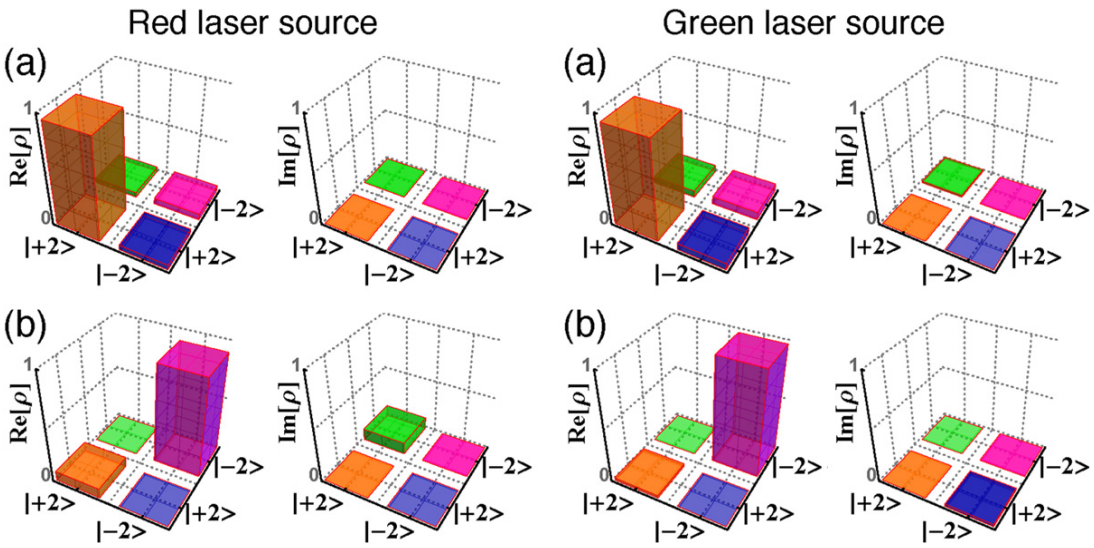

Figure 5. Experimental OAM density matrix of the emerging beam from the device reconstructed from OAM state tomography. (a) and (b) are corresponding to left and right-handed input circular polarizations, respectively. We observe fidelity of 94% and 91% for generating OAM of +2 and −2 with a red laser source, and of 93% and 98% for generating OAM of +2 and −2 with a green laser source.

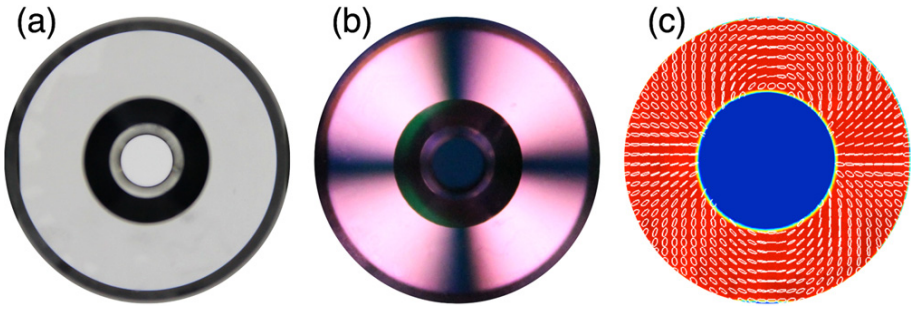

Figure 6. (a) Intensity profile of the outgoing beam from our device when illuminated with a white polarized light source. (b) Intensity distribution of the white light beam when the the device is sandwiched between two crossed polarizers. (c) Polarization distribution of the outgoing beam when illuminated by a white polarized light source. This beam possesses a polarization topology of two which means that the orientation of the polarization in the transverse plane undergoes a full rotation as we go through a full cycle around the beam's axis.

pattern was also observed for the white light source; rotating the half-wave plate leads to a rotation of the cross through the same angle.

Figure 6(a) shows the transverse intensity distribution of the outgoing beam from the device when illuminated with a white polarized source. As can be seen, the transmitted beam has a uniform intensity distribution. The petal pattern is also visible when the device is sandwiched between two crossed polarizers; see figure 6(b). Polychromatic effects around the null intensity lines are observed, which lies at the heart of diffraction. When the device is

illuminated with a polychromatic (white) wave, different colours undergo different diffraction effects since they have different wavelengths [34, 35]. As we have already discussed, the device transfers a linearly polarized beam into a vector vortex beam. We reconstructed the polarization pattern of the generated vector beam by performing polarization state tomography, where the reduced Stokes parameters of the output beam are measured via polarization projective measurements; see [28] for more details. The reconstructed topology of the generated beam is shown in figure 6(c). As can be seen, the transverse polarization pattern corresponds to the expected 'dipole' shape shown previously in the theory section.

5. Conclusions

In conclusion, we have proposed and demonstrated an efficient and novel way to convert the spin of incoming light into OAM via spin-to-orbital angular momentum coupling in an *isotropic* media. The idea lies at the heart of the space-variying cylindrically symmetric dielectric slab formed by two hollow axicons under a specific total internal reflection condition, which works as an inhomogeneous half-wave plate. Since the relative phase change is almost wavelength independent, the device works as an achromatic OAM generator in the OAM subspace of $|\ell| = 2$ for visible and infrared regime. Moreover, the device introduces a specific polarization topology into the incoming beam, since it possesses a space-variant polarization dependent phase shift. Thus, as we have shown, it can be used to generate a white light vector vortex beam. This specific OAM generator can also be widely used in imaging techniques such as an optical vortex coronagraph, where achromatic OAM generators of $|\ell| = 2$ is needed [18].

The authors would like to thank an anonymous reviewer for bringing to our attention the related work published in references [36] and [37]. However, we note that this earlier work deals with the generation of achromatic, radially polarized light beams, whereas our work deals with the development of a device capable of generating beams with an OAM of $|\ell| = 2$. The novelty of our work is therefore not compromised by this other work.

Acknowledgments

The authors thank Joe Vornehm, Mark Martucci and Doug Hand for insightful discussions regarding the cone fabrication. The authors also acknowledge the support of the Canada Excellence Research Chairs (CERC) program.

References

[1] Franke-Arnold S, Allen L and Padgett M J 2008 *Laser Photon. Rev.* **2** 299
[2] Hell S W 2007 *Science* **316** 1153
[3] Paterson L, MacDonald M P, Arlt J, Sibbett W, Bryant P E and Dholakia K 2001 *Science* **292** 912
[4] He H, Heckenberg N R and Rubinsztein-Dunlop H 1995 *J. Mod. Opt.* **42** 217
[5] Molina-Terriza G, Torres J P and Torner L 2007 *Nat. Phys.* **3** 305
[6] Gibson G, Courtial J, Padgett M J, Vasnetsov M, Pasko V, Barnett S M and Franke-Arnold S 2004 *Opt. Express* **12** 5448
[7] Boyd R W, Jha A, Malik M, O'Sullivan C, Rodenburg B and Gauthier D J 2011 *Proc. SPIE* **7948** 79480L–1
[8] Vallone G, D'Ambrosio V, Sponselli A, Slussarenko S, Marrucci L, Sciarrino F and Villoresi P 2014 *Phys. Rev. Lett.* **113** 060503

[9] Mirhosseini M, Magaa-Loaiza O S, O'Sullivan M N, Rodenburg B, Malik M, Lavery M P J, Padgett M J, Gauthier D J and Boyd R W 2014 (arXiv:1402.7113)
[10] Barreiro J T, Wei T C and Kwiat P G 2008 *Nat. Phys.* **4** 282
[11] Beijersbergen M W, Coerwinkel R P C, Kristensen M and Woerdman J P 1994 *Opt. Commun.* **112** 321
[12] Yu Bazhenov V, Soskin M S and Vasnetsov M V 1992 *J. Mod. Opt.* **39** 985
[13] Mirhosseini M, Magana-Loaiza O S, Chen C, Rodenburg B, Malik M and Boyd R W 2013 *Opt. Express* **21** 30196
[14] Allen L, Beijersbergen M W, Spreeuw R and Woerdman J P 1992 *Phys. Rev.* A **45** 8185
[15] Marrucci L, Manzo C and Paparo D 2006 *Phys. Rev. Lett.* **96** 163905
[16] Berry M V, Jeffrey M R and Mansuripur M 2005 *J. Opt. A: Pure Appl. Opt.* **7** 685
[17] Mansuripur M, Zakharian A R and Wright E M 2011 *Phys. Rev.* A **84** 033813
[18] Foo G, Palacios D M and Swartzlander G A 2005 *Opt. Lett.* **30** 3308
[19] Zhang X and Qui L 2013 *Opt. Eng.* **52** 048001
[20] Born M and Wolf E 1999 *Principles of Optics* (Cambridge: Cambridge University Press)
[21] Bhandari R 1997 *Phys. Rep.* **281** 1
[22] Bomzon Z, Biener G, Kleiner V and Hasman E 2002 *Opt Lett.* **27** 1141
[23] Marrucci L, Karimi E, Slussarenko S, Piccirillo B, Santamato E, Nagali E and Sciarrino F 2011 *J. Opt.* **13** 064001
[24] Karimi E, Schulz S A, de Leon I, Qassim V, Upham J and Boyd R W 2014 *Light: Science & Applications* **3** e167
[25] Cardano F, Karimi E, Marrucci L, de Lisio C and Santamato E 2013 *Opt. Express* **21** 8815
[26] Beckley A M, Brown T G and Alonso M A 2010 *Opt. Express* **18** 10777
[27] Karimi E, Zito G, Piccirillo B, Marrucci L and Santamato E 2007 *Opt. Lett.* **32** 3053
[28] Cardano F, Karimi E, Slussarenko S, Marrucci L, de Lisio C and Santamato E 2012 *Appl. Opt.* **51** C1
[29] Mair A, Vaziri A, Weihs G and Zeilinger A 2001 *Nature* **412** 313
[30] Padgett M J and Courtial J 1999 *Opt. Let.* **24** 430
[31] Nagali E, Sciarrino F, de Martini F, Karimi E, Piccirillo B, Marrucci L and Santamato E 2009 *Opt. Express* **17** 18745
[32] Qassim H, Miatto F M, Torres J P, Padgett M J, Karimi E and Boyd R W 2014 *J. Opt. Soc. Am.* B **31** A20
[33] Roux F S and Zhang Y 2014 *Phys. Rev.* A **90** 033835
[34] Gbur G, Visser T D and Wolf E 2001 *Phys. Rev. Lett.* **88** 013901
[35] Tavassoly M T, Amiri M, Karimi E and Khalesifard H R 2005 *Opt. Commun.* **255** 23
[36] Wakayama T, Komaki K, Otani Y and Yoshizawa T 2012 *Opt. Express* **20** 29260
[37] Wakayama T, Rodríguez-Herrera O G, Tyo J S, Otani Y, Yonemura M and Yoshizawa T 2014 *Opt. Express* **22** 3306

Chapter 3

Dynamics of twisted light in laser-induced birefringence

This chapter is based on the following paper:

1. A. Ahangary, **F. Bouchard**, E. Santamato, E. Karimi, and H. R. Khalesifard, "Dynamics of laser-induced radial birefringence in silver-doped glasses," *Optics Letters*, vol. 40, p. 4062 (2015).

3.1 Birefringence due to induced radial stress

In this chapter, we study the underlying mechanism of laser induced birefringence by considering the elastic properties of the material [10]. The result of such induced radial stress in silver-doped glasses is similar to that of a q-plate where the optical axis of the birefringent material varies in its transverse plane. Ultimately, this leads to spin-to-orbit coupling and the generation of twisted light as described in the previous chapter. In the following section, we are mostly interested in the physics underlying this effect.

3.1.1 Displacement vector and strain tensor

We initiate this study by considering the effect of deformation on a solid body. Initially, a point in the object can be characterized by a vector $\mathbf{r}$ with components x, y and z, in Cartesian coordinates. After the deformation, this point may be at a

position given by $\mathbf{r}'$, with components x', y' and z'. The displacement of this point due to the deformation is given in terms of the *displacement vector*, $\mathbf{u} = \mathbf{r}' - \mathbf{r}$. When considering two points very close to each other with a distance between them of $\mathrm{d}l = \sqrt{\mathrm{d}x^2 + \mathrm{d}y^2 + \mathrm{d}z^2}$, it is interesting to ask what is the distance between these two points after the deformation, i.e. $\mathrm{d}l' = \sqrt{\mathrm{d}x'^2 + \mathrm{d}y'^2 + \mathrm{d}z'^2}$. Using Einstein's summation convention, $\mathrm{d}l'$ may be expressed in terms of the displacement vector, $\mathrm{d}l'^2 = (\mathrm{d}x_i + \mathrm{d}u_i)^2$, where $\mathrm{d}u_i = (\partial u_i/\partial x_j)\mathrm{d}x_j$. This can be further rewritten as $\mathrm{d}l'^2 = \mathrm{d}l^2 + 2u_{ij}\mathrm{d}x_i\mathrm{d}x_j$, where u_{ij} is called the strain tensor and is given by,

$$u_{ij} = \frac{1}{2}\left(\frac{\partial u_i}{\partial x_j} + \frac{\partial u_j}{\partial x_i} + \frac{\partial u_l}{\partial x_i}\frac{\partial u_l}{\partial x_j}\right). \tag{3.1}$$

For small deformations, the last term may be neglected, i.e. $\mathbf{u}_{ik} = (\partial u_i/\partial x_j + \partial u_j/\partial x_i)/2$. The displacement vector may be obtained by solving the equation of equilibrium in the case of isotropic bodies,

$$\frac{3\,(1-\sigma)}{1+\sigma}\nabla\left(\nabla\cdot\mathbf{u}\right) + \frac{3\,(1-2\sigma)}{2\,(1+\sigma)}\nabla\times\left(\nabla\times\mathbf{u}\right) = \alpha\nabla T, \tag{3.2}$$

where σ, α and T are Poisson's ratio, the thermal expansion coefficient and the temperature, respectively. In the case of a purely radial deformation, one obtains the following differential equation,

$$\frac{\mathrm{d}}{\mathrm{d}r}\left(\frac{1}{r}\frac{\mathrm{d}\,(ru_r)}{\mathrm{d}r}\right) = \alpha\frac{1+\sigma}{3\,(1-\sigma)}\frac{\mathrm{d}T}{\mathrm{d}r}. \tag{3.3}$$

The solution to this equation is given by the following integral ,

$$u_r = \alpha\frac{1+\sigma}{3\,(1-\sigma)}\left[\frac{1}{r}\int_0^r T(\rho)\rho\mathrm{d}\rho + (1-2\sigma)\,\frac{r}{R^2}\int_0^R T(\rho)\rho\mathrm{d}\rho\right], \tag{3.4}$$

where R is taken as the radial position of the boundary, with the following boundary condition, $T(R) = 0$.

3.1.2 Driven heat equation

We must find an expression for the radial temperature profile, $T(r)$, in order to get an explicit solution for the displacement vector u. This may be done by solving the heat equation given by,

$$\alpha \nabla^2 T = \frac{\partial T}{\partial t} - \frac{\alpha}{k} \kappa I, \tag{3.5}$$

where, α is the thermal diffusivity, k is the thermal conductivity, κ is the absorption coefficient and I is the intensity of the incident optical beam. This differential equation can be solved for the temperature in two limiting cases, i.e. in its steady-state form, $\alpha \nabla^2 T = -\alpha \kappa I/k$ and in its transient-state form, $\alpha \nabla^2 T = \partial T/\partial t$. The temperature profile obtained in both situations can be introduced in Eq. (3.4) in order to obtain an analytical expression for the steady-state and transient-state solution of the radial component of the displacement vector.

3.1.3 Dielectric tensor

From the displacement vector obtained above, one may now compute the strain tensor. The only non-vanishing components of the strain tensor are given by, $u_{rr} = \partial u_r/\partial r$ and $u_{\varphi\varphi} = u_r/r$, and can be linked to the optical properties of the material via the dielectric tensor,

$$\epsilon_{ij} = \epsilon_0 \delta_{i,j} + a_1 u_{ij} + a_2 u_{kk} \delta_{ij}, \tag{3.6}$$

where a_1 and a_2 are scalar constants. From this dielectric tensor, one may then calculate the birefringence of the medium, where in our case we have, $\Delta n = n_{rr} - n_{\varphi\varphi} = \sqrt{\epsilon_{rr}} - \sqrt{\epsilon_{\varphi\varphi}}$. In the assumption that the quantity $\Delta\epsilon = \epsilon_{rr} - \epsilon_{\varphi\varphi}$ is small enough, the birefringence can be approximated as, $\Delta n \approx \Delta\epsilon/(2\sqrt{\epsilon_{rr}})$. Finally, the *local* optical retardation, $\delta = 2\pi \Delta n \; d/\lambda$, is given in terms of the birefringence and results in a birefringent medium with a transversely dependent optical axis of unity topological charge. Ultimately, this will lead to the generation of twisted light carrying an orbital angular momentum value of 2.

Optics Letters

Dynamics of laser-induced radial birefringence in silver-doped glasses

Ali Akbar Ahangary,[1] Frédéric Bouchard,[2] Enrico Santamato,[3] Ebrahim Karimi,[2,*] and Hamid Reza Khalesifard[1]

[1]Department of Physics, Institute for Advanced Studies in Basic Sciences, 45137-66731 Zanjan, Iran
[2]Department of Physics, University of Ottawa, 25 Templeton St., Ottawa, Ontario, K1N 6N5, Canada
[3]Department of Physics, University of Naples "Federico II," Complesso Universitario di Monte S. Angelo, 80126 Napoli, Italy
*Corresponding author: ekarimi@uottawa.ca

Received 22 July 2015; revised 6 August 2015; accepted 6 August 2015; posted 7 August 2015 (Doc. ID 246463); published 26 August 2015

Silver ion-exchanged glass exhibits nonlinear optical properties upon interacting with intense light beams. The thermal effect due to the nanoparticles' light-absorption induces radial stress, and consequently, a radial birefringence on the glass surface. The induced birefringence possesses a topological charge of 1 in the transverse plane of the glass, i.e., cylindrical symmetry. Therefore, when the glass is illuminated with a circularly polarized light beam, a portion of the incoming beam flips its polarization handedness, since the plate is birefringent, and gains an orbital angular momentum of ±2 in units of the Planck constant. This is referred to as optical spin-to-orbital angular momentum conversion, and can be understood by means of the Pancharatnam–Berry phase. Here, we design a pump–probe setup to study and observe the dynamics of optical angular momentum coupling in real time. We show that this effect can be permanent or reversible, depending on the power and interaction time of the pump beam. In particular, an intrinsic power-dependent birefringence hysteresis is observed on the sample after interaction with and the relaxation of the irradiated point. © 2015 Optical Society of America

OCIS codes: (260.6042) Singular optics; (260.1440) Birefringence; (350.1370) Berry's phase.

http://dx.doi.org/10.1364/OL.40.004062

Metal-doped dielectrics are of particular interest due to their peculiar linear and nonlinear optical properties, as well as their applications in medical science. The novel optical properties of metal-doped dielectrics arise from the fact that dielectrics and metals have bound and free electrons, respectively. Therefore, they behave differently upon interacting with electromagnetic waves, and show *unique* optical properties mainly on the surface where surface-plasmon polartions are excited. The optical properties of these waves, such as frequency, phase, and polarization, strictly depend on the size, structure, and distribution of the metal nanoparticles [1]. Engineering the nanoparticles' structure in a specific shape and topology as well as a desired distribution (cluster form) may lead to the invention of novel miniaturized photonic devices [2–4]. Different approaches have been proposed to manufacture these metal-doped dielectrics, such as induced diffusion, applying a strong DC electric field, and induced radiation pressure upon interacting with high-power laser sources, among others [5–7]. Among the different types of metal-doped dielectrics, silver ion-exchanged glass is particularly interesting due to its cost-effective fabrication as well as its impactful applications. For instance, silver nanoparticles embedded in a glass matrix are used to generate antibacterial scalpels [8]. Apart from the above-mentioned optical features, functioning silver ion devices may be affected upon interacting with an intensely bright light beam. The absorption of silver nanoparticles at the optical domain induces a third-order nonlinear thermal effect. It has been shown that this thermal effect introduces a "local" heat on the glass surface where the silver ions penetrated [9]. Such a local heat deforms the glass matrix, especially on the surface; thus, it results in two major optical effects: (i) *a local phase modulation*, and (ii) *a transverse birefringence due to induced radial stress*. These two are shown to exhibit a lensing and an optical spin-to-orbital angular momentum conversion, respectively [9,10]. The latter case arises from the fact that the radial stress introduces a radial birefringence. Therefore, the object is birefringent, but holds its cylindrical symmetry. Upon interacting with a light beam, the total optical angular momentum $\mathcal{J}_z$ and the spin angular momentum $\mathcal{S}_z$ + orbital angular momentum $\mathcal{O}_z$ (OAM) are preserved, i.e., $\mathcal{J}_z^{\text{in}} = \mathcal{J}_z^{\text{out}}$, where "in" and "out" stand for the input and output beams, respectively. In addition to these effects, the size and the distribution of the silver nanoparticles are affected by the illumination [11]. The radial birefringence effect described in the case of silver nanoparticles is similar to the case of liquid crystal droplets, where the liquid crystal molecules orient themselves in a radial manner. When circularly polarized light is made to go through the liquid crystal droplets, the output light will carry OAM, due to the spin-to-orbit coupling mentioned above [12]. However, in the nonlinear regime, the optical angular momentum conversion efficiency is significantly altered by the driving pump beam [13].

0146-9592/15/174062-04$15/0$15.00 © 2015 Optical Society of America

In this Letter, we examine the dynamics of this third-order nonlinear thermal effect in real time. Indeed, a pump–probe experiment is implemented to reveal the dynamics of laser-induced radial birefringence, which results in optical spin-to-OAM coupling. We experimentally show that when a silver-doped glass is illuminated with an intense laser beam, the induced birefringence as well as the self-phase modulation appear immediately. These effects are exceedingly pronounced by increasing the interaction time as well as the pump intensity. When the pump beam is turned off, the thermal effect vanishes, nonetheless leaving the sample with permanent radial stress (birefringence). We show that this effect does not only depend on the present magnitude of the laser power, but also on the "previous history" of the sample, which results in a significant birefringence hysteresis.

The silver ion-exchanged samples are prepared by immersing glass slides (of dimensions 24 mm × 40 mm × 0.9 mm) into a molten salt of $AgNO_3/NaNO_3$ (4/96 wt. %) at 400°C for 4 h. Throughout this process, the Ag^+ ions are exchanged with alkali ions due to diffusion, where the Ag^+ ions penetrate up to 100 μm into the surface of the glass [14]. After the ion exchange process, the glass is left to cool for 2 h and washed with HNO_3, H_2SO_4, and 3-distilled water to remove the residue from the salts and chemicals from the glass surface. The prepared samples' compositions are obtained by x ray fluorescence analysis, which reveals the following compositions; SiO_2:73.72, CaO: 6.98, Na_2O:12.90, MgO: 4.08, Al_2O_3:0.353, K_2O:0.10, Cl: 0.135, Fe_2O_3:0.07, and SO_3:1.653. The obtained ion-exchanged glass slides are pumped by a focused Ar^+ laser beam at different powers. This is a standard approach to induce silver penetration into a glass matrix, where the radiation pressure, due to the pump, induces a longitudinal force onto the silver nanoparticles. Prior to the irradiance, the glass is isotropic. Upon interacting with the Ar^+ laser beam, however, the silver nanoparticles absorb a portion of the pump beam. The induced heat on the ion-exchanged glass is identical to the beam shape, i.e., Gaussian, and therefore is nonuniform on the glass surface. The corresponding heat equation is in its steady-state form, $\alpha\nabla^2 T = -\kappa P$, where α and κ are, respectively, the thermal diffusivity and absorption coefficient of the silver-doped glass, and P is the power of the pump laser. The heat distribution forms a bell-like shape in this case. Therefore, the laser beam induces a cylindrical symmetry thermal gradient toward the beam center, which causes a radial strain tensor $\mathbf{u}_{i,j} = (\partial u_i/\partial x_j + \partial u_j/\partial x_i)/2$ that is given in terms of the following displacement vector, $u = u_i\hat{\mathbf{e}}_i$:

$$\frac{3(1-\sigma)}{1+\sigma}\nabla(\nabla\cdot u) + \frac{3(1-2\sigma)}{2(1+\sigma)}\nabla\times(\nabla\times u) = -\alpha\nabla T, \quad (1)$$

where σ is Poisson's ratio [15], and x_i's and $\hat{\mathbf{e}}_i$'s are, respectively, cylindrical coordinates r, φ, z with their corresponding unit vectors $\hat{\mathbf{r}}, \hat{\varphi}$, and $\hat{\mathbf{z}}$.

This radial stress alters the glass matrix strain tensor, and induces (via elasto-optic coefficients) a *steady-state* (st) "local" birefringence $\delta_{st}(r)$, represented in the cylindrical coordinate

$$\delta_{st}(r) = \delta_0^{st}\left(1 + \frac{1}{2}\left(\frac{w_0}{r}\right)^2\left(e^{-2\left(\frac{r}{w_0}\right)^2} - 1\right)\right), \quad (2)$$

where δ_0^{st} is the asymptotic birefringence at the sample's periphery that depends on the pump intensity and optical properties of the sample, and w_0 is the pump beam radius on the glass surface [9,16]. When the pump beam is turned off, the heat equation describing the thermal distribution on the sample is expressed in its *transient-state* form, as $\alpha\nabla^2 T = \partial T/\partial t$. In the transient state, the driving *heat* source is absent, and the temperature decreases and tends to stabilize with time. For this specific case, the induced "local" birefringence in the cylindrical coordinates is time dependent and is given by

$$\delta_{tr}(r;t) = \delta_0^{tr}\int_0^\infty \beta \mathrm{d}\beta A(\beta) e^{-\alpha\beta^2 t} J_2(\beta r), \quad (3)$$

where $A(\beta) = \int T(r;t_0)J_0(\beta r)r\mathrm{d}r$, $T(r;t_0)$ is the initial temperature distribution *function* at a given time of t_0, and $J_0(\cdot)$ and $J_2(\cdot)$ are Bessel functions of the first kind. For both cases of the steady and transient states, the birefringence possesses a topological charge of 1 in the glass transverse plane, i.e., it holds a cylindrical symmetry. In other words, the optical axis of the locally induced birefringence χ is identical to the azimuthal angle φ in the polar coordinates, i.e., $\chi(\varphi) = \varphi$. The action of the irradiated silver-doped glass on the linear polarization in the laboratory frame can be expressed by means of the Jones matrix formalism, as follows:

$$\begin{aligned}\hat{\mathcal{M}} &= \mathcal{R}(\varphi)\cdot\begin{bmatrix} e^{-i\delta/2} & 0 \\ 0 & e^{i\delta/2}\end{bmatrix}\cdot\mathcal{R}(-\varphi) \\ &= \cos\left(\frac{\delta}{2}\right)\begin{bmatrix}1 & 0\\ 0 & 1\end{bmatrix} - i\sin\left(\frac{\delta}{2}\right)\begin{bmatrix}\cos(2\varphi) & \sin(2\varphi)\\ \sin(2\varphi) & -\cos(2\varphi)\end{bmatrix},\end{aligned} \quad (4)$$

where $\mathcal{R}(\chi)$ is the standard active rotation matrix in the x–y transverse plane. We used the basis of horizontal and vertical linear polarizations. $\hat{\mathcal{M}}$ is a function of time (for the case of the transient state) and varies in the transverse plane, i.e., $\hat{\mathcal{M}} := \hat{\mathcal{M}}(r,\varphi;t)$. When a circularly polarized light beam traverses the glass plate, a portion $\cos^2(\delta/2)$ passes through the plate without being altered, corresponding to the first term in Eq. (4). However, the remaining fraction $\sin^2(\delta/2)$, associated with the second term in Eq. (4), undergoes spin-to-OAM coupling, since its polarization handedness changes signs, and the converted beam gains a helical phase of $\exp(\pm 2i\varphi)$, where the sign depends on the input beam's polarization state. This effect can also be explained in terms of the Pancharatnam–Berry phase, where the adiabatic evolution of a polarization state upon propagation through the sample results in different trajectories on the polarized Poincaré sphere [17–19].

In order to monitor the optical properties of the sample when it interacts with the pump beam in real time, we implement a pump–probe setup where an He–Ne laser is used as a probe beam. A schematic of the experimental setup is shown in Fig. 1. Due to the cylindrical symmetry of the sample and of the pump beam, the probe beam is brought to the circular polarization basis. The weak probe beam is then integrated into a polarizing Mach–Zehnder-like interferometer, where the beam is made to illuminate the sample in one of the arms while it is kept as a reference beam in the other arm. The phase front of the probe beam is monitored at one of the output ports of the interferometer by recording the spatial distribution of the interference pattern onto a CCD camera. The depolarization conversion efficiency [second term of Eq. (4)] due to the optical spin-to-OAM coupling is measured by means of an appropriate arrangement of a quarter-wave plate, a polarizer, and a silicon

photodiode detector. The power of the depolarized probe beam, the $\sin^2(\delta(t)/2)$ portion, is recorded before, during, and after the interaction of the sample with the pump Ar^+ laser beam. The Ar^+ laser beam operates at the continuous-wave multimode regime, where "blue" (457.9, 476.5, 488.0, and 496.5 nm) wavelength emission lines are present. These wavelengths, although they have lower power, are near the resonance peak, which is located at 430 nm, of the surface-plasmon waves of the sample [14]. The irradiations were carried out at a fixed beam diameter of 63 μm, with the pump power ranging from 2.5 to 4.5 W, where each interaction point on the surface has a corresponding pump power. Only regions with identical optical densities were chosen for the experiment. In order to study the behavior of the samples during interaction with the Ar^+ laser beam, the samples were irradiated for different exposure times corresponding to the sub-second range of $\{0.1, 0.2, 0.4, 0.6, 0.8\}$ and $\{1, 2, 4, 8, 16, 32, 64, 128, 256, 512\}$ seconds. The duration of each interaction is controlled by means of a time-controllable chopper. The interference patterns were recorded in real time at the same time that the sample was being pumped with the Ar^+ laser beam. Figures 1(a) and 1(b) show the recorded interference patterns when the pump laser beam is turned *on* and *off*. The double-helix interference shown in the upper inset of Fig. 1 reveals that the beam emerging from the glass sample possesses a dislocation with a topological charge of 2 around the beam's center. This "spiralling" effect is observed to be permanent, as shown in Fig. 1. However,

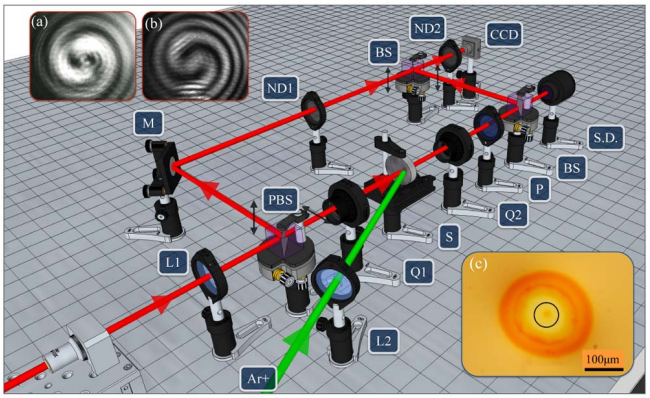

Fig. 1. Illustration of the pump–probe experiment. The sample *S* is illuminated by a focused Ar^+ laser *pump* beam (green arrow). A *probe* He–Ne laser (red arrow) is introduced to a polarizing Mach–Zehnder-like interferometer to measure the *depolarization* as well as the wavefront alteration of the probe during and after the interaction of the sample with the pump. Insets (a) and (b), respectively, show the interference patterns of the probe beam with a reference spherical wave during and after the illumination of the sample by the pump. The double helix indicates the presence of a phase singularity with a topological charge of 2 that is induced by the sample. The interaction point of the sample (transmittance image) is shown in inset (c), where the sample is exposed for 1 s with a 4.5 W pump beam. The black circle shows the spot size on the sample, which is 63 μm in diameter. A video of the probe's wavefront alteration (see Visualization 1) is recorded upon the interaction of the sample with a 4 W pump beam for a duration of 120 s. Legends: Q1/Q2: quarter-wave plate, *S*: sample, *P*: polarizer, BS: beam splitter, M: mirror, ND1: neutral density filter [optical density (OD) = 3], ND2: neutral density filter (OD = 0.5), L1: lens (f = 400 mm), L2: lens (f = 122 mm), S. D.: silicon photodiode detector, Ar^+:Ar^+ laser beam.

a small astigmatism is observed, which is attributed to the slight tilt between the pump and the probe beams. As the probe beam polarization state is changed from left- to right-handed circular polarization, the direction of the helix patterns are "reversed." The depolarization, or equivalently, the spin-to-OAM conversion efficiency, is next thoroughly studied for a number of different pump powers and interaction times. By doing so, one may observe the induced birefringence process for different scenarios, such as the steady state and the transient state. Figure 2(a) shows the depolarized component of the pump beam traversing the glass sample as the interaction between the pump and the sample is alternately turned on and off, for various interaction times. The spin-to-OAM coupling is observed to be larger during the interaction of the pump with the sample, rapidly reaching the steady-state condition. Nevertheless, as the pumping is suppressed, the glass sample enters the transient-state regime, where the depolarization magnitude drops significantly to a non-negligible level, which is found to be permanent. After the interaction, the residual depolarization increases for a longer pumping duration time, indicating the presence of hysteresis in the system. More precisely, there are explicit hysteresis effects whenever the sample is pumped in a circular-like path of pumping powers. This effect is shown in Fig. 3 for powers ranging from 0.0 to 3.5 W,

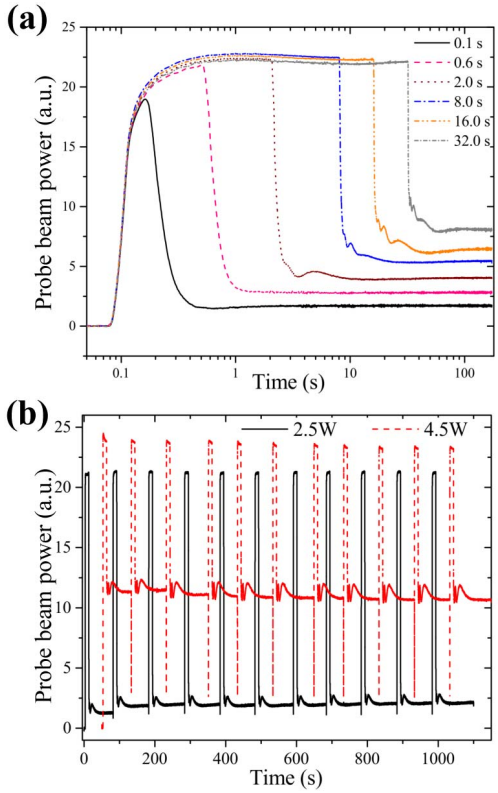

Fig. 2. Measured power of probe beam due to the induced depolarization through interaction points for (a) different integration times when the pump power is set to 3.5 W, and (b) pumping single points at 2.5 and 4.5 W for 10 s durations in 11 iterations. A single point is irradiated for 10 s, followed by a 40 s period of relaxation. In both cases, the induced birefringence significantly increased by interaction time; thus the energy induced by the pump beam increased. This becomes permanent after turning off the pump beam. Nonetheless, the induced birefringence reaches a saturation point after several iterations.

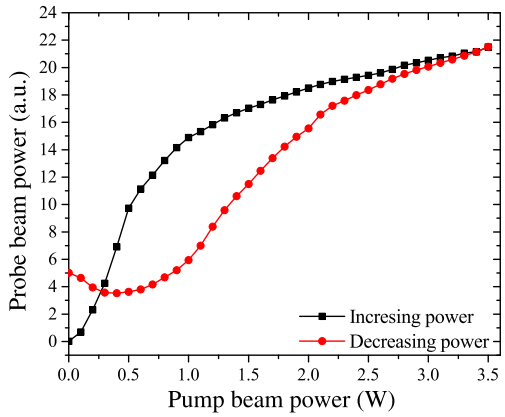

Fig. 3. Observed birefringence hysteresis on the silver-doped glass measured upon interacting with the Ar^+ pump laser. The power is increased (decreased) with an increment step of 0.1 W, and the irradiation time for each measurement point is chosen to be 10 s. After a full cycle, the glass is subject to a permanent induced birefringence.

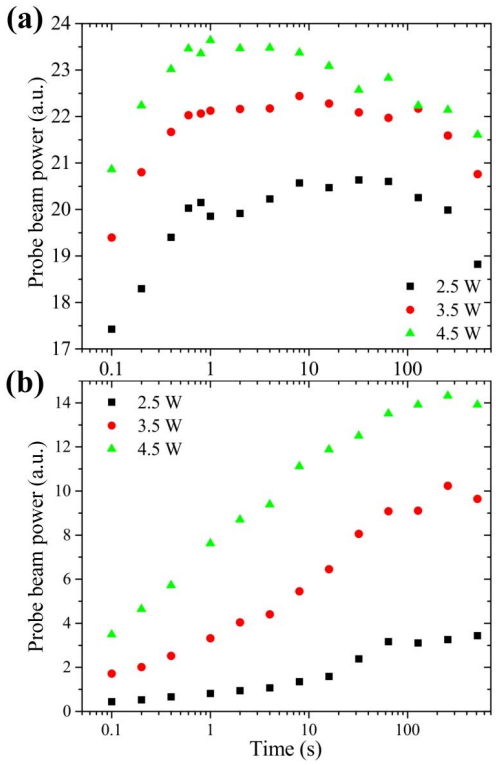

Fig. 4. Power of transmitted probe beam detected (a) during pumping and (b) after relaxation of the interaction points.

with increments/decrements of 0.1 W and pumping duration times of 10 s for all increments, thus allowing the system to reach the steady state. Further, we investigated whether the induced birefringence and hysteresis effect described above are purely a consequence of nonlinear thermal effects. This is done by irradiating the glass samples 11 times at two distinct pumping powers, 2.5 and 4.5 W, for a duration of 10 s. In order to ensure the thermal relaxation of the sample after pumping, time intervals of 190 s are assumed between two successive irradiations. As can be seen from the monitored depolarization in Fig. 2(b), the induced birefringence of the sample remains quantitatively unchanged throughout the irradiation intervals, thus indicating no energy accumulation effects, which still suggests the validity of our thermal nonlinearities-based model. There are two kinds of saturation for the interaction points, during pumping and after relaxation, which are shown in Figs. 4(a) and 4(b), respectively. Maximum spin-to-OAM coupling happens for 8, 8, and 4 s of irradiation with a pump power of 2.5, 3.5 and 4.5 W, respectively. In contrast, there is maximum conversion efficiency for ∼100 seconds of irradiation when the samples are relaxed.

In conclusion, we presented a pump–probe setup to examine the depolarization conversion efficiency due to spin-to-orbit coupling, and we recorded the phase pattern of the depolarized probe beam in real time. In particular, we observed a strong birefringence hysteresis due to the laser-induced radial stress. Our findings are in good agreement with theoretical model based on thermally induced radial birefringence in the silver-doped glass sample. The model describes the laser-induced spin-to-OAM conversion for both the cases of the steady and transient states.

Funding. Canada Excellence Research Chairs, Government of Canada (Canada Excellence Research Chairs Program)

Acknowledgment. F. B. and E. K. acknowledge the support of the Canada Excellence Research Chairs Program.

REFERENCES

1. U. Kreibig and M. Vollmer, *Optical properties of metal clusters* (Springer, 1995).
2. A. Abdolvand, A. Podlipensky, S. Matthias, F. Syrowatka, U. Gösele, G. Seifert, and H. Graener, Adv. Mater. **17**, 2983 (2005).
3. E. Karimi, S. A. Schulz, I. De Leon, H. Qassim, J. Upham, and R. W. Boyd, Light Sci. Appl. **3**, e167 (2014).
4. F. Bouchard, I. De Leon, S. A. Schulz, J. Upham, E. Karimi, and R. W. Boyd, Appl. Phys. Lett. **105**, 101905 (2014).
5. A. Podlipensky, A. Abdolvand, G. Seifert, H. Graener, O. Deparis, and P. Kazansky, J. Phys. Chem. B **108**, 17699 (2004).
6. F. Stietz, Appl. Phys. A **72**, 381 (2001).
7. R. Jin, Y. C. Cao, E. Hao, G. S. Métraux, G. C. Schatz, and C. A. Mirkin, Nature **425**, 487 (2003).
8. L. Esteban-Tejeda, F. Malpartida, A. Esteban-Cubillo, C. Pecharromán, and J. Moya, Nanotechnol. **20**, 085103 (2009).
9. J. M. Amjad, H. R. Khalesifard, S. Slussarenko, E. Karimi, L. Marrucci, and E. Santamato, Appl. Phys. Lett. **99**, 011113 (2011).
10. Y. Kaganovskii, I. Antonov, F. Bass, M. Rosenbluh, and A. Lipovskii, J. Appl. Phys. **89**, 8273 (2001).
11. A. Nahal, J. Mostafavi-Amjad, A. Ghods, M. Khajehpour, S. Reihani, and M. Kolahchi, J. Appl. Phys. **100**, 053503 (2006).
12. E. Brasselet, N. Murazawa, H. Misawa, and S. Juodkazis, Phys. Rev. Lett. **103**, 103903 (2009).
13. M. El Ketara and E. Brasselet, Opt. Lett. **37**, 602 (2012).
14. M. Niry, J. Mostafavi-Amjad, H. Khalesifard, A. Ahangary, and Y. Azizian-Kalandaragh, J. Appl. Phys. **111**, 033111 (2012).
15. L. D. Landau and E. M. Lifshitz, *Theory of Elasticity (Volume 7 of A Course of Theoretical Physics)* (Pergamon, 1970).
16. S. Mosca, B. Canuel, E. Karimi, B. Piccirillo, L. Marrucci, R. De Rosa, E. Genin, L. Milano, and E. Santamato, Phys. Rev. A **82**, 043806 (2010).
17. L. Marrucci, E. Karimi, S. Slussarenko, B. Piccirillo, E. Santamato, E. Nagali, and F. Sciarrino, J. Opt. **13**, 064001 (2011).
18. S. Pancharatnam, *Proceedings of the Indian Academy of Sciences, Section A* (Indian Academy of Sciences, 1956), vol. **44**, p. 247.
19. M. V. Berry, J. Mod. Opt. **34**, 1401 (1987).

Chapter 4

Generation of twisted light using plasmonic metasurfaces

This chapter is based on the following paper:

1. **F. Bouchard**, I. De Leon, S. A. Schulz, J. Upham, E. Karimi, and R. W. Boyd, "Optical spin-to-orbital angular momentum conversion in ultra-thin metasurfaces with arbitrary topological charges," *Applied Physics Letters*, vol. 105, p. 101905 (2014).

4.1 Geometric phases with plasmonic metasurfaces

In this chapter, we present a novel device that uses geometrical phases to generate twisted light. The underlying physics involved for such generation is identical to that described in the two previous chapters. The main difference here is the nature of the birefringence in the material as well as the orbital angular momentum values carried by the generated beams. In chapter 2, the birefringence emerges from the polarisation dependent phase obtained from total internal reflection. In order to obtain a perfect twisted light generator, an optical retardation of $\delta = \pi$ is required. In the case of total internal reflection, the optical retardation was controlled by carefully tuning the refractive index and the incident angle of the medium. In chapter 3, this optical retardation varied radially, giving rise to several rings carrying orbital angular momentum. In this chapter, the optical retardation is a result of a phase difference between two plasmonic resonances in the case of orthogonal linear polarisations.

This is done by considering an L-shaped nano-antenna, where an anti-diagonally and a diagonally polarized beam respectively excite an *antisymmetric* and a *symmetric* mode causing the birefringence of the nano-antennas. The relative phase between these two modes for an array of such nano-antennas may be engineered in order to obtain a $\delta = \pi$ optical retardation by adjusting the size and the periodicity of the nano-antennas. The relative orientation of the L-shaped nano-antennas corresponds to the optical axis of the birefringent media. Hence, by transversally varying the orientation of the nano-antennas, we were able to generate twisted light with orbital angular momentum values of up to 25.

4.2 High-dimensional quantum information

In many quantum information schemes, the use of high-dimensional quantum states, also known as *qudits*, has proven to be more advantageous than its 2-dimensional counterpart, also known as *qubits*. In quantum communications, high-dimensional photonic states may be used to send many bits of information on single photons rather than many photons carrying a single bit of information [11]. In fundamental tests of quantum mechanics, exploring the quantum nature of physics in high-dimensional systems is extremely interesting and such experiments may be performed using high-dimensional states of light [12]. Finally, in quantum cryptography, e.g. quantum key distribution, the security of many protocols increases with the dimensionality of the quantum states used [13]. Provided that, in the future, quantum technologies will have to be brought down to a much smaller scale using integrated photonic devices, nanoscale high-dimensional photonic state generators could represent a key component to the implementation of these technologies or protocols. By fabricating and characterizing nanoscale twisted light generators with orbital angular momentum values of up to 25, we show the viability of such devices for applications in many high-dimensional quantum information schemes, where qudits of dimensionality up to 51 could be achieved.

Optical spin-to-orbital angular momentum conversion in ultra-thin metasurfaces with arbitrary topological charges

Frédéric Bouchard,[1] Israel De Leon,[1] Sebastian A. Schulz,[1] Jeremy Upham,[1] Ebrahim Karimi,[1,a)] and Robert W. Boyd[1,2]
[1]*Department of Physics, University of Ottawa, 25 Templeton, Ottawa, Ontario K1N 6N5 Canada*
[2]*Institute of Optics, University of Rochester, Rochester, New York 14627, USA*

(Received 21 July 2014; accepted 1 September 2014; published online 11 September 2014)

Orbital angular momentum associated with the helical phase-front of optical beams provides an unbounded "space" for both classical and quantum communications. Among the different approaches to generate and manipulate orbital angular momentum states of light, coupling between spin and orbital angular momentum allows a faster manipulation of orbital angular momentum states because it depends on manipulating the polarisation state of light, which is simpler and generally faster than manipulating conventional orbital angular momentum generators. In this work, we design and fabricate an ultra-thin spin-to-orbital angular momentum converter, based on plasmonic nano-antennas and operating in the visible wavelength range that is capable of converting spin to an arbitrary value of orbital angular momentum ℓ. The nano-antennas are arranged in an array with a well-defined geometry in the transverse plane of the beam, possessing a specific integer or half-integer topological charge q. When a circularly polarised light beam traverses this metasurface, the output beam polarisation switches handedness and the orbital angular momentum changes in value by $\ell = \pm 2q\hbar$ per photon. We experimentally demonstrate ℓ values ranging from ± 1 to ± 25 with conversion efficiencies of $8.6\% \pm 0.4\%$. Our ultra-thin devices are integratable and thus suitable for applications in quantum communications, quantum computations, and nanoscale sensing. © *2014 AIP Publishing LLC*. [http://dx.doi.org/10.1063/1.4895620]

In addition to linear momentum and energy, light beams also possess angular momentum.[1] It has been shown that in vacuum the optical angular momentum can be decomposed into two nominally independent terms; spin angular momentum (SAM) and orbital angular momentum (OAM).[2,3] SAM is intrinsic and related to the vectorial nature of light. A circularly polarised beam carries SAM: $+\hbar$ per photon for a left-circularly polarised beam and $-\hbar$ per photon for a right-circularly polarised beam, where $\hbar$ stands for the reduced Planck constant.[4] By comparison, OAM has both intrinsic and extrinsic terms, the latter of which is coordinate dependent.[5] The intrinsic OAM, hereafter simply referred to as OAM, is related to the azimuthal dependence of the optical phase. Thus, a beam with a helical wavefront that has a phase dependence of $\exp(i\ell\varphi)$ carries OAM of $\ell\hbar$ per photon, where ℓ can take any positive or negative integer value.[6] Although, SAM and OAM are two "rotational" degrees of freedom of light that are nearly independent, they can interact under specific conditions such as tight focusing of a circularly polarised light beam,[7] light-matter interaction in space-variant dielectric,[8] inhomogeneous birefringent,[9] or structured media.[10,11] We recently demonstrated a metasurface composed of an inhomogenous array of plasmonic nano-antennas with a thickness much smaller than the operating wavelength. This metasurface can be wielded to transform a circularly polarised light beam into a beam carrying OAM. The dimension of the individual nano-antenna and the periodicity of the array were chosen such that the array exhibits approximately a half-wavelength, i.e., π, optical retardation between two plasmonic resonances.[11] In the previous study, the plasmonic nano-antenna arrangement was cylindrically symmetric, meaning that in one cycle around the origin of the metasurface the individual nano-antennas exhibit a single rotation, which corresponds to a unit topological charge q (see $q = 1$ in Fig. 1(a)). The device's operation principle was based on the *full* spin-to-orbital angular momentum conversion. Because the metasurface was rotationally symmetric, there was *no* exchange of angular momentum between the photons and the metasurface and this device yielded light carrying OAM of $\ell = \pm 2q\hbar = \pm 2\hbar$. However, this symmetry is not a requirement for spin to OAM conversion and a more general geometry of metasurfaces with different q values could access a much broader range of OAM values.

In this work, we design and fabricate ultra-thin plasmonic metasurfaces with a general geometry possessing integer or half-integer topological charges. The working principle of these devices is based on the coupling between optical spin and OAM, an effect that occurs in inhomogeneous wave-plates.[12] Indeed, the device flips the SAM of the input beam and the output beam gains a nonuniform, helical phase-front, depending on the orientation of the nano-antenna array. Our fabricated metasurfaces are capable of generating OAM values in the domain of $\{-25,\ldots, +25\}$ with a conversion efficiency of about 9% at visible wavelengths 760 nm–790 nm. However, the metasurface has a theoretical conversion efficiency as high as 44%, with reduction in efficiency originating from discrepancies between the ideal and fabricated nano-antenna dimensions. Such an efficiency would be suitable for performing recently

a)ekarimi@uottawa.ca

 © 2014 AIP Publishing LLC

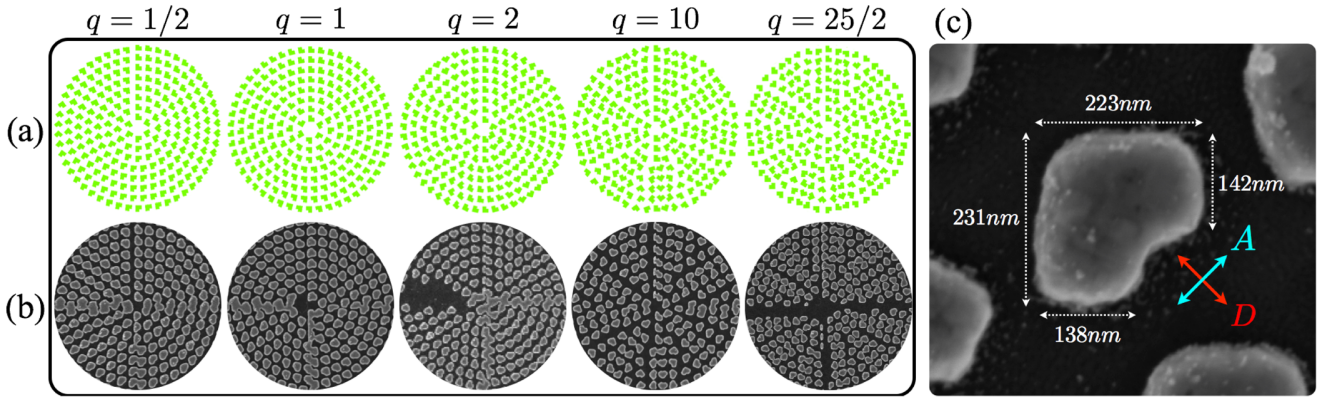

FIG. 1. (a) Spatial arrangement of nano-antennas in the plane of the metasurfaces for generating light beams carrying OAM values of {±1, ±2, ±3, ±20, and ±25}. (b) SEM images of the fabricated metasurfaces corresponding to the designs shown in (a). q indicates the topological charge. (c) SEM image of a single L-shaped nano-antenna with a measured dimension shown in magenta colour. Diagonal (D) and anti-diagonal (A) polarisation states excite a symmetric and an anti-symmetric mode, respectively.

demonstrated quantum computations with photon's SAM and OAM.[13,14]

To generate OAM through spin-to-orbital angular momentum coupling, we require a metasurface composed of birefringent elements that exhibit a half-wavelength optical retardation between two orthogonal polarisation states. In our design, such birefringent elements take the form of L-shaped gold nano-antennas with equal arm-lengths, as illustrated in Fig. 1(c). A nano-antenna with this geometry supports two surface plasmon resonances, associated with polarisations aligned parallel and perpendicular to the symmetry axis of the nano-antenna. Diagonal (D) and anti-diagonal (A) polarisation states, respectively, excite a symmetric and an anti-symmetric mode (see Fig. 1(c))—analogous to the case of coupled harmonic oscillators. The optical retardation δ between these two optical modes can be adjusted to approximate π by choosing the appropriate dimensions and periodicity of the nano-antennas, although these vary for different operating wavelengths.[15] The action of this metasurface, neglecting both absorption and reflection, in the Jones calculus (omitting a global phase delay) is given by

$$\sigma_z = \begin{pmatrix} 1 & 0 \\ 0 & -1 \end{pmatrix}, \tag{1}$$

where $\exp(i\pi) = -1$ represents the relative optical retardation of π between excited diagonal and anti-diagonal polarisation states. As can be seen, Eq. (1) represents the action of a half-wave plate in the A-D polarization basis. Let us now consider an array of such antennas that are rotated by an angle α about an axis orthogonal to the plate's surface. A straightforward Jones calculation determines the metasurface action as $R(-\alpha)\ \sigma_z\ R(\alpha)$, which in the *circular polarisation* basis is given by

$$\mathcal{M}_\alpha = \begin{pmatrix} 0 & e^{-2i\alpha} \\ e^{2i\alpha} & 0 \end{pmatrix}, \tag{2}$$

where we assume $|L\rangle = \begin{pmatrix} 1 \\ 0 \end{pmatrix}$ and $|R\rangle = \begin{pmatrix} 0 \\ 1 \end{pmatrix}$ to be left-circular and right-circular polarisation states, respectively. Again a global phase ($\pi/2$) is omitted. As expected, in the circular polarisation basis, this proposed metasurface flips the polarisation state of an input beam from left (L) to right (R) circular polarisation or *vice versa*, i.e., $\mathcal{M}_\alpha \cdot |L\rangle = \exp(2i\alpha)\,|R\rangle$. However, any rotation of the metasurface orientation does not change the output polarisation state $|R\rangle$, and the output polarisation state remains right circularly polarised (or left depending on the input handedness). Nevertheless, the rotated metasurface introduces a *uniform* phase $\exp(\pm 2i\alpha)$, which depends both on the input polarisation state and the orientation of the metasurface. This introduced phase, known as the Pancharatnam-Berry phase, is equal to half of the solid angle probed by the state evolution on the polarisation Poincaré sphere.[16,17] The sign of this phase is defined by the helicity of the input polarisation, positive for left-handed and negative for right-handed input polarised beams, corresponding to a clockwise or a counter-clockwise path on the Poincaré sphere. However, in general, the orientation of the nano-antennas can be nonuniform, i.e., it can vary within the transverse plane. Here, we consider the specific case where the orientation of the nano-antennas is dependent on the azimuthal angle of the polar coordinate system and the topological charge, i.e., $\alpha(\varphi) = q\,\varphi$. In fact, the topological charge q determines the amount of rotation of the nano-antennas for a full coordinate rotation ($\varphi \rightarrow \varphi + 2\pi$). Different metasurfaces with topological charges of $q = 1/2$, 1, 3/2, 10, and 25/2 are shown in Figs. 1(a) and 1(b). Apart from a small region very close to the origin, where the nano-antenna orientation is *undefined* (a singularity), the metasurface introduces a nonuniform, helical staircase-like phase-front of $\exp(\pm i\,2q\,\varphi)$ to the circularly polarised output beam. Thus, the emerging beam possesses an OAM value of $\pm 2q$, with the sign depending on the input polarisation state. This imposes a condition on the value of q. Since a physical beam carries an integer OAM value, q must be an integer or half-integer. However, in practice the metasurface may not introduce a *perfect* phase delay of π; thus, its action on a circularly polarised basis is more complicated than discussed above. For such a plate, the action can be split into two parts; a portion of the beam that undergoes spin-to-orbital angular momentum conversion and gains an OAM value of $\pm 2q$ and another portion that is not affected by the metasurface, remaining in the same

polarisation and OAM states as the input beam. These two portions have orthogonal circular polarisation states, and thus they can be separated by means of a quarter-wave plate (QWP) followed by a polarising beam splitter (PBS).

The gold metasurface was fabricated on a fused silica substrate through electron beam lithography in a positive bi-layer resist, followed by thermal metal evaporation and lift-off. Charge dissipation during the lithography step was achieved through a conductive layer consisting of 23 nm thick indium tin oxide (ITO). Typical dimensions for an individual nano-antenna are 142–150 nm arm width, 235–242 nm arm length, and a thickness of 90–96 nm with a periodicity of 330 nm. This design provides an optical retardation of 1.35π radian between two linearly orthogonal polarisation states and a conversion efficiency of about 35% at a wavelength of 780 nm. Here, we define the conversion efficiency as the ratio of the converted power to the total power of the transmitted beam, i.e., the sum of both the converted and the non-converted components transmitted out of the sample. Scanning electron microscope (SEM) images of several metasurface plates having different topological charges are shown in Fig. 1(b). As can be seen in Fig. 1(c), the shape of nano-antenna does not form a perfect L-shape. Because the individual antennas are not perfectly L-shaped, their birefringence between the resonances of the *A* and *D* polarizations is relaxed somewhat, which affects the metasurface's conversion efficiency but does not compromise the working principle of the device. Similarly, the small number of nano-antennas missing from the device surface affects only the intensity profile of the emerging beam.

The experimental setup shown in Fig. 2 is used to record both the intensity and the wavefront of the beams generated by the metasurfaces. Measurements are carried out using a tunable diode laser, working in the wavelength range of 760 nm–790 nm. The single-mode laser beam is spatially cleaned through coupling into a single mode optical fibre. The beam is circularly polarised by means of a PBS followed by a rotated QWP. The reflected beam from the PBS, which is vertically polarised, is used as a reference beam in the Mach-Zehnder interferometer, to record the wavefront of the generated beam. In order to record the interference pattern, the polarisation of the reference beam is rotated to horizontal polarisation by means of a half-wave plate. On the sample arm, a convex lens with a focal length of 200 mm is used to reduce the beam size to be comparable with the diameter of the *patterned* metasurface ($\simeq 100\,\mu$m). A $10\times$ microscope objective is used to collimate the transmitted beam. The transmitted beam contains both the converted and non-converted parts, with orthogonal circular polarisations, e.g., for a left handed circularly polarised input beam the converted and non-converted beams have right- and left-circular polarisations, respectively. A sequence of a rotated QWP at an angle of $\pi/4$ and a PBS is used to separate the converted and non-converted light, for simultaneous power measurements. The intensity profile of the converted beam, which possesses OAM, is then captured by a (DCU223C) Charge-Coupled Device (CCD) camera. Figure 3(a) shows the intensity profile of the converted beams generated by the plasmonic metasurfaces shown in Fig. 1(b). As can be seen, the emerging beams possess a doughnut shape with a *null* intensity at the origin. This null intensity, which is caused by the phase singularity at the beam centre, is characteristic for beams with a helical phase front. The plasmonic plate introduces such a helical phase-front of $\exp(\pm i\,2q\,\varphi)$ into the Gaussian input beam. At the metasurface exit face, this beam is proportional to $\exp(-r^2/w_0^2)\,\exp(\pm i\,2q\,\varphi)$, where r is the radial distance in polar coordinates and w_0 is the beam waist of the input Gaussian beam. This is a subfamily of Hypergeometric-Gaussian beams that reduce to a superposition of two Bessel-Gaussian beams[18,19] and is not shape-invariant under free-space propagation, as explained in Ref. 18. The OAM value of the emerging beam is determined by recording the interference pattern with a reference beam. The interference of a spherical reference wave and a beam carrying OAM value of ℓ results in a helical pattern with ℓ intertwined lobes. Switching the input polarisation state from left-circular to right-circular polarisation does not change the intensity profile, but changes the sign of the OAM value ℓ. Thus, it reverses the twisting direction of the intertwined helices of the interference pattern, without affecting the number of helices. Figures 3(b) and 3(c) show interference patterns of the converted beams from the plasmonic metasurfaces (shown in Fig. 1(b)) for both left-circular and right-circular input polarisation states. These confirm that the output beams possess OAM values equal to

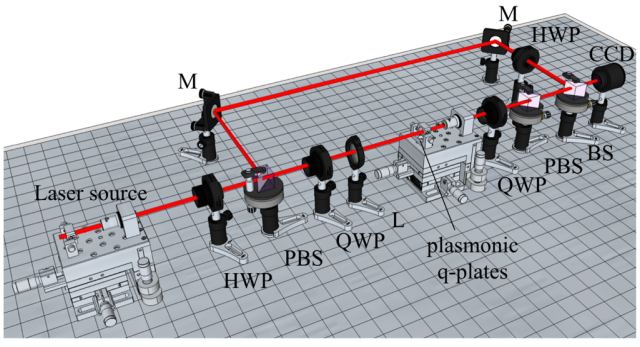

FIG. 2. Experimental setup. M: mirror, L: lens, HWP: half-wave plate, QWP: quarter-wave plate, BS: beam splitter, PBS: polarising beam splitter, and CCD: Charge-Coupled Device camera.

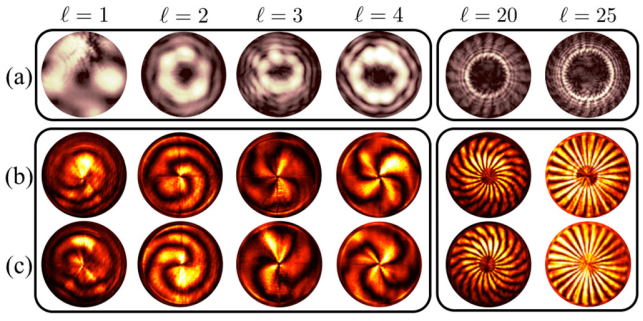

FIG. 3. Intensity profile and recorded interference patterns of the beam generated by the plasmonic metasurfaces for different OAM values. (a) The intensity profile of the converted component of the transmitted light. The central null field at the origin results from the phase singularity. (b) and (c) The interference pattern of the generated beams with a spherical wave. The (b) and (c) rows correspond to left and right-circularly polarised input beams. The number of intertwined helices reveals that the transmitted beams possess OAM of $\ell = \pm 1, \pm 2, \pm 3, \pm 4, \pm 20$, and ± 25.

twice the metasurface topological charge, i.e., $|\ell| = 2q$ as expected from our previous discussion.

Finally, the conversion efficiency of the device is measured for the wavelength range from 760 nm to 790 nm. In our definition, both reflections and absorptions by different optical components, including the metasurface, are not considered. This distinguishes the *purity* of the generated beam from absorption and reflections off optical components in the experimental setup, as this *purity* is generally the limiting factor. Conversion efficiencies of $(8.6 \pm 0.4)\%$ at a wavelength of 780 nm are measured for different metasurface plates. This conversion efficiency is reasonably spectrally broad, for example, the $q = 2$ metasurface showed a change of only 0.4% across the 30 nm wavelength range.

In summary, we designed and fabricated plasmonic metasurfaces with arbitrary integer and half-integer topological charges capable of generating beams of light carrying integer magnitudes of OAM. The largest OAM value tested was 25, but there is no fundamental upper bound on the ℓ magnitudes that could be achieved by these plasmonic metasurfaces. We experimentally investigated spin to OAM conversion at various ℓ values by recording the intensity and phase profiles of the beams generated by these metasurfaces. About 9% of the transmitted light was converted. This technology would introduce ultra-thin OAM generators into integrated devices, which could have applications for nano-scale sensing,[20] classical,[21,22] and quantum communications.[23,24]

The authors thank Hammam Qassim for fruitful discussions, and acknowledge the support of the Canada Excellence Research Chairs (CERC) Program.

[1]L. Allen, S. M. Barnett, and M. J. Padgett, *Optical Angular Momentum* (Taylor and Francis Group, 2003).
[2]C. Darwin, Proc. R. Soc. London, Ser. A **136**, 36 (1932).
[3]J. Humblet, Physica **10**, 585 (1943).
[4]R. A. Beth, Phys. Rev. **50**, 115 (1936).
[5]A. O'Neil, I. MacVicar, L. Allen, and M. Padgett, Phys. Rev. Lett. **88**, 053601 (2002).
[6]L. Allen, M. W. Beijersbergen, R. Spreeuw, and J. Woerdman, Phys. Rev. A **45**, 8185 (1992).
[7]Y. Zhao, J. S. Edgar, G. D. Jeffries, D. McGloin, and D. T. Chiu, Phys. Rev. Lett. **99**, 073901 (2007).
[8]Z. Bomzon, G. Biener, V. Kleiner, and E. Hasman, Opt. Lett. **27**, 1141 (2002).
[9]L. Marrucci, C. Manzo, and D. Paparo, Phys. Rev. Lett. **96**, 163905 (2006).
[10]G. Li, M. Kang, S. Chen, S. Zhang, E. Y.-B. Pun, K. W. Cheah, and J. Li, Nano Lett. **13**, 4148 (2013).
[11]E. Karimi, S. A. Schulz, I. De Leon, H. Qassim, J. Upham, and R. W. Boyd, Light: Sci. Appl. **3**, e167 (2014).
[12]L. Marrucci, E. Karimi, S. Slussarenko, B. Piccirillo, E. Santamato, E. Nagali, and F. Sciarrino, J. Opt. **13**, 064001 (2011).
[13]V. D'Ambrosio, N. Spagnolo, L. Del Re, S. Slussarenko, Y. Li, L. C. Kwek, L. Marrucci, S. P. Walborn, L. Aolita, and F. Sciarrino, Nat. Commun. **4**, 2432 (2013).
[14]F. Cardano, F. Massa, E. Karimi, S. Slussarenko, D. Paparo, C. de Lisio, F. Sciarrino, E. Santamato, and L. Marrucci, preprint arXiv:1403.4857 (2014).
[15]F. Aieta, P. Genevet, M. A. Kats, N. Yu, R. Blanchard, Z. Gaburro, and F. Capasso, Nano Lett. **12**, 4932 (2012).
[16]S. Pancharatnam, in *Proceedings of the Indian Academy of Sciences, Section A* (Indian Academy of Sciences, 1956), Vol. 44, pp. 247–262.
[17]M. V. Berry, J. Mod. Opt. **34**, 1401 (1987).
[18]E. Karimi, G. Zito, B. Piccirillo, L. Marrucci, and E. Santamato, Opt. Lett. **32**, 3053 (2007).
[19]Z. Sacks, D. Rozas, and G. Swartzlander, Jr., J. Opt. Soc. Am. B **15**, 2226 (1998).
[20]S. W. Hell, Science **316**, 1153 (2007).
[21]G. Gibson, J. Courtial, M. J. Padgett, M. Vasnetsov, V. Pas'ko, S. M. Barnett, and S. Franke-Arnold, Opt. Express **12**, 5448 (2004).
[22]N. Bozinovic, Y. Yue, Y. Ren, M. Tur, P. Kristensen, H. Huang, A. E. Willner, and S. Ramachandran, Science **340**, 1545 (2013).
[23]G. Vallone, V. D'Ambrosio, A. Sponselli, S. Slussarenko, L. Marrucci, F. Sciarrino, and P. Villoresi, Phys. Rev. Lett. **113**, 060503 (2014).
[24]M. Mirhosseini, O. S. Magaña-Loaiza, M. N. O'Sullivan, B. Rodenburg, M. Malik, D. J. Gauthier, and R. W. Boyd, preprint arXiv:1402.7113 (2014).

Chapter 5

Observation of subluminal twisted light in vacuum

This chapter is based on the following paper:

1. **F. Bouchard**, J. Harris, H. Mand, R. W. Boyd, and E. Karimi, "Observation of sub-luminal twisted light in vacuum," *Optica*, vol. 3, p. 351 (2016).

5.1 Group velocities of twisted light

The orbital angular momentum of light is directly related to the structure of its wavefront. Interestingly, the phase and group velocity of light intrinsically depends on its wavefront. We are then interested in the study of the effect of twisting the wavefront of a short pulse of light on its group velocity in free-space. Obviously, the group velocity of any pulse of light in vacuum will be in the vicinity of the physical constant c, representing the speed of light in vacuum, but we are interested in extremely small shifts in the group velocities due to the effect of wavefront twisting. Let us first review the concept of group velocity.

Considering a set of co-propagating plane waves with different frequencies, ω, one may adjust their relative phases in order to obtain a sequence of constructive and destructive interferences resulting in a localized pulse of light in time and space. Traditionally, the expression for the group velocity is given by $v_g = \partial\omega/\partial k$, where k is the wavevector and is given by $k = \omega/c$ in vacuum. The group velocity of an optical pulse in vacuum is always given by $v_g = c$, hence the name of the constant c.

However, here we assumed that pulses consisted of a superposition of *plane waves* that has a trivial phase profile. In order to describe the group velocity of a propagating pulse of light that has a structured wavefront, one needs a more general expression for the group velocity of light in vacuum. This expression is derived in Appendix A and is given by $v_{\mathrm{g}} = |\partial_\omega \nabla \Phi|^{-1}$, where Φ is the phase of the optical field. For the sake of convenience, we will now adopt the LG basis as our orbital angular momentum carrying optical fields for our group velocity calculations. The phase of an LG mode labelled by indices ℓ and p is given by,

$$\Phi_{\ell,p}^{(\mathrm{LG})}(\mathbf{r},\omega) = \frac{\omega}{c} z + \frac{\omega r^2}{2cR} + \ell\phi - (2p + |\ell| + 1)\,\zeta, \tag{5.1}$$

where R is the radius of curvature of the beam's wavefront and ζ is the Gouy phase. Hence, one would then expect different group velocities $v_{\mathrm{g}}^{(\ell,p)}$ associated with different LG modes.

5.2 Intensity Autocorrelation

In order to measure extremely small temporal variations from pulses carrying different orbital angular momentum values ℓ, a very accurate method to measure timing of short pulses is required. Generally, measuring very short time events requires an even shorter time event. However, short pulses of light are usually the shortest events we have access to in the laboratory. Hence, the best we can do experimentally is to use a short pulse to measure itself. The problem with this technique is that pulses of light usually do not interact when crossing each other's path. Fortunately, this does not hold true in the case of nonlinear optics [14]. In general, two beams of light interacting in a nonlinear medium may give rise to a wide variety of optical phenomena. One of the most basic occurences of such optical nonlinearity is second harmonic generation (SHG). SHG usually occurs when two photons overlapping in a nonlinear medium both in time and space interact in such a way to produce a new photon at a different colour. Conservation of energy dictates the change of colours where the frequency of the up-converted photon will be equal to the sum of the frequencies of the pump photons. Hence, by looking at the frequency of the light exiting the nonlinear medium, one may determine whether the pulses are overlapping or not. This information is sufficient to obtain timing information of the pulse.

Intensity autocorrelation [15] is the process in which a short pulse of light is split

into two pulses, for example with a beam splitter. The two pulses are subsequently recombined and made to overlap inside a nonlinear medium. A delay line is introduced in the path of one of the pulses in order to adjust the arrival time of that pulse. When the two pulses are made to arrive simultaneously at the crystal, their overlap is maximal, thus resulting in the largest amount of SHG. The SHG signal may be filtered from the incoming beams by adopting a non-collinear scheme where the SHG signal will exit the nonlinear medium at a different angle than the incoming beams. This is due to conservation of linear momentum in a parametric process. When the arrival time of one of the photons is varied, the SHG signal will start to decrease, hence letting us approximately reconstruct the temporal profile of the input pulse. In general, this technique will give us a rough estimate of the temporal profile of the pulse and thus a more sophisticated method may be employed to do so. In our experiment, we are not particularly interested in the shape of the pulse, but rather in the small shift of the point of maximal SHG resulting from a non-constant group velocity for various ℓ indices.

optica

Observation of subluminal twisted light in vacuum

Frédéric Bouchard,[1,2] Jérémie Harris,[1,2] Harjaspreet Mand,[1,2] Robert W. Boyd,[1,2,3] and Ebrahim Karimi[1,2,*]

[1]Department of Physics, University of Ottawa, 25 Templeton St., Ottawa, Ontario K1N 6N5, Canada
[2]The Max Planck Centre for Extreme and Quantum Photonics, University of Ottawa, Ottawa, Ontario K1N 6N5, Canada
[3]Institute of Optics, University of Rochester, Rochester, New York 14627, USA
*Corresponding author: ekarimi@uottawa.ca

Received 9 December 2015; revised 27 January 2016; accepted 2 February 2016 (Doc. ID 255400); published 23 March 2016

Einstein's theory of relativity establishes the speed of light in vacuum, *c*, as a fundamental constant. However, the speed of light pulses can be altered significantly in dispersive materials. While significant control can be exerted over the speed of light in such media, to our knowledge no experimental demonstration of altered light speeds has hitherto been achieved in vacuum for "twisted" optical beams. We show that "twisted" light pulses exhibit subluminal velocities in vacuum, being 0.1% slowed relative to *c*. This work does not challenge relativity theory but experimentally supports a body of theoretical work on the counterintuitive vacuum group velocities of twisted pulses. These results are particularly important given recent interest in applications of twisted light to quantum information, communication, and quantum key distribution. © 2016 Optical Society of America

OCIS codes: (260.0260) Physical optics; (080.4865) Optical vortices; (070.7345) Wave propagation.

http://dx.doi.org/10.1364/OPTICA.3.000351

Velocity, the rate at which an object changes its position over time, is well-defined for Newtonian particles, but cannot in general be unambiguously assigned to waves. For the specific and unphysical case of a monochromatic plane wave, however, a propagation rate, referred to as the phase velocity, can be attributed to the beam phase front. The phase velocity v_{ph} of a monochromatic plane wave in a medium with refractive index n is given by c/n. A more general expression for v_{ph} is required when considering the propagation of a light beam with phase front $\Phi(\mathbf{r})$, $v_{\mathrm{ph}} = \omega/|\nabla\Phi|$, where ω denotes the angular frequency of the beam and ∇ represents the gradient with respect to the spatial coordinate $\mathbf{r}$ [1]. A pulsed beam, which is spatiotemporally localized, is comprised of an infinite superposition of monochromatic waves, each of which propagates at a distinct phase velocity $v_{\mathrm{ph}}(\omega)$. It is the constructive and destructive interference among these frequency components that gives rise to the pulse shape and position. As a result, the pulse propagates at a speed different from that of the individual monochromatic waves of which it is composed. The speed at which the pulse envelope propagates is referred to as the group velocity v_g and is given by $v_g = |\partial_\omega \nabla\Phi|^{-1}$, where ∂_ω stands for differentiation with respect to ω [1]; see Supplement 1 for more details.

The refractive index of a nondispersive medium does not depend on the frequency of light being considered. Consequently, the phase and group velocities associated with a plane wave propagating along a nondispersive medium's z axis will take on the values $v_{\mathrm{ph}} = v_g = c/n$, since $\Phi = (\omega n/c)z$. In contrast to plane waves, the phase and group velocities of light pulses can differ by orders of magnitude in dispersive media such as cold atomic clouds [2], atomic vapors [3,4], and structurally engineered materials [5–7]. Under such exotic conditions, pulse group velocities can be rendered greater or smaller than c, or even negative [8]. Here we investigate the exotic group velocities exhibited by Laguerre–Gauss (LG) modes in vacuum. In particular, we observe and explain subluminal effects that arise due to the twisted nature of the optical phase front. We use an experimental setup that employs nonlinear intensity autocorrelation to measure relative time delays between Gaussian and twisted beams, and show these time delays to be significant, in some cases reaching several tens of femtoseconds. Our theoretical treatment predicts that further exotic effects, such as superluminal propagation in vacuum, might also manifest themselves as a consequence of the structured light beams.

Despite their mathematical simplicity, plane waves carry infinite energy and therefore are unphysical. More complex waves that can only be approximated even under ideal experimental conditions, such as Bessel beams and evanescent waves, have been studied for their exotic group velocities in vacuum [9,10]. A recent publication has also reported slow-light effects in vacuum [11] for both Gaussian and Bessel-like beams. The work demonstrated light delays as large as ~27 fs. The observed effect here and that of Giovannini *et al.* [11] are comparable in magnitude, although different in nature, as the latter results from a "tilting" of the wave vector. Giovannini *et al.* reported that the optical group delay increased with the square of the diameter of the beam, keeping all other parameters constant. Although their model has been validated through a wave-optics analysis, they interpreted their results in terms of a ray-optics picture. In their ray-optics model, the slow-light effect occurs because a ray traveling from the edge of the beam to the focus traverses a larger distance than an axial ray. This model predicts that the group delay scales as the square

of the beam diameter. In the present work, we report that the group velocity decreases linearly with the OAM value ℓ of the beam. Because the diameter of an LG beam scales as the square root of the ℓ value, the scaling law that we observe is consistent with that reported by Giovannini *et al.* We have interpreted this dependence (see Supplement 1) as arising as a consequence of the twisted nature of the optical wavefront.

Physically realizable beams, which carry finite energy, possess spatial phase and intensity structures differing from those of plane waves. LG modes are among the most commonly encountered examples of such beams, and are solutions to the paraxial wave equation. It may therefore be more transparent to frame the initial theoretical development in the language of pure LG modes, which serve as a more natural basis in which to consider slow-light effects in vacuum arising from a twisting of optical wavefronts. Notwithstanding the aesthetic and pedagogical appeal of a pure-LG-mode theory, our experiment is carried out using vortex beams, such as hypergeometric Gaussian (HyGG) ones, as these are more readily generated experimentally for reasons that will be made clear later [12]. LG modes are an orthonormal and complete set, in terms of which any arbitrary paraxial mode can be expanded [13], including HyGG modes. They are characterized by azimuthal and radial mode indices, ℓ and p, respectively. These modes are eigenstates of orbital angular momentum (OAM), and in vacuum carry OAM values of $\ell\hbar$ per photon along their propagation direction [14,15]. LG modal transverse intensity profiles feature intensity maxima at $r_{\max} = w(z)\sqrt{|\ell|/2}$, where $w(z)$ is the beam radius upon propagation [16]. The LG mode phase fronts have helical structures, and in vacuum are given by

$$\Phi^{\mathrm{LG}}(\mathbf{r}, \omega) = \frac{\omega}{c} z + \frac{\omega r^2}{2cR} + \ell\varphi - (2p + |\ell| + 1)\zeta, \qquad (1)$$

where $R := R(z, \omega)$ is the radius of curvature of the beam phase front, $\zeta := \zeta(z, \omega)$ is the Gouy phase [17], defined in Supplement 1, and r, φ, z are the standard cylindrical coordinates. The dependence exhibited by Φ^{LG} on its spatial coordinates $\mathbf{r}$, angular frequency ω, and the indices ℓ and p suggests that the phase velocity of these LG modes also depends on these values. Indeed, when explicitly calculated, the phase velocity is found to depend on r, ω, ℓ, and p, i.e., $v_{\mathrm{ph}}(r, z; \omega; p, \ell)$. This concept is illustrated in Fig. S1 of Supplement 1, which shows the spatial dependence of the phase fronts associated with Gaussian and spherical waves. This phase velocity leads to the conclusion that v_g is a function of r, z, ω, p, and ℓ, i.e., $v_g(r, z; \omega; p, \ell)$.

The group velocity is calculated by means of a procedure described in Supplement 1, where we also show that the slow-light effect arises largely from the structure of the wavefront radius of curvature, as distinct from the Gouy phase effect already discussed in the theoretical literature [18–20]. Indeed, the Gouy phase effect is an order of magnitude smaller than that observed in our experiment. Notably, the slow-light effects investigated here are observed to arise due to the twisting of the optical phase front itself, which causes the beam's intensity maximum to follow a hyperbolic trajectory.

The group velocities associated with LG modes having different p and ℓ indices are shown as functions of distance in Fig. 1. Figure 1(a) demonstrates that beams with $\ell = 0$ propagate at subluminal and superluminal speeds depending on propagation distance for all values of p. Specifically, for propagation distances bounded by $|z| \le z_R$, these modes exhibit superluminal speeds,

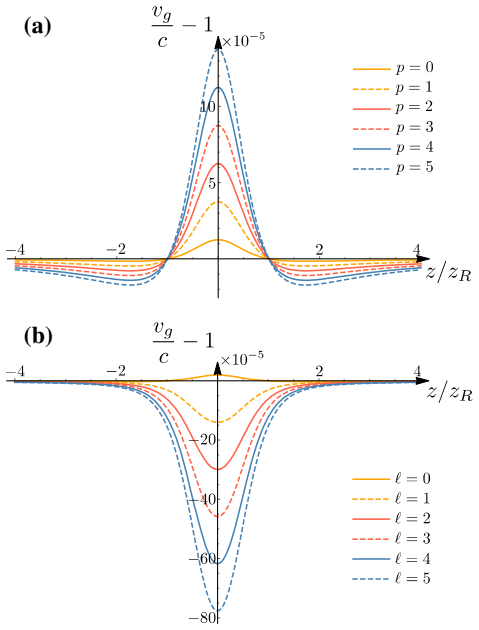

Fig. 1. Group velocities of focused Laguerre–Gauss modes as a function of propagation distance. (a) Group velocities as a function of propagation distance for LG modes with $\ell = 0$ and various values of p. These velocities pertain to the on-axis case, $r = 0$. Three different propagation regions can be identified: a first subluminal zone $z < -z_R$, a superluminal zone $|z| < z_R$, and a second subluminal zone $z > z_R$, where $z_R = \omega w_0^2/(2c)$ is the Rayleigh range, at which all modes travel at speed c. (b) Propagation dependence of group velocities for LG beams characterized by $p = 0$ and different values of ℓ. These group velocities are calculated not along the beam axis but at the radial position corresponding to the beam intensity maximum $r_{\max} = w(z)\sqrt{|\ell|/2}$. $r_{\max}$ defines the circle through which will pass all rays associated with a given LG mode in the ray tracing picture. With the exception of the $\ell = 0$ case, all modes are found to exhibit subluminal behavior throughout propagation. These results are obtained from simulations of light at a wavelength of 795 nm with a beam waist of 2.5 mm, focused by a thin lens of focal length 400 mm.

which at the waist increase linearly by $\delta v_g^{(p)} = 2.5 \times 10^{-5}$ cp for the fairly typical case of light at 795 nm with a beam waist of 100 μm. At the positions $z = \pm z_R$, where $z_R = \omega w_0^2/(2c)$ is the Rayleigh range, all modes propagate at c. Beyond z_R, subluminality can be observed. Despite their fast-light behavior at the waist, beams with $p \neq 0$ still lag behind the Gaussian mode as a result of their having experienced subluminal velocities prior to z_R.

The competing slow- and fast-light effects characterizing the propagation of $p \neq 0$ modes cancel to a significant extent for propagation distances beyond z_R, rendering p-index-induced pulse delays extremely difficult to measure. By contrast, for a fixed $p = 0$, LG modes are found to exhibit slow-light behavior for all propagation distances and all values of ℓ, as shown in Fig. 1(b). In this case, light speed reduction at the waist increases linearly with ℓ by $\delta v_g^{(\ell)} = -1.6 \times 10^{-4}\, c\ell$ for light at 795 nm with a beam waist of 100 μm. Although this effect is small, the time delay experienced by $\ell \neq 0$ pulses increases monotonically with propagation distance, reaching measurable values far from the waist. Nonetheless, the expected time delays for $\ell \neq 0$ relative to $\ell = 0$ Gaussian pulses are on the order of a few femtoseconds for the wavelength of light and beam waist considered, since the portions

of an $\ell \neq 0$ beam that are maximally intense experience more pronounced phase front curvature effects. A ray tracing picture, however, may be relied on in order to explain why beams carrying different OAM exhibit subluminal behaviors. In this picture, optical beams with higher values of OAM possess higher transverse wave vectors, so that the longitudinal components of their wave vectors are reduced. Therefore, their phase velocities are decreased as a consequence of increasing their OAM values. However, this geometrical optics picture is not fully accurate, since it is incapable of explaining superluminal effects of the sort observed in Fig. 1(a). Therefore, the need for a highly accurate arrival time measurement strategy is clearly indicated [11,21].

A schematic of our experimental setup is shown in Fig. 2. We measured the relative time delay between a Gaussian reference pulse and an $\mathrm{HyGG}_\ell = \sum_p c_p \mathrm{LG}_{p,\ell}$ pulse by implementing a technique analogous to noncollinear intensity autocorrelation (see Supplement 1 for more details) is more accurate. We spatially overlap these noncollinear pulsed beams inside a beta-barium borate (BBO) nonlinear crystal. A time delay is introduced between the two pulses using an optical delay stage. When this delay is minimized, the pulses are spatially and temporally overlapped within the crystal, leading to maximization of the noncollinear second-harmonic generation output pulse intensity. In this way, time delays experienced by the test beam can be detected by measuring the delay stage movement required to restore maximal pulse overlap. Using this technique, changes in relative arrival times of the Gaussian and twisted pulses induced by increases in the HyGG mode ℓ index can be measured within femtoseconds.

Figure 3(a) shows normalized power measured as a function of the delay stage position using the autocorrelation technique described (see Supplement 1), for HyGG modes with various values of ℓ. As can be seen, measurable shifts occurred between all HyGG modes presented in the figure. These peak shifts arise from differences in the pulse arrival time induced by the subluminal

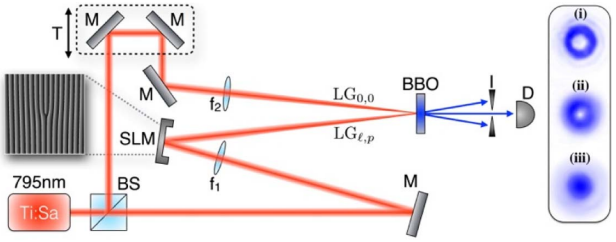

Fig. 2. Experimental setup for measuring subluminal speeds of twisted pulsed beams in vacuum. The test HyGG_ℓ beam is generated using a spatial light modulator (SLM) onto which is displayed the hologram shown in the figure. Reference $\mathrm{LG}_{0,0}$ and test HyGG_ℓ beams are focused into a type-I beta-barium borate (BBO) crystal. Second-harmonic generation (SHG) output transverse intensity profiles of the test, cross, and reference beams are shown in parts (i)–(iii) of the rightmost inset. When the delay between the test and reference arms is on the order of the pulse duration, one photon from each can be upconverted to produce an SHG photon. By conservation of linear momentum, this photon will exit the BBO crystal at the bisector between the SHG beams produced by the test and reference beams alone. Conservation of OAM further requires that the SHG outputs (i)–(iii) carry OAM values of 2ℓ, ℓ, and 0 [22,23]. The inset shows beam profiles obtained experimentally for the case $\ell = 1$. Note that the hologram shown here generates a pure ℓ mode with an infinite superposition of p modes, where most of the power resides in the fundamental $p = 0$ mode. Legend: BS-beam splitter, T-delay line (trombone), M-mirror, f-lens, I-iris, and D-detector.

speeds experienced by different HyGG beams during propagation. In particular, the shift in peak position between the $\mathrm{LG}_{0,0}$ and HyGG_6 modes is approximately 7 μm, corresponding to a time delay of 23 fs, from which can be inferred a maximum fractional group velocity drop of 0.1% relative to c. This fractional velocity drop is determined from the theoretical curves plotted in Fig. 1.

The velocity drop recorded here is that corresponding to the $z = 0$ propagation position, and it therefore represents the slowest pulse propagation speed reached during the experiment. Time delays experienced by various HyGG_ℓ modes relative to the $\mathrm{LG}_{0,0}$ reference mode are shown in Fig. 3(b). These results reveal the expected linear dependence of pulse arrival time on ℓ for a specific propagation distance (see Supplement 1). This dependence may be understood with reference to Eq. (1), which indicates that phase is a function of the index ℓ and the radial curvature $R(z, \omega)$. While the ℓ index is clearly shown to play an important role in determining the group velocity of an LG mode, the effect of the p index is far less pronounced, for reasons discussed earlier. Thus, HyGG and LG beams will experience similar time delays, up to some correction factor. In the far-field, the group velocity of any LG mode asymptotically approaches c; see Fig. 1. Therefore, the time delay between $\mathrm{LG}_{p,\ell}$ and $\mathrm{LG}_{0,0}$ reaches a constant value far from the focus.

A number of conclusions can be drawn from the investigation presented here. First, the group velocities of twisted LG beams (HyGG beams) have been shown to differ measurably from those of Gaussian pulses, even in free space. This surprising phenomenon can be interpreted as arising from diffraction effects in

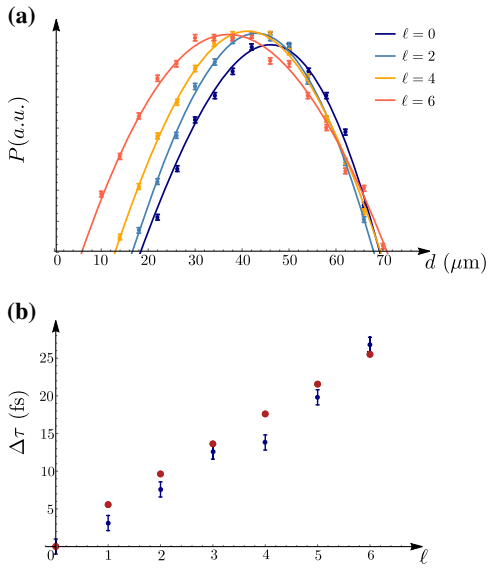

Fig. 3. Subluminal light propagation of HyGG modes in free space. (a) Normalized power obtained from the autocorrelation technique described in the text as a function of delay stage position, d, for HyGG beams with $\ell = 0, 2, 4, 6$. Raw data are presented along with the fits used to estimate pulse peak positions. Power was measured at each stage position over a period of sufficient length to suppress Poissonian noise. The widths of the autocorrelation traces were found to fall in the range of 201 ± 6 μm, but in the interest of clarity, only the peaks of the autocorrelation traces are shown. (b) Arrival times of HyGG_ℓ pulses relative to an $\mathrm{LG}_{0,0}$ reference pulse extracted from peak positions determined directly from experimental data. A linear relationship between arrival time and ℓ is observed, and the experimental data (blue dots) are plotted along with theoretical data (red dots) obtained from the group velocity expression derived in Supplement 1.

vacuum, as it results in wavelength-dependent phase and group velocities. This is different from the standard approach to calculating group velocities for a pulse in a medium considering the dispersion relation. Further, exotic phase and group velocity effects inevitably arise for any physically realizable beam, for these must necessarily possess nontrivial spatial amplitude and phase structures, which result in other-than-luminal propagation speeds. For the particular case of twisted light, spatial structure can lead to slow-light effects whose magnitudes depend directly on various beam parameters, including the modal ℓ and p indices.

These findings carry great practical significance, particularly for classical and quantum communication and quantum information with twisted light [24–26]. Single photon sources have a limited pulse width, which depends on the pump pulse duration. Although it is possible to implement some of the quantum protocols, such as the decoy state quantum key distribution (QKD), with an attenuated coherent state, most of the quantum information schemes require photons to have a certain temporal coherence. This temporal coherence length is on the order of several tens of micrometers (femtosecond duration), which is exactly the temporal length of the laser pulse that we have studied. Therefore, our results, both theoretical model and experimental results, are valid for the case of single photons as well. In light of significant recent interest in implementing QKD and quantum computations with structure photons, one must take the presented subluminal effect for twisted photons into account.

Unless differences induced in LG mode pulse arrival times are compensated for, the subluminial and superluminal effects reported here could result in the out-of-sequence detection of pulses, or the failure of quantum logic gates. A photon in an OAM qubit state $|\psi_{\alpha,\beta}\rangle = (\alpha|0\rangle + \beta|\ell\rangle)$, where $|0\rangle$ and $|\ell\rangle$, respectively, represent $\mathrm{LG}_{0,0}$ and $\mathrm{LG}_{0,\ell}$ modes, generated by a sender (Alice) at time $t = 0$ will travel at a group velocity that depends on the values of α and β. As a result, the photon's arrival time at the receiver (Bob) will be given by $t_{\alpha,\beta} = \int_{z=\mathrm{source}}^{z=\mathrm{reciever}} \mathrm{d}z/v_g^{\alpha,\beta}(z)$. As this treatment shows, the message will reach Bob at a time that will depend on α and β. More generally, photons associated with an arbitrary mode $|\psi_{\{c_\ell\}}\rangle = \sum_{\ell=0}^{+\infty} c_\ell|\ell\rangle$ will exhibit arrival times $t_{\{c_\ell\}}$, which will depend on the set $\{c_\ell\}$ of amplitudes associated with each LG component comprising the beam of interest.

Photon OAM has been shown to represent a valid state label that can be used to distinguish one photon from another. From a quantum information standpoint, therefore, one could imagine how a Hong–Ou–Mandel (HOM)-type experiment could exhibit great sensitivity to the slow-light effects explored here. In particular, a HOM experiment carried out, for example, with one photon in an $\mathrm{LG}_{0,0}$ mode and the other in a coherent superposition of $\mathrm{LG}_{0,0}$ and $\mathrm{LG}_{0,1}$ modes would already be expected to register only a limited dip, due to the partial distinguishability of the two photons on the basis of their OAM. However, our work has shown that a second effect will also be at play: in addition to being damped due to the partial distinguishability of the incident photons, one would also expect the HOM dip obtained in such an experiment to be *skewed* as a direct consequence of the different arrival times of the two photons. Given the critical importance of the HOM effect in quantum information protocols, this second effect may have a wide range of practical consequences.

Notably, our results should not be misattributed to lens thickness effects [27], which have been avoided by removing any lenses in the path of the LG beam following its generation. We have shown that time delays on the order of several femtoseconds can arise between LG modes due to the group velocity effects we have explored, depending on the geometries of the sender and receiver optics. As a result, any communication scheme [28,29] or computation protocol [30] relying on twisted light must account for the slow and fast light effects that we have demonstrated.

Funding. Canada Research Chairs; Canada Excellence Research Chairs (CERC); Government of Canada; Natural Sciences and Engineering Research Council of Canada (NSERC).

Acknowledgment. We thank Peter Banzer and Miles J. Padgett for fruitful discussions.

See Supplement 1 for supporting content.

REFERENCES

1. M. Born and E. Wolf, *Principles of Optics: Electromagnetic Theory of Propagation, Interference and Diffraction of Light* (Cambridge University, 1999), Chap. 1.
2. L. V. Hau, S. E. Harris, Z. Dutton, and C. H. Behroozi, Nature **397**, 594 (1999).
3. A. Dogariu, A. Kuzmich, and L. Wang, Phys. Rev. A **63**, 053806 (2001).
4. M. S. Bigelow, N. N. Lepeshkin, and R. W. Boyd, Science **301**, 200 (2003).
5. M. Notomi, K. Yamada, A. Shinya, J. Takahashi, C. Takahashi, and I. Yokohama, Phys. Rev. Lett. **87**, 253902 (2001).
6. N.-H. Liu, S.-Y. Zhu, H. Chen, and X. Wu, Phys. Rev. E **65**, 046607 (2002).
7. J. Sharping, Y. Okawachi, and A. Gaeta, Opt. Express **13**, 6092 (2005).
8. G. M. Gehring, A. Schweinsberg, C. Barsi, N. Kostinski, and R. W. Boyd, Science **312**, 895 (2006).
9. N. V. Budko, Phys. Rev. Lett. **102**, 020401 (2009).
10. K. B. Kuntz, B. Braverman, S. H. Youn, M. Lobino, E. M. Pessina, and A. I. Lvovsky, Phys. Rev. A **79**, 043802 (2009).
11. D. Giovannini, J. Romero, V. Potoček, G. Ferenczi, F. Speirits, S. M. Barnett, D. Faccio, and M. J. Padgett, Science **347**, 857 (2015).
12. E. Karimi, G. Zito, B. Piccirillo, L. Marrucci, and E. Santamato, Opt. Lett. **32**, 3053 (2007).
13. A. E. Siegman, *Lasers* (University Science, 1986).
14. L. Allen, M. W. Beijersbergen, R. Spreeuw, and J. Woerdman, Phys. Rev. A **45**, 8185 (1992).
15. M. Padgett, J. Courtial, and L. Allen, Phys. Today **57**(5), 35 (2004).
16. M. Berry and K. McDonald, J. Opt. A **10**, 035005 (2008).
17. T. Visser and E. Wolf, Opt. Commun. **283**, 3371 (2010).
18. Z. Horváth, J. Vinkó, Z. Bor, and D. Von der Linde, Appl. Phys. B **63**, 481 (1996).
19. M. A. Porras, I. Gonzalo, and A. Mondello, Phys. Rev. E **67**, 066604 (2003).
20. R. J. Mahon and J. A. Murphy, J. Opt. Soc. Am. A **30**, 215 (2013).
21. R. Trebino, K. W. DeLong, D. N. Fittinghoff, J. N. Sweetser, M. A. Krumbügel, B. A. Richman, and D. J. Kane, Rev. Sci. Instrum. **68**, 3277 (1997).
22. T. Roger, J. J. Heitz, E. M. Wright, and D. Faccio, Sci. Rep. **3**, 3491 (2013).
23. J. Courtial, K. Dholakia, L. Allen, and M. Padgett, Phys. Rev. A **56**, 4193 (1997).
24. G. Gibson, J. Courtial, M. J. Padgett, M. Vasnetsov, V. Pas'ko, S. M. Barnett, and S. Franke-Arnold, Opt. Express **12**, 5448 (2004).
25. G. Molina-Terriza, J. P. Torres, and L. Torner, Nat. Phys. **3**, 305 (2007).
26. E. Nagali, L. Sansoni, F. Sciarrino, F. De Martini, L. Marrucci, B. Piccirillo, E. Karimi, and E. Santamato, Nat. Photonics **3**, 720 (2009).
27. E. Karimi, C. Altucci, V. Tosa, R. Velotta, and L. Marrucci, Opt. Express **21**, 24991 (2013).
28. J. Wang, J. Yang, I. M. Fazal, N. Ahmed, Y. Yan, H. Huang, Y. Ren, Y. Yue, S. Dolinar, M. Tur, and A. E. Willner, Nat. Photonics **6**, 488 (2012).
29. M. Krenn, R. Fickler, M. Fink, J. Handsteiner, M. Malik, T. Scheidl, R. Ursin, and A. Zeilinger, New J. Phys. **16**, 113028 (2014).
30. F. Cardano, F. Massa, H. Qassim, E. Karimi, S. Slussarenko, D. Paparo, C. de Lisio, F. Sciarrino, E. Santamato, R. W. Boyd, and L. Marrucci, Sci. Adv. **1**, e1500087 (2015).

Chapter 6

Observation of quantum recoherence of propagating twisted photon pairs

This chapter is based on the following paper:

1. **F. Bouchard**, J. Harris, H. Mand, N. Bent, E. Santamato, R. W. Boyd, and E. Karimi, "Observation of quantum recoherence of photons by spatial propagation," *Scientific Reports* **5**, 15330 (2015).

6.1 Spontaneous parametric down conversion

In this chapter, we study quantum properties of twisted photons as they propagate in free-space. The quantum formalism employed below is valid for a low number of quantum systems. Thus, the use of a laser beam would not be appropriate for a quantum experiment as it is usually composed of a very large number of photons. Hence, in order to perform fundamental tests of twisted photons at the quantum regime, one needs the ability to operate an optical experiment in the single photon regime.

There has been many efforts to develop sources of single photons due to their applications in the field of quantum information, computation and communication. One of the most popular and straightforward techniques to realize the production of photon pairs, namely spontaneous parametric down conversion (SPDC), may be

achieved using a nonlinear crystal [16]. Throughout this process, intense pulses of light interact with the nonlinear crystal and in some cases spontaneously produce a pair of single photons. Traditionally, the intense input beam is referred to as the *pump* beam and the down-converted photons are referred to as the *signal* and *idler* photons. This nonlinear process is parametric and thus requires the initial state and the final state of the atoms making up the material to be equal, resulting in the conservation of energy, linear momentum and orbital angular momentum. Hence, the sum of the energy of the two down-converted photons must be equal to the energy of the pump photon. Conservation of linear momentum will result in the formation of a cone of single photons, where photon pairs lie at opposite ends of the SPDC cone. Interestingly, conservation of orbital angular momentum in the process of SPDC leads to the *entanglement* of the orbital angular momentum quantum states of the photon pairs [8]. These entangled orbital angular momentum states consist of the basis for our work in this chapter.

6.2 Density matrix formalism

In quantum mechanics, the state of a system is typically represented as a vector $|\psi\rangle$, residing in a Hilbert space. In general, such states may be represented as a superposition of eigenstates $|n\rangle$, i.e. $|\psi\rangle = \sum_n c_n|n\rangle$, where c_n represents complex coefficients. A more general representation of quantum states that may accounts for a loss in coherence is given by the density matrix formalism. A density matrix, $\hat{\rho}$, generalizes the previous vector representation in the following way, $\hat{\rho} = |\psi\rangle\langle\psi|$, where $\langle\psi|$ corresponds to the conjugate transpose of $|\psi\rangle$. However, the density matrix formulation incorporates the effect of an incoherent superposition of states, i.e. $\hat{\rho} = \sum_i p_i|\psi_i\rangle\langle\psi_i|$, analogous to unpolarized light in optics.

6.3 Quantum state tomography

In order to experimentally reconstruct the density matrix associated with a quantum system, one may perform quantum state tomography. Obviously, this method is not effective when one desires to measure one system, as it is well-known that the quantum system will be disturbed if one attempts to measure it. Hence, state tomography is typically performed on an ensemble of identically prepared quantum systems. Let us

first review that scheme of quantum state tomography in the case of a 2-dimensional system, which applies to polarisation and 2-dimensional orbital angular momentum states of single photons. We will further extend this method to high-dimensional systems.

6.3.1 Mutually unbiased bases

Mutually unbiased bases (MUBs) are of great importance in many areas of quantum information, e.g. quantum key distribution and quantum state tomography [17]. In particular, they consist of orthogonal bases such that two elements, $|\psi_i\rangle$ and $|\psi_j\rangle$, belonging to different MUBs obey the following inner product relation, $|\langle\psi_i|\phi_j\rangle|^2 = 1/d$, where d is the dimensionality of the MUBs. Furthermore, an important result in quantum information is the existence of a number of MUBs for a specific dimension. In the particular case of dimensions given by powers of prime numbers, the number of MUBs is given by $d+1$.

Hence, in dimension 2, the (2+1) mutually unbiased bases are given by,

$$\{\mathrm{I}\} = \{|0\rangle, |1\rangle\}, \tag{6.1}$$

$$\{\mathrm{II}\} = \left\{\frac{|0\rangle + |1\rangle}{\sqrt{2}}, \frac{|0\rangle - |1\rangle}{\sqrt{2}}\right\}, \tag{6.2}$$

$$\{\mathrm{III}\} = \left\{\frac{|0\rangle + i|1\rangle}{\sqrt{2}}, \frac{|0\rangle - i|1\rangle}{\sqrt{2}}\right\}. \tag{6.3}$$

In the case of polarisation states of light, we have $\{\mathrm{I}\} = \{|L\rangle, |R\rangle\}$, $\{\mathrm{II}\} = \{|H\rangle, |V\rangle\}$ and $\{\mathrm{III}\} = \{|A\rangle, |D\rangle\}$.

6.3.2 Tomography of a qubit

The reconstruction of the state of a quantum system via state tomography is achieved by projecting the state on each element of every MUB, thus requiring a set of $d(d+1)$ measurements. Although there exists tomographical schemes requiring a smaller number of measurements to reconstruct the density matrix of the state, this *overcomplete* method is conceptually straightforward to implement. Going back to the example of polarisation, this results in measuring the normalized probability of the projective

measurements P_L, P_R, P_H, P_V, P_A and P_D [18]. From these projective measurements, one may calculate the Stokes parameters S_i given by,

$$S_0 = P_L + P_R, \tag{6.4}$$
$$S_1 = P_H - P_V, \tag{6.5}$$
$$S_2 = P_A - P_D, \tag{6.6}$$
$$S_3 = P_L - P_R. \tag{6.7}$$

The reconstructed density matrix is then given in terms of the Pauli matrices $\hat{\sigma}_i$,

$$\hat{\rho} = \frac{1}{2}\sum_{i=0}^{3} \frac{S_i}{S_0}\hat{\sigma}_i. \tag{6.8}$$

6.3.3 High-dimensional quantum state tomography

In high-dimensional quantum systems, state tomography may be performed provided that one has the ability to measure the probability of projective measurements of each d elements of every $d+1$ MUBs. Such a projective measurement is denoted as $P_m^{(\alpha)}$, where m labels the states with $(m = 1, ..., d)$ and α labels the MUB with $(\alpha = 1, ..., d+1)$. Following this notation, projection operators are give by $\Pi_m^{(\alpha)} = |\psi_m^{(\alpha)}\rangle\langle\psi_m^{(\alpha)}|$. One could now express the projective measurements in terms of the projector operators, i.e. $P_m^{(\alpha)} = \mathrm{Tr}\left[\hat{\rho}\,\Pi_m^{(\alpha)}\right]$, where $\mathrm{Tr}\,[.]$ is the trace operator. Finally, the reconstructed density matrix may be expressed in terms of the projective measurements and projection operators, i.e.

$$\hat{\rho} = \sum_{\alpha=1}^{d+1}\sum_{m=1}^{d} P_m^{(\alpha)}\Pi_m^{(\alpha)} - \hat{I}, \tag{6.9}$$

where $\hat{I}$ is the d-dimensional identity matrix.

SCIENTIFIC REPORTS

OPEN

Observation of quantum recoherence of photons by spatial propagation

Received: 31 July 2015
Accepted: 23 September 2015
Published: 15 October 2015

Frédéric Bouchard[1], Jérémie Harris[1], Harjaspreet Mand[1], Nicolas Bent[1], Enrico Santamato[2], Robert W. Boyd[1,3] & Ebrahim Karimi[1]

Entanglement is at the heart of many unusual and counterintuitive features of quantum mechanics. Once two quantum subsystems have become entangled, it is no longer possible to ascribe an independent state to either; instead, the subsystems are completely described only as part of a greater, composite system. As a consequence of this, each entangled subsystem experiences a loss of coherence following entanglement. We refer to this decrease in coherence as *decoherence*. Decoherence leads inevitably to the leaking of information from each subsystem to the composite entangled system. Here, we demonstrate a process of decoherence reversal, whereby we recover information lost from the entanglement of the optical orbital angular momentum and radial profile degrees of freedom possessed by a photon pair. These results carry great potential significance, since quantum memories and quantum communication schemes depend on an experimenter's ability to retain the coherent properties of a particular quantum system.

When one quantum system becomes entangled with another, its purity is diminished as phase information is lost to the second (ancilla) Hilbert space. Once the system has lost coherence, its state cannot be described independently of the ancilla. The system is said to have undergone decoherence, and the combined state of the system and ancilla must be specified in order to capture the information originally contained in the system alone[1,2].

In quantum computation and communication protocols, only the state of the system is generally accessible, meaning that its entanglement with an ancilla produces a loss of available information[3]. Therefore, the ability to reverse the decoherence process and recover the original system state holds great promise in many areas[4–7]. We demonstrate the reversal of propagation-induced decoherence, which we term *recoherence*. We show that quantum information in the orbital angular momentum (OAM) degree of freedom of an entangled photon pair can be lost and retrieved through propagation, by manipulating the degree of entanglement (DOE) between their OAM and radial mode Hilbert spaces. This effect should not be confused with entanglement migration, in which information is transferred between wavefunction phase and amplitude by propagation, rather than having been lost to ancilliary Hilbert spaces[8], nor should it be mistaken for quantum erasure, which is achieved by information loss due to projective measurement[9]. The effects explored here are of more general interest, as they are brought upon by the action of a unitary operation (free spatial propagation) that is usually assumed to preserve OAM information content. The general decoherence/recoherence paradigm is illustrated in Fig. 1, which shows an initial state consisting of a system $|\psi_1\rangle_s + |\psi_2\rangle_s$ and ancilla $|\varphi\rangle_a$, which are entangled by the decoherence process, producing a combined state $|\psi_1\rangle_s \otimes |\varphi_1\rangle_a + |\psi_2\rangle_s \otimes |\varphi_2\rangle_a$. This entanglement is then reversed by (unitary) spatial propagation, and the original state recovered.

[1]Department of Physics, University of Ottawa, 25 Templeton St., Ottawa, Ontario, K1N 6N5 Canada. [2]Dipartimento di Scienze Fisiche, Universitá di Napoli "Federico II", Complesso di Monte S. Angelo, 80126 Napoli, Italy. [3]Institute of Optics, University of Rochester, Rochester, New York, 14627, USA. Correspondence and requests for materials should be addressed to E.K. (email: ekarimi@uottawa.ca)

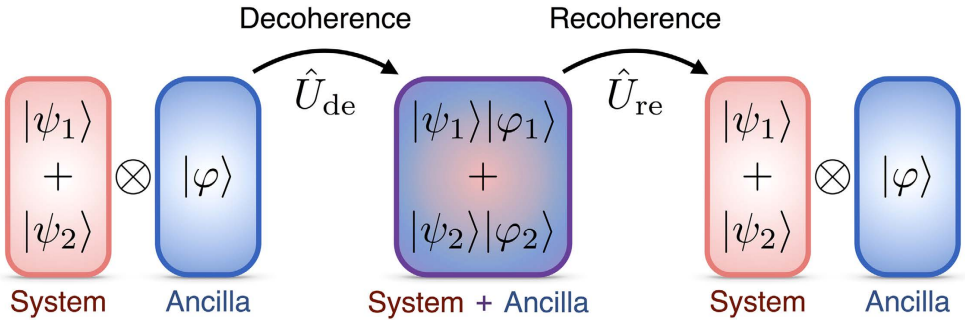

Figure 1. Illustration of the processes of decoherence and recoherence. The system's initial state ray takes the form $|\psi_1\rangle + |\psi_2\rangle$, where $|\psi_1\rangle$ and $|\psi_2\rangle$ are themselves state rays in the system Hilbert space. Before decoherence, the system and ancilla Hilbert spaces are separable, and a state may be ascribed to each independently. Both kets describing the system are associated with the same ancilla ket $|\varphi\rangle$. Upon decoherence induced by the unitary operator $\hat{U}_{\rm de}$, the state of the ancilla becomes contingent on the state of the system, so that the ancilla kets $|\varphi_1\rangle$ and $|\varphi_2\rangle$, respectively associated with the $|\psi_1\rangle$ and $|\psi_2\rangle$ system states, are no longer identical, i.e. $\hat{U}_{\rm de}(|\psi_1\rangle + |\psi_2\rangle) \otimes |\varphi\rangle = |\psi_1\rangle|\varphi_1\rangle + |\psi_2\rangle|\varphi_2\rangle$. Therefore, the two Hilbert spaces become non-separable, and coherence is lost, if one can only access the system. During the recoherence process, application of a unitary operator $\hat{U}_{\rm re}$ causes the kets $|\varphi_1\rangle$ and $|\varphi_2\rangle$ to recover their initial form $|\varphi\rangle$, allowing system Hilbert space coherence to be regained, i.e. $\hat{U}_{\rm re}(|\psi_1\rangle|\varphi_1\rangle + |\psi_2\rangle|\varphi_2\rangle) = (|\psi_1\rangle + |\psi_2\rangle) \otimes |\varphi\rangle$.

We observed the recoherence effect by choosing as the system the OAM degrees of freedom of an entangled photon pair, and by taking the photons' radial profiles to represent the ancilla. The entangled pair was generated from a pump photon produced in a Laguerre-Gauss (LG) mode. LG modes are a well-characterized family of solutions to the paraxial wave equation, and form an orthonormal and complete basis[10]. LG beams are of particular interest since they represent eigenstates of OAM. They carry an OAM of $\ell\hbar$ per photon[11] and are given by

$$\mathrm{LG}_{p,\ell}(r, \phi, z) \propto e^{i\ell\varphi}\mathcal{F}_{p,\ell}(r, z), \tag{1}$$

where p and ℓ are the modal radial and azimuthal indices, and r, ϕ, z are the standard cylindrical coordinates. In this representation, the dependence of the LG transverse profile on the radial and longitudinal coordinates r and z is entirely contained within $\mathcal{F}_{p,\ell}(r, z)$[12], which possesses a doughnut-shaped amplitude for $\ell \neq 0$, and a Gaussian radial profile for $\ell = 0$.

Results

Recently, optical OAM conservation has been demonstrated during spontaneous parametric down conversion (SPDC)[13,14]. In SPDC, a single photon is frequency down-converted in a nonlinear material to produce two photons whose total OAM is equal to that of the incident pump photon. The generated photons are known as the signal and idler, and will in general belong to modes with different OAM values. Consequently, their radial modes will evolve differently upon free-space propagation. Notwithstanding the disparate modal evolution of the signal and idler, the transverse profiles of both SPDC photons must overlap within the nonlinear crystal immediately following down conversion, to ensure continuity of field intensities during SPDC.

We consider the case $p = 0$ and take $|\ell_{\mathcal{S}}, \ell_i\rangle := |\ell_{\mathcal{S}}\rangle_{\mathcal{S}} \otimes |\ell_i\rangle_i$ to denote an optical state in which the signal (idler) photon carries $\ell_{\mathcal{S}}$ (ℓ_i) units of OAM, and $\left|F_{\ell_{\mathcal{S}},\ell_i}(z)\right\rangle := \left|F_{\ell_{\mathcal{S}}}(z)\right\rangle_s \otimes \left|F_{\ell_i}(z)\right\rangle_i$ to represent the radial profiles $F_{\ell_{\mathcal{S}}}(r, z)$ and $F_{\ell_i}(r, z)$ of the signal and idler, where we have dropped the index p for simplicity, and the subscripts s and i indicate the signal and idler photons, respectively. For an incident pump photon with $\ell = 1$, the state of the SPDC pair is

$$|\psi(z)\rangle = \frac{1}{\sqrt{2}}(|1, 0\rangle \otimes |F_{1,0}(z)\rangle + e^{i\theta}|0, 1\rangle \otimes |F_{0,1}(z)\rangle), \tag{2}$$

where θ is the phase between the SPDC photon pair states. Here we account only for signal and idler photons generated with either 0 or 1 units of OAM (see Supplementary Information (SI)).

Immediately following SPDC, continuity of the optical fields in the nonlinear crystal requires that $|F_{\ell,0}(0)\rangle = |F_{0,\ell}(0)\rangle := |F(0)\rangle$. Consequently, the radial profile component of the total state can be factored, and $|\psi(0)\rangle = \frac{1}{\sqrt{2}}(|1, 0\rangle + e^{i\theta}|0, 1\rangle) \otimes |F(0)\rangle$ (see SI). Therefore, the OAM state of the system is pure immediately following photon pair generation, and the radial and OAM state components of $|\psi(0)\rangle$ are separable. Upon propagation, this separability disappears as the transverse profiles become

entangled with the OAM state of each photon, so that for $z \neq 0$, the two-photon state is described by Eq. (2) instead, and cannot be factorized. The unitary operator responsible for the entanglement of the OAM and radial mode Hilbert spaces is $\hat{U}(0, z) = \hat{U}^{(s)}(0, z) \otimes \hat{U}^{(i)}(0, z)$, with $\hat{U}^{(s,i)} = \exp(i\hat{H}^{(s,i)}z)$, $\hat{H}^{(s,i)} = -1/(2k)\Delta_{\perp}^{(s,i)}$ and where $\Delta_{\perp}^{(s,i)}$ denotes the transverse laplacian over the signal and idler Hilbert spaces, respectively. In the position representation, $\hat{U}^{(s,i)}$ takes the form of the Fresnel propagator (see SI).

The propagation effects described can be understood by considering the reduced density matrix $\rho_{\mathrm{OAM}}^{\mathrm{red}}(z)$ of the OAM Hilbert space alone. This matrix is obtained by tracing over the radial profile component of the total density matrix $\rho(z) = |\psi(z)\rangle\langle\psi(z)|$, and is found to take the form $\rho_{\mathrm{OAM}}^{\mathrm{red}}(z) = \frac{1}{2}(|1, 0\rangle\langle 1, 0| + |0, 1\rangle\langle 0, 1| + c(z)|1, 0\rangle\langle 0, 1| + c^*(z)|0, 1\rangle\langle 1, 0|)$, where $c(z) = e^{-i\theta}\left|\int_0^{\infty} F_{\ell}^*(r, z)F_0(r, z)rdr\right|^2$ (see SI). The reduced density matrix can be expressed alternatively as

$$\rho_{\mathrm{OAM}}^{\mathrm{red}}(z) = \frac{1}{2}\begin{pmatrix} 1 & c(z) \\ c^*(z) & 1 \end{pmatrix}. \tag{3}$$

The off-diagonal terms take values $c(0) = \exp(-i\theta)$ in the SPDC plane, and their magnitudes decrease with propagation distance z. This decreases the purity of the reduced density matrix, and increases the entanglement entropy of the OAM subspace. The purity of the reduced density matrix defined above is given by $\mathcal{P}(z) = \mathrm{Tr}\left[(\rho_{\mathrm{OAM}}^{\mathrm{red}}(z))^2\right]$, where $\mathrm{Tr}[\cdot]$ denotes the trace operation. The entanglement entropy of the OAM subspace is $\mathcal{S}(z) = -\sum_i \lambda_i \ln(\lambda_i)$, where λ_i are the eigenvalues of $\rho_{\mathrm{OAM}}^{\mathrm{red}}(z)$, and $\ln(\cdot)$ denotes the natural logarithm. Purity and entanglement entropy represent measures of the DOE of the system and ancilla; as $\mathcal{P}$ ($\mathcal{S}$) decreases (increases), the system and ancilla become increasingly entangled (and *vice-versa*). As a point of physical interest, we note that the decoherence of the OAM Hilbert space of the state presented in Eq. (2) does not occur due to the introduction of *ad hoc* classical noise in the phase term; rather, it arises from ignorance regarding ancillary degree (s) of freedom (radial mode) entangled with the quantum system under study (OAM).

For the sake of clarity, we have included the radial degree of freedom of the photon pairs in our analysis from the very beginning. Decoherence and recoherence effects due to the non-trivial evolution of the radial degree of freedom, are then derived straightforwardly. This treatment may lead the reader to think this effect unsurprising or rather obvious. Nevertheless, the quantum nature of the photonic radial degree of freedom has only recently been recognized and demonstrated[15]. Hence a naïve analysis of the propagation of OAM-entangled photon pairs would assume photon OAM to be robust against spatial propagation. Indeed, this error would be all the more understandable given that its underlying assumptions hold true for single photons; it is the fact that a multi-photon system is considered here that makes decoherence an issue. Unfortunately, quantum key distribution and quantum information applications depend heavily upon precisely the sort of multi-photon entanglement discussed here[16]. We note also that this coherence retrieval process is physically distinct from non-unitary projective post-selection, which can achieve similar ends, but entails the loss of a substantial number of photons. Moreover, the recoherence of a quantum photonic state arising from purely unitary evolution in space (or equivalently in time), is a completely novel, and hitherto unobserved, effect.

Our experimental setup is shown in Fig. 2. The output of a quasi-continuous wave UV laser operating with a repetition rate of 100 MHz and an average power of 150 mW at a wavelength of 355 nm is spatially cleaned and sent to a kinoform displayed on a Hamamatsu UV spatial light modulator (SLM1), which reshapes the spatial distribution of the incoming beam into a desired $\mathrm{LG}_{0,\ell}$ mode. The first diffracted order obtained from the reflection of the beam off the SLM is selected using an iris placed at the Fourier plane of the lens $f_1 = 200$ mm. The beam is then imaged from the UV SLM to a $L = 3$ mm thick type-I β-barium borate (BBO) crystal by means of a 4*f*-system ($f_1 = 200$ mm – $f_2 = 100$ mm). The BBO crystal is placed on a translational stage so as to allow the SPDC output to be imaged and analyzed for different propagation distances. The SPDC photons are separated into two different paths at a non-polarising beam splitter and then re-imaged on SLMs 2 and 3 (Hamamatsu) by means of additional 4*f*-systems ($f_3 = 400$ mm – $f_4 = 200$ mm). SLM 2 and SLM 3 perform the measurement on the OAM state of the down-converted photons. The measured photons are then coupled to single mode optical fibres and sent to avalanche photodiode (APD) detectors. The coincidence counts between the two detectors are measured by means of a coincidence box with a time window of 10 ns.

We generate OAM-entangled photon pairs from SPDC, which at the BBO crystal have identical radial intensity profiles. Upon propagation, their radial profiles will differ increasingly, causing system decoherence, and a decrease (increase) in the purity (entropy) of the photons' OAM states. By imaging the exit plane of the BBO crystal on a SLM and single mode optical fibre, we can retrieve the initial radial profiles, and achieve recoherence by recovering maximal OAM state purity. The BBO crystal is then mounted on a translational stage and moved along the beam axis to image different propagation planes, where only partial recoherence occurs. The purity of the OAM state is calculated from reconstructed density matrices obtained from OAM state tomography performed over the Hilbert space spanned by the basis

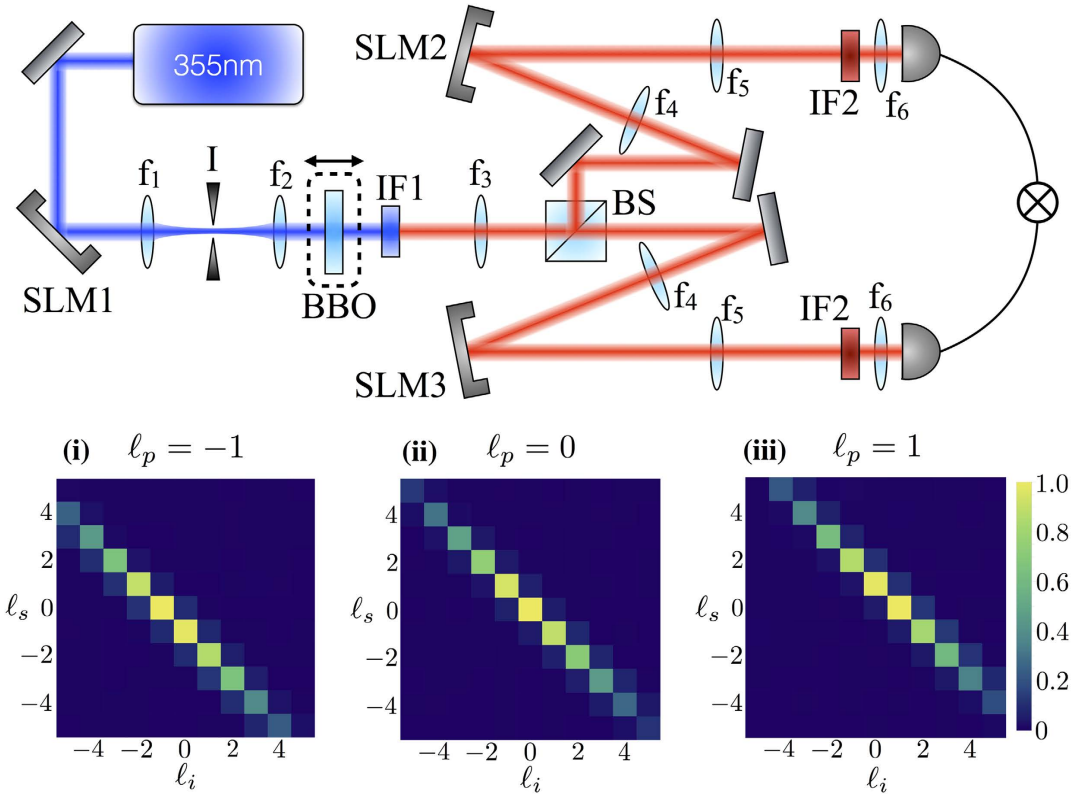

Figure 2. Experimental setup. Using SLM1, we impart an OAM of ℓ_p per photon on a beam of UV light, which is made to pass through a Type I β-barium borate (BBO) crystal for SPDC. The entangled photon pair is separated by a beam splitter, and each photon is imaged on a different SLM. Only when the pattern displayed on the SLM is complementary to the phase front of the incident photon will it be phase-flattened and coupled to a single-mode optical fibre for eventual detection by a coincidence counter. The BBO crystal is mounted on a translational stage, so that SPDC fields imaged on the SLMs correspond to different propagation ranges. Insets **(i)**, **(ii)** and **(iii)** show experimental OAM conservation matrices obtained for pump OAM values of $\ell_p = -1$, $\ell_p = 0$ and $\ell_p = 1$. These results confirm that OAM conservation is indeed verified in our optical system, indicating that the setup is capable of reliably measuring photon OAM.

$\{|0, 0\rangle, |0, 1\rangle, |1, 0\rangle, |1, 1\rangle\}$. Tomography is carried out by using SLMs and single mode optical fibres, which in combination carry out a function analogous to that of the polariser in polarisation state tomography[17,18]. Our apparatus allows the DOE between the OAM and radial profile states to be adjusted and measured with precision.

Figure 3a shows plots of system purity versus imaging position. The theoretically predicted increase of purity with imaging position is verified experimentally. Neither the theoretical nor the experimental curves reach their minimum possible purity of $P = 1/2$; hence, the OAM and radial profile Hilbert spaces are never maximally entangled (see SI). Instead, measured OAM state purities ranged from 0.55 to 0.84. In Fig. 3b, we show corresponding plots of system von Neumann entropy. Measured and theoretical values agree qualitatively, decreasing with imaging position, respectively ranging from 0.26 to 0.59, and 0 to 0.62. The purity and von Neumann entropy were found to differ from their theoretical counterparts at the image plane. We attribute this disagreement to the finite thickness of the BBO crystal, which means that in practice, SPDC does not occur in an infinitely thin plane, but within a range (3 mm) of positions in the crystal.

Discussion

This experiment shows that propagation-induced decoherence can be reversed to recover lost information, provided that a judicious choice of imaging optics is made by the experimenter. Following SPDC, the radial profiles of the signal and idler begin to differ upon propagation. The resulting entanglement between the signal and idler's respective OAM content and their radial profiles leads to a loss of accessible information from the bi-photon OAM Hilbert space. In our experiment, this information loss was reversed by the action of a lens and free propagation of the SPDC pair. Though the reversal of any quantum mechanical process must always be theoretically possible, these findings demonstrate that this reversibility can be observed in practice, even for decoherence phenomena. Apart from their being of

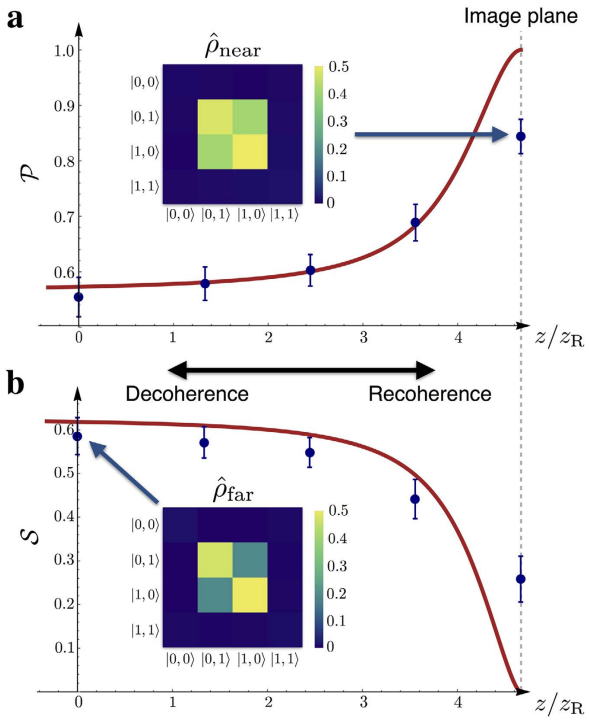

Figure 3. Purity and von Neumann entropy of the OAM state for different SPDC propagation distances. (**a**) Experimental and theoretical plots of OAM state purity. Experimental data were obtained over a propagation range of $4.7z_R = 21$ mm (see text), and the theoretical plot from the reconstructed density matrix Eq. (3) obtained from propagation simulations described in the main text and SI. (**b**) Experimental and theoretical plots of OAM state von Neumann entropy. Experimental data correspond to those plotted in part (**a**). Insets show reconstructed density matrices $\hat{\rho}_{\text{near}}$ and $\hat{\rho}_{\text{far}}$ obtained from experimental data at $z = 0$ and $z = 21$ mm (the near- and far-field positions). Only the absolute values of the matrices' off-diagonal elements were plotted, since their phases do not influence system purity or entropy. As can be seen from the insets, the magnitude of the off-diagonal elements visibly increases as the BBO crystal is translated toward the detection image plane, accounting for the corresponding increase in system purity.

great interest from a fundamental standpoint, our results may suggest a possible means by which to avoid the information loss that can accompany spatial propagation of coherent optical signals. Our findings are relevant to any quantum optical communication or information storage scheme in which information loss from propagation-induced decoherence is a concern.

References

1. W. H. Zurek. *Progress of Theoretical Physics* **89,** 281 (1993).
2. W. H. Zurek. *Reviews of Modern Physics* **75,** 715 (2003).
3. M. Almeida, F. De Melo, M. Hor-Meyll, A. Salles, S. Walborn, P. S. Ribeiro & L. Davidovich. *Science* **316,** 579 (2007).
4. A. Nicolas, L. Veissier, L. Giner, E. Giacobino, D. Maxein & J. Laurat. *Nature Photonics* **8,** 234 (2014).
5. G. Vallone, V. D'Ambrosio, A. Sponselli, S. Slussarenko, L. Marrucci, F. Sciarrino & P. Villoresi. *Physical Review Letters* **113,** 060503 (2014).
6. M. Krenn, R. Fickler, M. Fink, J. Handsteiner, M. Malik, T. Scheidl, R. Ursin & A. Zeilinger. *New Journal of Physics* **16,** 113028 (2014).
7. J. Wang, J.-Y. Yang, I. M. Fazal, N. Ahmed, Y. Yan, H. Huang, Y. Ren, Y. Yue, S. Dolinar, M. Tur *et al. Nature Photonics* **6,** 488 (2012).
8. K. Chan, J. Torres & J. Eberly. *Physical Review A* **75,** 050101 (2007).
9. M. O. Scully & K. Drühl. *Physical Review A* **25,** 2208 (1982).
10. A. E. Siegman. *"Lasers. Mill Valley,"* (1986).
11. L. Allen, M. W. Beijersbergen, R. Spreeuw & J. Woerdman. *Physical Review A* **45,** 8185 (1992).
12. E. Karimi & E. Santamato. *Optics Letters* **37,** 2484 (2012).
13. A. Mair, A. Vaziri, G. Weihs & A. Zeilinger. *Nature* **412,** 313 (2001).
14. S. P. Walborn, C. Monken, S. Pádua & P. S. Ribeiro. *Physics Reports* **495,** 87 (2010).
15. E. Karimi, D. Giovannini, E. Bolduc, N. Bent, F. M. Miatto, M. J. Padgett & R. W. Boyd. *Physical Review A* **89,** 013829 (2014).
16. A. K. Ekert. *Physical Review Letters* **67,** 661 (1991).
17. D. F. James, P. G. Kwiat, W. J. Munro & A. G. White. *Physical Review A* **64,** 052312 (2001).
18. N. K. Langford, R. B. Dalton, M. D. Harvey, J. L. O'Brien, G. J. Pryde, A. Gilchrist, S. D. Bartlett & A. G. White. *Physical Review Letters* **93,** 053601 (2004).

Acknowledgements

F.B. acknowledges the support of the Natural Sciences and Engineering Research Council of Canada (NSERC). The authors acknowledge the support of the Canada Excellence Research Chairs (CERC) Program.

Author Contributions

F.B. and J.H. contributed equally to this work. E.K. and E.S. conceived the idea. F.B., J.H. and E.K. designed the experiment. F.B., J.H., H.M., N.B. performed the experiment. F.B. and J.H. analyzed the data. R.W.B. and E.K. supervised all aspects of the project. All authors discussed the results and contributed to the text of the manuscript.

Additional Information

Supplementary information accompanies this paper at http://www.nature.com/srep

Competing financial interests: The authors declare no competing financial interests.

How to cite this article: Bouchard, F. *et al.* Observation of quantum recoherence of photons by spatial propagation. *Sci. Rep.* **5**, 15330; doi: 10.1038/srep15330 (2015).

This work is licensed under a Creative Commons Attribution 4.0 International License. The images or other third party material in this article are included in the article's Creative Commons license, unless indicated otherwise in the credit line; if the material is not included under the Creative Commons license, users will need to obtain permission from the license holder to reproduce the material. To view a copy of this license, visit http://creativecommons.org/licenses/by/4.0/

Chapter 7

Conclusions

In conclusion, we have carried out five independent projects studying the classical and quantum dynamics of twisted light.

In the first place, we study the interaction of light and matter giving rise to the generation of twisted light. In the first chapter, we exploited the properties of total internal reflection in order to propose and demonstrate a novel device capable of generating light carrying two units of orbital angular momentum per photon independent of wavelength. This spin-to-orbit coupling is achieved by exploiting the geometrical phase arising from total internal reflection within two hollow axicons. The achromatic nature of the device may be used to generate white twisted light and white vector vortex beams. Such a device has applications in astronomy and imaging techniques. For example, an optical vortex coronagraph necessitates an achromatic generator of light carrying an orbital angular momentum value of $|\ell| = 2$.

In the work on laser-induced radial birefringence, we studied the effect of a laser beam on the elasticity of a material, leading to the alteration of its optical properties. Ultimately, radial birefringence produces spin-to-orbit coupling leading to the generation of twisted light and vector vortex beams. We have developed a theoretical model of the effect of laser illumination on the dielectric tensor of the material. In particular, we have studied this effect in two different illumination modes, i.e. a steady-state and a transient-state form. Those findings were experimentally tested with silver-doped glass in a pump-probe experiment, and good agreement with the theoretical model was found.

Using the same physical concept of geometrical phases as in the previous chapters, we explored spin-to-orbit coupling in a plasmonic metasurface. In this case, the

birefringence was due to polarisation-dependent plasmonic resonances in an array of L-shaped nano-antennas. The nano-antennas were then arranged transversally in a specific configuration resulting in the generation of light carrying an arbitrary orbital angular momentum value. In this study, we demonstrated the generation of twisted light with orbital angular momentum values as high as $|\ell| = 25$. Our metasurfaces could be important in applications requiring integrated and nano-scale devices. More importantly, the wide range of orbital angular momentum values generated allows for high-dimensional quantum cryptography, communication and computations with twisted photons.

In the second part of this thesis, we are interested in the propagation of twisted light. In chapter 5, we study the group velocity of classical pulses of light carrying several different orbital angular momentum values. Small differences in the free-space propagation of twisted pulses of light are predicted by our theoretical model. Our model is subsequently tested experimentally by implementing an intensity autocorrelation scheme. We experimentally showed that time delays on the order of several femtoseconds may arise from the propagation of twisted pulses due to their variation in group velocities.

Finally, we studied the propagation of twisted photons in the quantum regime. In particular, a specific pair of entangled twisted photons may experience decoherence of their quantum information under propagation. This loss of information is due to the coupling of the radial degree of freedom of the photon pair with their orbital angular momentum degree of freedom. In general, this decoherence effect will vary under propagation. We experimentally show this decoherence effect and moreover the retrieval of the quantum information carried by the entangled pair of twisted photons. We call this coherence retrieval process by the name of recoherence. Recoherence of twisted light was experimentally observed under a unitary transformation.

APPENDICES

Appendix A

Supplementary material: Observation of subluminal twisted light in vacuum

Supplementary Material

optica

Observation of subluminal twisted light in vacuum: supplementary material

FRÉDÉRIC BOUCHARD,[1,2] JÉRÉMIE HARRIS,[1,2] HARJASPREET MAND,[1,2] ROBERT W. BOYD,[1,2,3] AND EBRAHIM KARIMI[1,2,*]

[1] Department of Physics, University of Ottawa, 25 Templeton St., Ottawa, Ontario, K1N 6N5 Canada.
[2] The Max Planck Centre for Extreme and Quantum Photonics, University of Ottawa, Ottawa, Ontario, K1N 6N5, Canada.
[3] Institute of Optics, University of Rochester, Rochester, New York, 14627, USA.
*Corresponding author: ekarimi@uottawa.ca

Published 23 March 2016

This document provides supplementary information to "Observation of subluminal twisted light in vacuum: http://dx.doi.org/10.1364/optica.3.000351." © 2016 Optical Society of America

http://dx.doi.org/10.1364/optica.3.000351.s001

Experimental setup: The output of a 100 fs pulsed Ti:Sa laser operating with a repetition rate of 82 MHz and an average power of 300 mW at a central wavelength of 795 nm is split into two arms by means of a non-polarising beam splitter (BS). In the test arm, the incident beam is made to pass through a lens placed immediately prior to a kinoform displayed on a Pluto-HOLOEYE spatial light modulator (SLM), which reshapes the spatial distribution of the incoming pulsed beam into a desired HyGG_{ℓ} mode. In order to generate a pure $\mathrm{LG}_{p,\ell}$ mode, one would have to use an intensity masking technique. The downside to this method is the power reduction in the beam that accompanies the masking strategy, a crucial consideration in a nonlinear optical experiment, as the efficiency of the SHG signal depends on the intensity of the pump beam. No lenses are used after the hologram, in order to avoid the introduction of additional artificial time delays. Since the different LG modes considered have intensity maxima at different radii, a lens placed in the optical path of the beam would introduce an additional time delay, which would depend on the lens thickness at the radius of the beam's intensity maximum. We note that one may be tempted to overcome this difficulty by making use of flat (Fresnel) lenses. However, this would result in a distortion of the pulse shape and spectrum [1].
The first diffracted order obtained from the reflection of the test beam off the SLM is selected using an iris placed at the Fourier plane of the lens. The test and reference pulses are respectively focused by means of $f_1 = 400$ mm and $f_2 = 500$ mm lenses into a $L = 500$ μm thick type-I β-barium borate (BBO) crystal, where they are spatially overlapped. The Rayleigh range, $z_R = 2$ cm ≈ 40 L, associated with the test beam is much longer than the crystal length. The cross-SHG signal is isolated from the two other SHG outputs and fundamental beams by means of an iris followed by an interference filter. The power associated with this signal is measured over a period of one second using a Newport power meter with a silicon detector.

Cross-correlation: The second-order polarisation arising from the reference ($\mathrm{LG}_{0,0}$)-test ($\mathrm{LG}_{p,\ell}$) beam interaction is given by $P^{(2)}_{0,\ell}(t) = \epsilon_0\, \chi^{(2)} \mathrm{LG}_{0,0}(t)\, \mathrm{LG}_{0,\ell}(t-\tau)$, where $\mathrm{LG}_{0,\ell}(t)$ represents the time-dependent electric field associated with the $\mathrm{LG}_{0,\ell}$ mode, τ indicates the time delay between the two pulses, and $\chi^{(2)}$ is the second-order nonlinear susceptibility of the BBO crystal. The intensity associated with the cross-beam SHG signal is then proportional to the product $\left|\mathrm{LG}_{0,0}(t)\right|^2 \left|\mathrm{LG}_{0,\ell}(t-\tau)\right|^2$. Hence, maximal cross-beam SHG will be observed when the delay is set to be zero, $\tau = 0$. However, due to the Gaussian temporal profile of the pulses, some non-collinear SHG will result even in the case of small non-zero time delays. As the time delay between both pulses increases, the non-collinear SHG signal decreases gradually, disappearing when τ significantly exceeds the pulse temporal duration.

Phase and Group Velocities
A surface of constant phase, also known as a cophasal surface, associated with a monochromatic electric field $E(\mathbf{r},t) = A(\mathbf{r})e^{i(\omega\, t - \Phi(\mathbf{r}))}$, where $A(\mathbf{r})$ and $\Phi(\mathbf{r})$ respectively denote the amplitude and phase of the electric field, is given by [2]

$$\omega\, t\text{-}\Phi(\mathbf{r}) = \text{constant}, \qquad \textbf{(S1)}$$

whence

$$\delta\big(\omega\, t\text{-}\Phi(\mathbf{r})\big) = 0. \tag{S2}$$

The phase velocity describes the rate at which a point of constant phase travels through space, i.e. $v_{\mathrm{ph}} = \delta r_{\mathrm{ph}}/\delta t$, and can be calculated by

$$\omega\, \delta t\text{-}\nabla\Phi(\mathbf{r}) \cdot \delta\mathbf{r} = 0. \tag{S3}$$

Equation (S3) can be rearranged by introducing a unit vector $\hat{\mathbf{r}} = \delta\mathbf{r}/\delta r_{\mathrm{ph}}$, yielding

$$v_{\mathrm{ph}} = \frac{\delta r_{\mathrm{ph}}}{\delta t}$$

$$= \frac{\omega}{\mathbf{r}\cdot\nabla\Phi(\mathbf{r})} = \frac{\omega}{|\nabla\Phi(\mathbf{r})|}, \tag{S4}$$

where we have used the fact that $\hat{\mathbf{r}} = \nabla\Phi(\mathbf{r})/|\nabla\Phi(\mathbf{r})|$ for propagation of a wavefront.

For polychromatic fields, which in general may be expressed in the form $E(\mathbf{r},t) = \int_{-\infty}^{\infty} \tilde{A}(\mathbf{r},\omega)e^{i(\omega\, t-\Phi(\mathbf{r},\omega))}d\omega$, a group velocity may be assigned to the pulse envelope. Here, $\tilde{A}(\mathbf{r},\omega)$ is the angular frequency amplitude and represents the amplitude of the field in frequency space. The group velocity may be derived by expressing the electric field as a product of its carrier and envelope components, such that $E(\mathbf{r},t) = A(\mathbf{r},t)e^{i(\omega_0\, t-\Phi(\mathbf{r},\omega_0))}$, where ω_0 stands for the central angular frequency of the field. From these two expressions for the electric field, it can be seen that

$$A(\mathbf{r},t) = \int_{-\infty}^{\infty} \tilde{A}(\mathbf{r},\omega)e^{i\{(\omega-\omega_0)t-(\Phi(\mathbf{r},\omega)-\Phi(\mathbf{r},\omega_0))\}}d\omega. \tag{S5}$$

The phase Φ_{envelope} of the field envelope therefore evolves according to $\Phi_{\mathrm{envelope}} = (\omega-\omega_0)t - (\Phi(\mathbf{r},\omega)-\Phi(\mathbf{r},\omega_0))$. When $\Phi(\mathbf{r},\omega)$ is Taylor-expanded to first order in frequency around ω_0, i.e. $\Phi(\mathbf{r},\omega) \simeq \Phi(\mathbf{r},\omega_0) + (\omega-\omega_0)\partial_{\omega_0}\Phi(\mathbf{r},\omega)$, the condition for constant envelope phase is found to be

$$\delta\big(\Phi_{\mathrm{envelope}}\big) = 0; \tag{S6}$$

therefore, we have

$$(\omega\text{-}\omega_0)\delta\left(t\text{-}\partial_{\omega_0}\Phi(\mathbf{r},\omega)\right) = (\omega\text{-}\omega_0)\big(\delta t\text{-}\partial_{\omega_0}\nabla\Phi(\mathbf{r},\omega)\cdot \delta\mathbf{r}\big) = 0. \tag{S7}$$

Defining a unit vector for the position of the envelope, $\hat{\mathbf{r}} = \delta\mathbf{r}/\delta r_{\mathrm{g}}$, then gives

$$v_{\mathrm{g}} = \frac{\delta r_{\mathrm{g}}}{\delta t}$$

$$= \frac{1}{\hat{\mathbf{r}}\cdot\nabla\partial_{\omega_0}\Phi(\mathbf{r},\omega)} = \frac{1}{|\nabla\partial_{\omega_0}\Phi(\mathbf{r},\omega)|}. \tag{S8}$$

The amplitude of a Laguerre-Gauss beam is given by

$$\mathrm{LG}_{p,\ell}(r,\varphi,z) = \frac{C_{p,\ell}}{w(z)}\left(\frac{r\sqrt{2}}{w(z)}\right)^{|\ell|}\exp\left(-\frac{r^2}{w^2(z)}\right)L_p^{|\ell|}\left(\frac{2r^2}{w^2(z)}\right)e^{i\Phi^{\mathrm{LG}}}, \tag{S9}$$

where p is the radial index (positive integer), ℓ is the azimuthal index (integer), r and φ are the transverse cylindrical coordinates, $C_{p,\ell}$ are normalization constants, $w(z) = w_0(1 + (z/z_R(\omega))^2)^{1/2}$ is the beam radius, $L_p^{|\ell|}(x)$ are the generalized Laguerre polynomials, and Φ^{LG} contains all of the phase terms of the Laguerre-Gauss beam. The LG beam phase may be expressed explicitly as

$$\Phi_{p,\ell}^{\mathrm{LG}}(r,\varphi,z,\omega) = \frac{\omega}{c}z + \frac{\omega}{c}\frac{r^2}{2R(z,\omega)} + \ell\varphi\text{-}(2p+|\ell|+1)\zeta, \tag{S10}$$

where $\zeta := \arctan\left(\frac{z}{z_R(\omega)}\right)$ is the Gouy phase. The spatial dependence of the phase profile of the Laguerre-Gauss beam is the origin of the other-than-luminal propagation velocity. The Gouy phase is an obvious example of a non-trivial term in the phase of a beam that will give rise to sub- and super-luminal group velocities. By showing the surfaces of constant phase of the Gaussian beam along with a spherical wave, one can observe how the phase of a Gaussian beam is different from that of a spherical wave, hence suggesting a discrepancy in the group velocity. This concept is illustrated in Fig. S1, which shows the spatial dependence of the phase-fronts associated with Gaussian and spherical waves. This phase velocity leads to the conclusion that v_g is a function of r, z, ω, p and ℓ, i.e. $v_g(r, z; \omega; p, \ell)$.

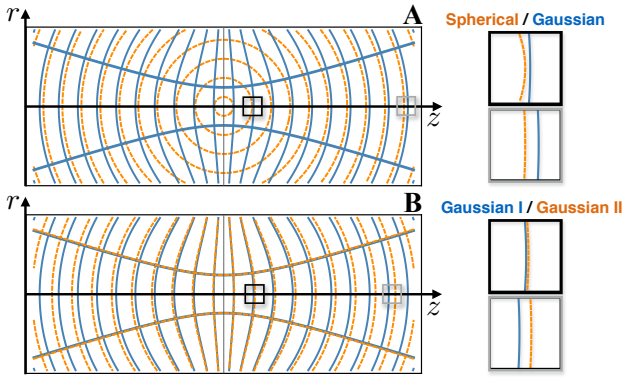

Fig. S1. Phase distribution of Gaussian and spherical waves upon propagation in vacuum. **A** Comparison between spherical (dashed orange) and Gaussian (solid blue) wave phase-fronts having identical wavelengths. As the two beams propagate away from the focus, the phase fronts of the spherical and Gaussian waves begin to separate. This accrued phase discrepancy is associated with the Gouy phase [12]. **B** Illustration of the differing wavefront distributions of two Gaussian beams (dashed orange and solid blue, respectively) differing in wavelength by 2%. Insets show enlarged views of the phase-fronts near the beam waist (black colour box) and approximately at 10 wavelengths from the waist (gray colour box). The radial dependence of the difference between the phase-fronts associated with the two beams is apparent in both figures. This can be understood to be a consequence of diffraction; the longer wavelength (orange) beam diverging more rapidly than the shorter wavelength (blue).

The radius of curvature $R(z,\omega)$ is obtained from the ABCD law for the case of a Gaussian beam incident on a thin lens at its waist, and subsequently focused to a new waist, and is given by [3]

$$R(z,\omega) = \frac{\left(\frac{z+d(\omega)}{z_{R,0}(\omega)}\right)^2 + \left(1\text{-}\frac{z+d(\omega)}{f}\right)^2}{\left(\frac{z+d(\omega)}{z_{R,0}^2(\omega)}\right)\text{-}\frac{1}{f}\left(1\text{-}\frac{z+d(\omega)}{f}\right)}, \tag{S11}$$

where $d(\omega) = f\left(1 + \left(f/z_{R,0}(\omega)\right)^2\right)^{-1}$ is the distance between the lens and the focus, f is the focal length of the lens, and $z_{R,0}(\omega)$

is the Rayleigh range of the beam prior to the lens. From the expression (S10) for the phase, one can obtain an explicit form for the group velocity of an LG beam by direct application of Eq. (S8),

$$v_g(\mathbf{r},\omega) = \frac{1}{\left|\nabla\partial_\omega \Phi^{LG}_{p,\ell}(\mathbf{r},\omega)\right|}. \quad \textbf{(S12)}$$

This was the approach taken to produce the theoretical curves shown in Fig. 2 for LG modes having different indices p and ℓ. The group velocity associated with a pulse exhibits a dependence on $\mathbf{r}$. The radii at which velocity measurements were made correspond to the coordinates through which the classical rays associated with each beam will pass, according to the ray tracing picture. Measurements plotted in Fig. 4 naturally reflect the group velocity of LG modes at $r_{max} = w(z)\sqrt{|\ell|/2}$ for $p = 0$ modes having different values of ℓ.

We note also that two LG beams characterized by equal central wavelengths and r_{max} values, but different indices ℓ and, correspondingly, different beam waists, will propagate at different group velocities. Even if the classical ray trajectories associated with two LG modes are made to coincide at the focus by changing the beam waist, their Rayleigh ranges will differ, and scale inversely with ℓ. Therefore, it is impossible to compensate for this effect by simply changing the beam waist; it is a beam property rather than a property of the optics. It should also be noted that the results shown in Fig. 2 are wavelength and beam waist dependent.

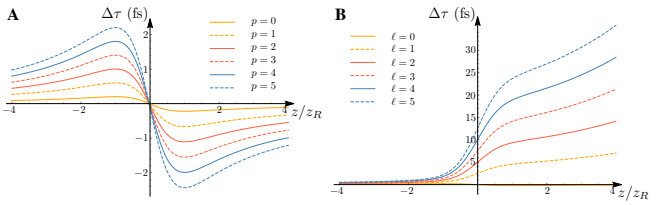

Fig. S2. Time delay between LG mode pulses and a plane wave pulse as a function of position along the beam axis. **A** Theoretical arrival times of $LG_{p,0}$ pulses relative to a plane wave pulse travelling at c, as a function of position along the beam axis. Since the maximal intensity of $LG_{p,0}$ modes is found on-axis (at $r = 0$), these relative arrival times do not include any contribution from the phase-front radius of curvature. As a result, any deviations from exactly luminal propagation may be attributed entirely to changes in the p index itself. **B** Theoretical plot showing arrival times of $LG_{0,\ell}$ pulses as a function of propagation distance, relative to a plane wave pulse travelling at . The time delays between LG pulses with nonzero ℓ indices and the plane wave pulse are monotonically-increasing functions of propagation distance for $\ell \neq 0$. This is due to the fact that LG beams with nonzero ℓ are characterized by subluminal group velocities throughout propagation. In each case, the plotted time delays are calculated at the radius of maximum intensity, $r_{max}(z)$, and therefore include the contribution of the phase-front radius of curvature to the group velocity of the LG pulse.

Hypergeometric-Gaussian modes

A given Hypergeometric-Gaussian mode with well-defined ℓ can be regarded as an infinite superposition of $LG_{p,\ell}$ modes with fixed ℓ and different p indices. In a general, a HyGG beam generated from a pitch-fork hologram finds most of its power peaked in the $LG_{0,\ell}$ mode [4]. Perhaps the most important correction that one needs to include while dealing with HyGG modes is the radius of maximum intensity r_{max}. In the following, we carry out a calculation to obtain an expression for the r_{max} of a HyGG beam at the focus.

The HyGG modes (in dimensionless coordinates) can be expressed as a superposition of modified Bessel function of the first kind.

$$u_{-|m|,m}(\rho) \propto e^{\frac{1}{2}\left(\frac{-2i}{1+\zeta}+\frac{1}{i\zeta+\zeta^2}\right)\rho^2}\rho\left[I_{\frac{|m|-1}{2}}\left(\frac{\rho^2}{2\zeta(1+i\zeta)}\right) - I_{\frac{|m|+1}{2}}\left(\frac{\rho^2}{2\zeta(1+i\zeta)}\right)\right],$$

where $\rho = r/w_0$ and $\zeta = z/z_R$ are the dimensionless radial and longitudinal coordinates, respectively. We consider here only the radial dependence of the mode (for reasons that will be obvious as we proceed). The squared modulus of the modal amplitude is then calculated,

$$\left|u_{-|m|,m}(\rho)\right|^2 \propto e^{\left(\frac{\rho^2}{1+\zeta^2}\right)}\rho^2\left|I_{\frac{|m|-1}{2}}\left(\frac{\rho^2}{2\zeta(1+i\zeta)}\right) - I_{\frac{|m|+1}{2}}\left(\frac{\rho^2}{2\zeta(1+i\zeta)}\right)\right|^2.$$

At this stage in the derivation, we assume that the term in the argument of the Bessel functions is very small. This condition is satisfied as the beam propagates away from the near field, at larger values of z. We can then approximate the modified Bessel function by,

$$I_\alpha(z) \approx \frac{1}{\Gamma(\alpha+1)}\left(\frac{z}{2}\right)^\alpha.$$

This approximation is valid in the limit where

$$0 < \left|\frac{\rho^2}{2\zeta(1+i\zeta)}\right| \ll \sqrt{\frac{|m|+1}{2}}.$$

The intensity of the beam can then be expressed in the following form,

$$\left|u_{-|m|,m}(\rho)\right|^2 \propto e^{\left(\frac{\rho^2}{1+\zeta^2}\right)}\rho^2\frac{1}{\Gamma\left(\frac{|m|+1}{2}\right)}\left(\frac{\rho^2}{4\zeta\sqrt{1+\zeta^2}}\right)^{|m|-1}\left[1 - \frac{1}{|m|+1}\left(\frac{\rho^2}{1+\zeta^2}\right) + \left(\frac{1}{|m|+1}\right)^2\frac{\rho^4}{4(\zeta^2+\zeta^4)}\right].$$

We proceed with an additional approximation, by neglecting the last term in the expression above. This is physically reasonable since z is assumed to be large in this case. Hence,

$$\left|u_{-|m|,m}(\rho)\right|^2 \propto e^{\left(\frac{\rho^2}{1+\zeta^2}\right)}\rho^2\frac{1}{\Gamma\left(\frac{|m|+1}{2}\right)}\left(\frac{\rho^2}{4\zeta\sqrt{1+\zeta^2}}\right)^{|m|-1}\left[1 - \frac{1}{|m|+1}\left(\frac{\rho^2}{1+\zeta^2}\right)\right].$$

If we concern ourselves only with the radial dependencies,

$$\left|u_{-|m|,m}(\rho)\right|^2 \propto e^{\left(\frac{\rho^2}{1+\zeta^2}\right)}\rho^{2|m|}\left[1 - \frac{1}{|m|+1}\left(\frac{\rho^2}{1+\zeta^2}\right)\right].$$

We can now differentiate the expression in order to obtain the maximal value for ρ,

$$\partial_\rho\left|u_{-|m|,m}(\rho_{max})\right|^2 = 0,$$

$$\rho_{max} = |m|^{1/4}(|m|+1)^{1/4}\sqrt{1+\zeta^2}.$$

Thus we obtain an expression slightly different from the case of LG beams, for which

$$r_{max}^{(HyGG)}(\ell,z) = w(z)\left(|\ell|(|\ell|+1)\right)^{1/4}.$$

References

1. E. Karimi *et al.*, Opt. Express **21**, 24991 (2013).

2. M. Born, E. Wolf, *Principles of optics: electromagnetic theory of propagation, interference and diffraction of light (Chapter 1)* (CUP Archive, 1999).
3. P. W. Milonni, J. H. Eberly, *Laser Physics (Chapter 7)* (John Wiley & Sons, 2010).
4. E. Karimi *et al.*, Opt. Lett. **32**, 3053–3055 (2007).

Appendix B

Supplementary Information: Observation of quantum recoherence of photons by spatial propagation

Supplementary Information for Observation of quantum recoherence of photons by spatial propagation

Frédéric Bouchard,[1] Jérémie Harris,[1] Harjaspreet Mand,[1] Nicolas Bent,[1] Enrico Santamato,[2] Robert W. Boyd,[1,3] and Ebrahim Karimi[1,*]

[1]*Department of Physics, University of Ottawa, 25 Templeton St., Ottawa, Ontario, K1N 6N5 Canada*

[2]*Dipartimento di Scienze Fisiche, Universitá di Napoli "Federico II", Complesso di Monte S. Angelo, 80126 Napoli, Italy*

[3]*Institute of Optics, University of Rochester, Rochester, New York, 14627, USA*

I. OAM CONSERVATION

A parametric process is one in which light interacts with a material in such a way as to leave the quantum state of this material unchanged after the interaction. The initial and final optical states then carry the same energy, linear momentum and angular momentum. The energy conservation condition is fulfilled by requiring the SPDC photon pairs to be frequency down-converted such that the sum of the frequencies of the SPDC photons is equal to the frequency of the pump photon. The down-converted photon pair is then in a frequency entangled state. Similarly, OAM conservation is enforced by the requirement that the SPDC photons be entangled in OAM, so that their state is given by the expression

$$\left|\psi_{\ell_p}\right\rangle = \sum_{m=-\infty}^{\infty} c_m \left|m+\ell_p\right\rangle_s \left|-m\right\rangle_i . \tag{1}$$

As can be seen from Fig. 1, the state $\left|\psi_{\ell_p}\right\rangle$ possess an *OAM spectrum*, $|c_m|^2$. The OAM spectrum can be tuned by carefully adjusting the SPDC phase matching condition of the nonlinear crystal. In the case of a BBO crystal, this can be easily achieved by tilting the crystal. For the case of $\ell_p = 0$, the OAM spectrum peaks at $\ell_{s,(i)} = \ell_{i,(s)} = 0$. As we break the symmetry by pumping the crystal with a photon $\ell_p \neq 0$, the OAM spectrum will peak at $\ell_{s,(i)} = \ell_p$ and $\ell_{i,(s)} = 0$. In this work, we limit our analysis to an OAM entangled state given by: $\left|\psi_{\ell_p}\right\rangle = \frac{1}{\sqrt{2}}\left(\left|\ell_p\right\rangle_s \left|0\right\rangle_i + e^{i\theta}\left|0\right\rangle_s \left|\ell_p\right\rangle_i\right)$.

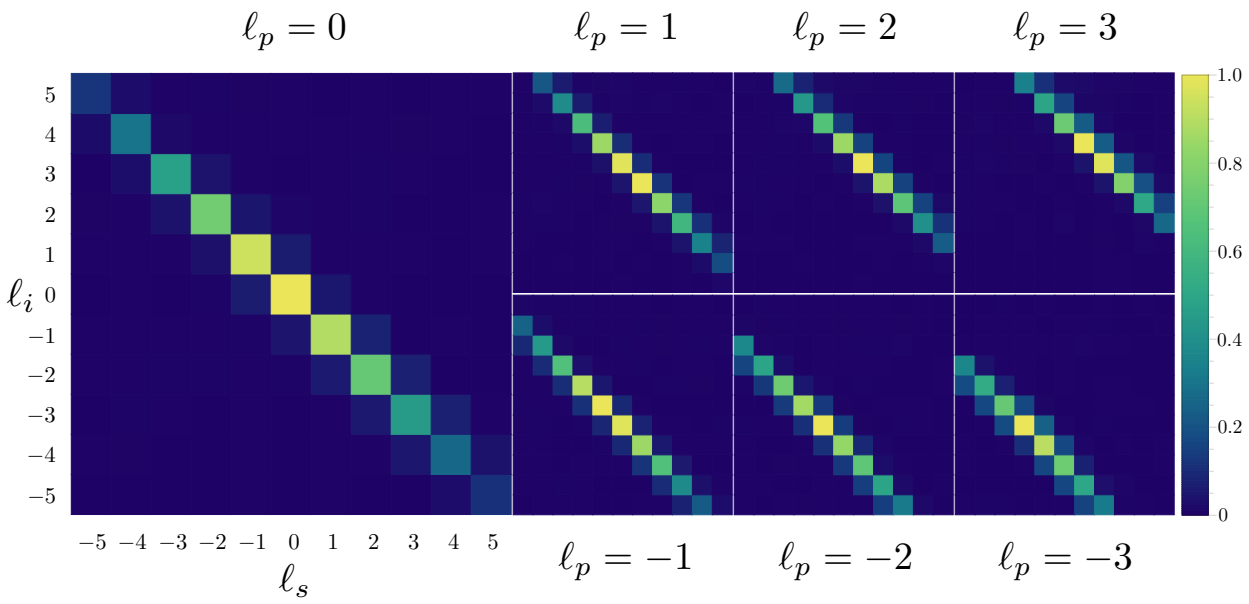

Figure 1: **OAM conservation matrices.** Results obtained from OAM conservation experiments are shown for incident pump beam OAM values of $\ell = -3, -2, -1, 0, 1, 2, 3$. These data show the expected linear relationship between signal and idler OAM values, the sum of the signal and idler OAM indices being exactly equivalent to the pump OAM, verifying angular momentum conservation.

II. SPDC PROPAGATION

If the down-converted (pump) photon incident on the nonlinear crystal is described by OAM and radial indices ℓ and $p = 0$ respectively, it must belong to a mode possessing the corresponding doughnut-shaped intensity pattern $F_\ell^{\text{pump}}(r, z)$. Hence, it will give rise to two SPDC photons for which the transverse modal amplitudes will initially (that is, at $z = 0$) be identical to $F_\ell^{\text{pump}}(r, 0)$. Conservation of OAM also requires that the total OAM of the signal-idler pair be equal to ℓ. One can show (See SI. I) that the most likely distribution of OAM between these photons would find the signal (idler) carrying ℓ units of OAM, while the idler (signal) carries none. As a result, at the SPDC plane, the transverse amplitudes of the generated photon pair will be given by $F_\ell^{s,i}(r, 0)$ and $F_0^{i,s}(r, 0)$, where we must have

$$F_\ell^{\text{pump}}(r, 0) = F_\ell^{s,i}(r, 0) = F_0^{i,s}(r, 0). \tag{2}$$

Upon propagation, however, the transverse amplitudes of the signal and idler modes will become dependent on the photons' respective OAM content. The particular transverse amplitude associated with each mode can be determined at a distance z from the SPDC plane by applying

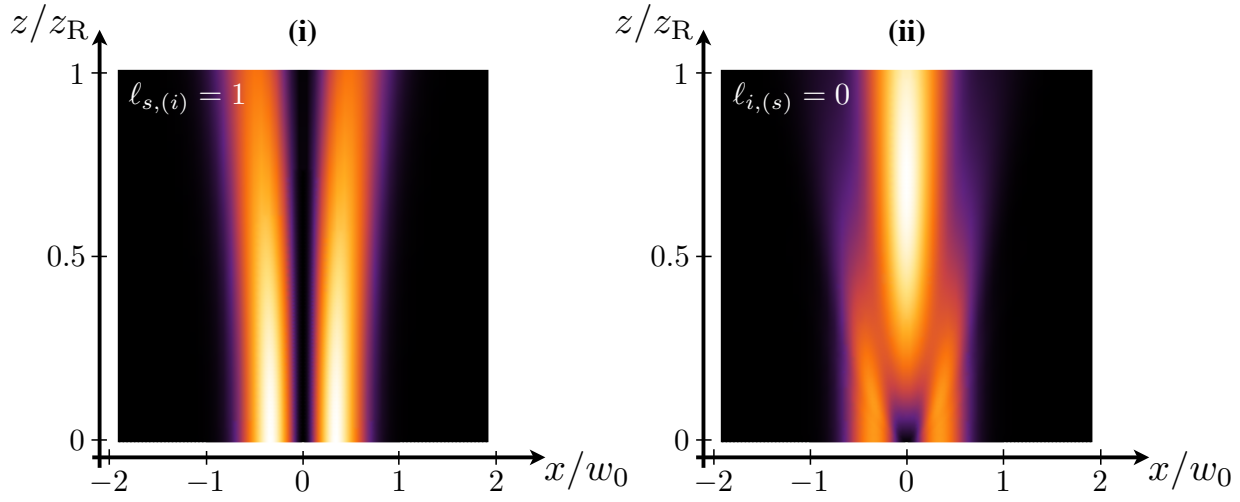

Figure 2: **Propagation simulation.** The intensities of the fields associated with the signal and idler photons generated from SPDC with a pump OAM of $\ell_p = 1$ are shown as a function of propagation distance z and transverse coordinate x, where $r = \sqrt{x^2 + y^2}$. The longitudinal and transverse figure axes are respectively normalised to the Rayleigh range z_R and beam waist w_0. The SPDC process produces a signal (idler) photon with an OAM of $\ell_{s,(i)} = 1$ and an idler (signal) photon with an OAM of $\ell_{s,(i)} = 0$. We show normalised beam intensities for a propagation range of $z/z_R = 0$ to $z/z_R = 1$. Of particular note, the radial intensities for both the signal and idler are found to agree perfectly in the $z = 0$ plane, differing appreciably within from one another within one Rayleigh lenght.

the Fresnel propagator to the signal and idler amplitude functions at $z = 0$, as follows:

$$F_\ell^{s,i}(r,z) = \frac{-i\pi}{\lambda z} e^{\frac{ikr^2}{2z}} \int_0^\infty r' dr' e^{\frac{ikr'^2}{2z}} J_\ell\left(\frac{krr'}{z}\right) F_\ell^{s,i}(r',0). \tag{3}$$

In the case of a pump photon belonging to a LG mode possessing an OAM index of $\ell = 1$, we have $F_1^{s,i}(r,0) = F_0^{i,s}(r,0) = -2i\sqrt{2}\left(\frac{r}{w_0}\right) e^{-\frac{r^2}{w_0^2}}$. In Fig 2, we show corresponding theoretical plots depicting the spatial evolution of the radial SPDC profiles for the case in which the signal photon carries $\ell = 1$ unit of OAM, while the idler carries none. The overlap between these fields decreases rapidly upon propagation, even prior to the Rayleigh range, as can be gathered from the figure. This diminished overlap results in a reduction in the values of the off-diagonal elements $c(z)$ of the reduced density matrix $\rho_{\mathrm{OAM}}^{\mathrm{red}}$, and a corresponding increase in the entanglement entropy of the OAM subsystem upon propagation.

III. THEORETICAL DETERMINATION OF THE OFF-DIAGONAL ELEMENTS OF THE REDUCED DENSITY MATRIX

The full density matrix describing the system (OAM) and ancilla (transverse profile) Hilbert spaces at any arbitrary propagation distance z is given by

$$\begin{aligned}\rho(z) = \frac{1}{2}\Big(& |1,0\rangle \otimes |F_{1,0}(z)\rangle \langle 1,0| \otimes \langle F_{1,0}(z)| \\ & + \quad |0,1\rangle \otimes |F_{0,1}(z)\rangle \langle 0,1| \otimes \langle F_{0,1}(z)| \\ & + \quad e^{-i\theta} |1,0\rangle \otimes |F_{1,0}(z)\rangle \langle 0,1| \otimes \langle F_{0,1}(z)| \\ & + \quad e^{i\theta} |0,1\rangle \otimes |F_{0,1}(z)\rangle \langle 1,0| \otimes \langle F_{1,0}(z)| \Big).\end{aligned} \tag{4}$$

The reduced density matrix over the OAM Hilbert space, $\rho_{\mathrm{OAM}}^{\mathrm{red}}$, is obtained by tracing $\rho(z)$ over the ancilla space. This can be achieved by taking

$$\begin{aligned}\rho_{\mathrm{OAM}}^{\mathrm{red}} \; = \; & \mathrm{Tr}_a \left[\rho(z)\right] = \\ & \int \; r_1 \, dr_1 \int r_2 \, dr_2 \; \left(\langle r_2|_i \langle r_1|_s \, \rho(z) \, |r_1\rangle_s |r_2\rangle_i \right),\end{aligned} \tag{5}$$

where, for example, $\langle r_2|_i \langle r_1|_s \cdot |F_{1,0}(z)\rangle = F_1(r_1,z)F_0(r_2,z)$. The reduced density matrix then becomes

$$\begin{aligned}\rho_{\mathrm{OAM}}^{\mathrm{red}} = \frac{1}{2}\Big(& a(z) \; |1,0\rangle \langle 1,0| + b(z) \, |0,1\rangle \langle 0,1| \\ & + \quad c(z) \, |1,0\rangle \langle 0,1| + d(z) \, |0,1\rangle \langle 1,0| \Big),\end{aligned} \tag{6}$$

where we have defined

$$a(z) := \int_0^\infty |F_1(r_1,z)|^2 \, r_1 dr_1 \int_0^\infty |F_0(r_2,z)|^2 \, r_2 dr_2, \tag{7}$$

$$b(z) := \int_0^\infty |F_0(r_1,z)|^2 \, r_1 dr_1 \int_0^\infty |F_1(r_2,z)|^2 \, r_2 dr_2, \tag{8}$$

$$c(z) := e^{-i\theta} \int_0^\infty F_1(r_1,z) F_0^*(r_1,z) r_1 dr_1 \int_0^\infty F_1^*(r_2,z) F_0(r_2,z) r_2 dr_2, \tag{9}$$

and

$$d(z) := e^{i\theta} \int_0^\infty F_0(r_1, z) F_1^*(r_1, z) r_1 dr_1 \int_0^\infty F_0^*(r_2, z) F_1(r_2, z) r_2 dr_2. \tag{10}$$

We note immediately that $a(z) = b(z) = 1$ in order to satisfy normalization of the transverse modes, and that $c(z) = d^*(z) = e^{-i\theta} \left| \int_0^\infty F_1^*(r, z) F_0(r, z) r dr \right|^2$. The matrix representation of $\rho_{\mathrm{OAM}}^{\mathrm{red}}$ is therefore given by

$$\rho_{\mathrm{OAM}}^{\mathrm{red}}(z) = \frac{1}{2} \begin{pmatrix} 1 & c(z) \\ c^*(z) & 1 \end{pmatrix}. \tag{11}$$

IV. TOMOGRAPHY

In this section we describe the tomography process used to reconstruct the state of the down-converted photons for different propagation distances. A measurement is made on the OAM state of the photons by means of two SLMs. As described in SI. I, the most probable output OAM state from SPDC pumped by a photon carrying ℓ_p units of OAM is given by: $|\psi\rangle = \frac{1}{\sqrt{2}} \left(|0, \ell_p\rangle + e^{i\theta} |\ell_p, 0\rangle \right)$. Thus, we limit our analysis to a four-dimensional OAM Hilbert space spanned by the following basis: $\{|0,0\rangle, |0,\ell_p\rangle, |\ell_p,0\rangle, |\ell_p,\ell_p\rangle\}$. This specific OAM subspace is isomorphous to the two-photon polarisation Hilbert space, which can be represented by the SU(4) group. Tensor products of Pauli matrices $\hat{\sigma}_x$, $\hat{\sigma}_y$, $\hat{\sigma}_z$ and the identity matrix $\hat{}$ are generators of the SU(4) group. Thus, one can reconstruct the OAM density matrix of the down-converted photon pairs by projecting the unknown bipartite OAM state over the eigenstates of the generators. This is analogous to measuring the polarisation Stokes parameters in the case of photon pairs. The correspondence with the case of polarisation is straightforwardly achieved by associating $|0\rangle$ and $|\ell_p\rangle$ with the left and right-handed circular polarised states of light, respectively. A full characterisation of the unknown OAM state can be effected by measuring sixteen independent Stokes-like parameters $r_{i,j}$ $(i, j = 0, 1, 2, 3)$. In order to perform these sets of measurements, we implement a well-known phase-flattening projective measurement. In this technique, both photons are imaged onto SLMs where different computer-generated holograms are displayed. These holograms flatten the phase-front of the beam at the first order of diffraction. The flattened component of the optical field can be coupled into a single mode optical fibre. The SLM and the single mode optical fibre act as the polariser in the case of polarisation state tomography. The reconstructed OAM density

matrix of the entangled photon pairs is then obtained from the following expression:

$$\hat{\rho} = \frac{1}{4} \sum_{i,j=0}^{3} r_{i,j} \, \hat{\sigma}_i \otimes \hat{\sigma}_j. \tag{12}$$

---

* Electronic address: ekarimi@uottawa.ca

Bibliography

[1] Les Allen, Marco W Beijersbergen, RJC Spreeuw, and JP Woerdman. Orbital angular momentum of light and the transformation of laguerre-gaussian laser modes. *Physical Review A*, 45(11):8185, 1992.

[2] Jun John Sakurai and Jim Napolitano. *Modern quantum mechanics*. Addison-Wesley, 2011.

[3] Milton Abramowitz, Irene A Stegun, et al. Handbook of mathematical functions. *Applied mathematics series*, 55:62, 1966.

[4] Anthony E Siegman. Lasers. university science books. *Mill Valley, CA*, 37:208, 1986.

[5] MW Beijersbergen, RPC Coerwinkel, M Kristensen, and JP Woerdman. Helical-wavefront laser beams produced with a spiral phaseplate. *Optics Communications*, 112(5):321–327, 1994.

[6] NR Heckenberg, R McDuff, CP Smith, and AG White. Generation of optical phase singularities by computer-generated holograms. *Optics letters*, 17(3):221–223, 1992.

[7] Lorenzo Marrucci, C Manzo, and D Paparo. Optical spin-to-orbital angular momentum conversion in inhomogeneous anisotropic media. *Physical Review Letters*, 96(16):163905, 2006.

[8] Alois Mair, Alipasha Vaziri, Gregor Weihs, and Anton Zeilinger. Entanglement of the orbital angular momentum states of photons. *Nature*, 412(6844):313–316, 2001.

[9] Hammam Qassim, Filippo M Miatto, Juan P Torres, Miles J Padgett, Ebrahim Karimi, and Robert W Boyd. Limitations to the determination of

a laguerre–gauss spectrum via projective, phase-flattening measurement. *JOSA B*, 31(6):A20–A23, 2014.

[10] Lev Davidovich Landau and Eugin M Lifshitz. Course of theoretical physics, theory of elasticity. 1986.

[11] Mohammad Mirhosseini, Omar S Magaña-Loaiza, Malcolm N O'Sullivan, Brandon Rodenburg, Mehul Malik, Martin PJ Lavery, Miles J Padgett, Daniel J Gauthier, and Robert W Boyd. High-dimensional quantum cryptography with twisted light. *New Journal of Physics*, 17(3):033033, 2015.

[12] Adetunmise C Dada, Jonathan Leach, Gerald S Buller, Miles J Padgett, and Erika Andersson. Experimental high-dimensional two-photon entanglement and violations of generalized bell inequalities. *Nature Physics*, 7(9):677–680, 2011.

[13] Nicolas J Cerf, Mohamed Bourennane, Anders Karlsson, and Nicolas Gisin. Security of quantum key distribution using d-level systems. *Physical Review Letters*, 88(12):127902, 2002.

[14] Robert W Boyd. *Nonlinear optics*. Academic press, 2003.

[15] Rick Trebino, Kenneth W DeLong, David N Fittinghoff, John N Sweetser, Marco A Krumbügel, Bruce A Richman, and Daniel J Kane. Measuring ultrashort laser pulses in the time-frequency domain using frequency-resolved optical gating. *Review of Scientific Instruments*, 68(9):3277–3295, 1997.

[16] CK Hong and Leonard Mandel. Experimental realization of a localized one-photon state. *Physical Review Letters*, 56(1):58, 1986.

[17] Thomas Durt, Berthold-Georg Englert, Ingemar Bengtsson, and Karol Życzkowski. On mutually unbiased bases. *International journal of quantum information*, 8(04):535–640, 2010.

[18] Daniel FV James, Paul G Kwiat, William J Munro, and Andrew G White. Measurement of qubits. *Physical Review A*, 64(5):052312, 2001.